DTU Library

Development of 3D Imaging Detectors for High Energy Astronomy Instrumentation

Owe, Selina Howalt

Publication date:
2023

Document Version
Publisher's PDF, also known as Version of record
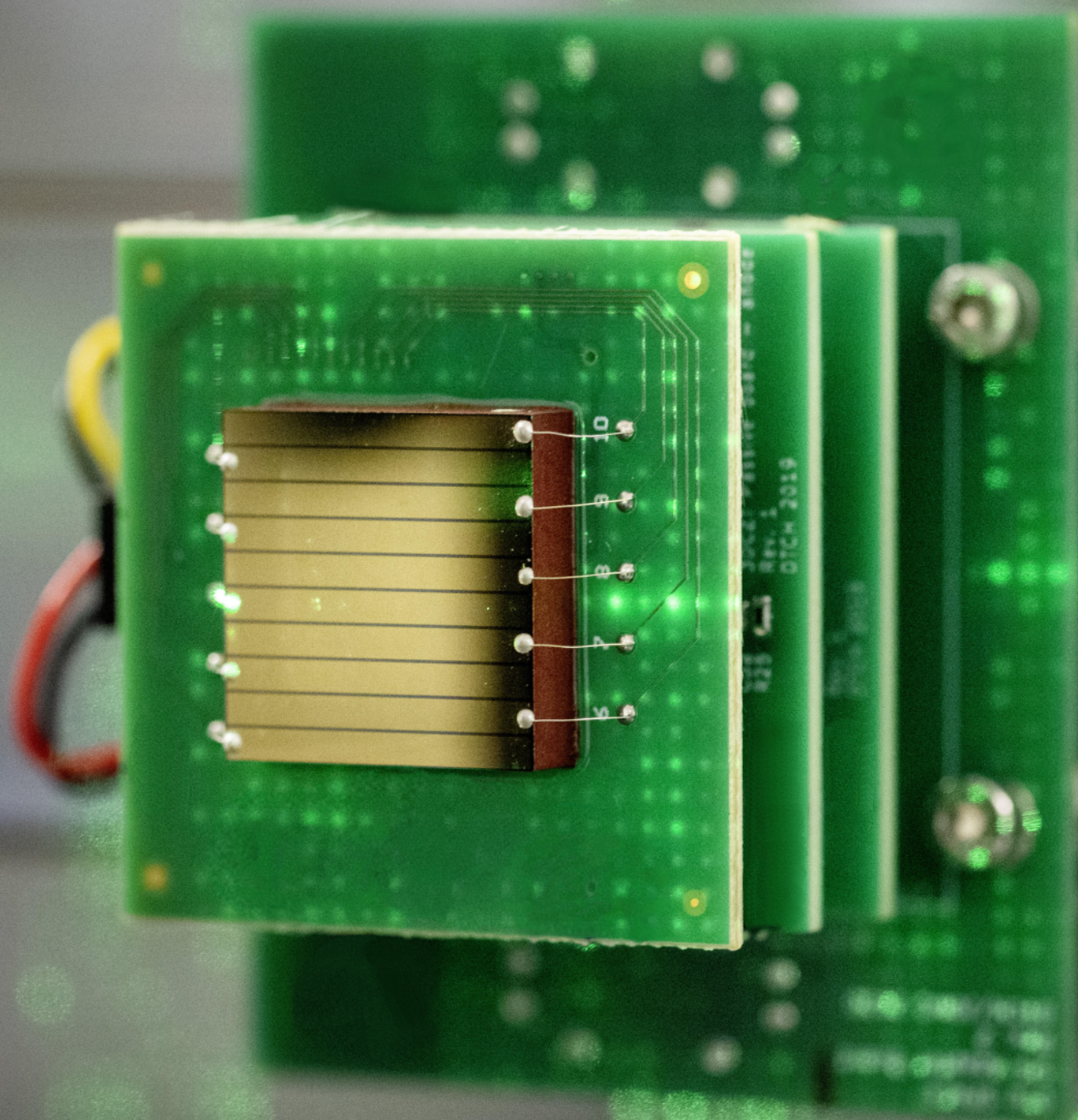
[Link back to DTU Orbit](#)

Citation (APA):
Owe, S. H. (2023). *Development of 3D Imaging Detectors for High Energy Astronomy Instrumentation*. Technical University of Denmark.

Development of 3D Imaging Detectors for High Energy Astronomy Instrumentation

PhD thesis by Selina R. H. Owe

Development of 3D Imaging Detectors for High Energy Astronomy Instrumentation

Author:
Selina Ringsborg Howalt Owe

Supervisor:
Irfan Kuvvetli

Co-supervisor:
Søren Brandt

A thesis submitted in fulfillment of the requirements for the degree of Doctor philosophiae

at

DTU Space

October 25, 2023

Abstract

Observations within medium-energy X- and gamma-ray astronomy are characterized by the technical challenges associated with instrument requirements. Current observatories suffer from poor sensitivity in this energy range compared to its neighboring bands, resulting in the medium-energy X- and gamma-ray domain remaining largely unexplored. Meaningful advances in this field depend on the next generation of space observatories, where state-of-the-art detector technology plays an important role.

This thesis focuses on the development of the 3D CZT drift strip detector, a promising candidate for future space missions within medium-energy X- and gamma-ray astronomy. This detector offers excellent intrinsic spatial and spectral resolution but requires further development to achieve a higher Technology Readiness Level. The thesis work is divided into three main components: an investigation into enhancing the 3D CZT drift strip detector model by mapping electron mobility and lifetime of the detector in three dimensions, a comprehensive characterization study of 10 3D CZT drift strip detector modules, and finally a simulation study of the detector operating in a small Compton camera configuration in orbit to assess its feasibility for use on small platforms like CubeSats.

In the first study, three-dimensional maps of electron mobility and lifetime in the 3D CZT drift strip detector were presented. Notably, these maps revealed material non-uniformity, which resulted in a substantial improvement in the 3D CZT drift strip detector model performance. The study underlined that knowledge of the detector material is essential for thorough understanding and characterization of the detector and for modeling its response. Areas of severe charge trapping or poor charge transport can be identified and included in the models as well. Furthermore, a reliable model depicting the pulse shape formation in the detector can be used to generate training data for future artificial neural network models, which can be a crucial for data size reduction.

The second study presented a full characterization work of 10 newly fabricated 3D CZT drift strip detector modules. A key finding of this study, was that the leakage current and overall performance of the modules were within the desired range, even though the modules were fabricated with a simpler electrode deposition process, compared to previous detector versions. This allows for a simpler manufacturing process of future modules. The study elevated the 3D CZT drift strip detector technology to a more modular design with a simpler electrode geometry, while maintaining sub-millimeter intrinsic spatial resolution, moderate spectral resolution at 122 keV, and good spectral resolution at 661.6 keV. Advances in the overall setup and dedicated readout electronics can reduce the dominant electronic noise and help further improve the spectral resolution of the detector. Additionally, it was highlighted that the 3D CZT drift strip detector technology might not only benefit the future of space exploration, but a technology transfer can make it valuable on Earth, for example, in future breast cancer diagnostic tools.

Lastly, the simulation study indicated that it may be possible to operate the detector on a small Compton camera payload, with some limited science goals. In terms of technology demonstration purposes, a small payload like this could be valuable.

This thesis brings the 3D CZT drift strip detector technology closer to a space ready module. It summarizes the findings and developments made throughout the project, and wraps up with an outlook on the future work for the 3D CZT drift strip detector, to hopefully, one day operate it in space.

Resumé

Observationer inden for medium-energi røntgen- og gammaastronomi karakteriseres ofte ved de tekniske udfordringer og høje krav forbundet med tilhørende instrumentering. Nuværende observatorier inden for dette energiområde lider under lav sensitivitet, særligt når det sammenlignes med nærliggende energiområder i det elektromagnetiske spektrum. Som følge af dette, er området inden for medium-energi røntgen- og gammastråling særligt uudforsket. Betydelige fremskridt afhænger af den næste generation af teleskoper, hvor ny detektorteknologi vil spille en central rolle.

Denne afhandling omhandler udviklingen af 3D CZT drift strip detektoren, en lovende kandidat til fremtidige rummissioner inden for medium-energi røntgen- og gammastråling. Detektoren har en fremragende positions- og energiopløsningsevne, men kræver yderligere udvikling for at højne dens Technology Readiness Level. Denne afhandling er opdelt i tre hovedkomponenter: Et studie der undersøger hvorledes en model af 3D CZT drift strip detektoren kan forbedres ved at kortlægge elektroners mobilitet og levetid i tre dimensioner, en omfattende karakteriseringsundersøgelse af 10 3D CZT drift strip detektormoduler og afslutningsvis et studie der simulerer detektoren inkluderet i en Compton kamera konfiguration for at vurdere dens anvendelighed til brug på små platforme så som CubeSats.

I det første studie blev elektroners mobilitet og levetid i 3D CZT drift strip detektoren kortlagt. Det resulterede i en markant forbedring af ydeevnen for 3D CZT-drift strip detektormodellen. Derudover blev en klar uensartethed i materialet afsløret, hvilket understreger vigtigheden af at forstå detektormaterialet for at modellerer dens respons. Desuden kan sådan en kortlægning bruges som en opslagstabel til korrektion for yderligere forbedring af detektoren. Undersøgelsen understregede, at kendskab til detektormaterialet er afgørende for en grundig forståelse og karakterisering af detektoren. Områder med alvorlig indfangning af ladninger eller dårlig ladningstransport kan kortlægges og inkluderes i modellerne. Derudover kan en pålidelig model, der skildrer signaldannelse i detektoren, bruges som træningsdata for fremtidige kunstige neurale netværksmodeller, hvilket kan være afgørende for reduktion af datastørrelsen. Det andet studie præsenterede et komplet karakteriseringsarbejde af 10 nyligt fremstillede 3D CZT drift strip detektormoduler. En af de primære resultater i denne undersøgelse var, at 'leakage current' og den samlede ydelse for modulerne var inden for det ønskede område, selvom modulerne blev fremstillet med en enklere proces i forhold til tidligere detektorversioner. Dette tillader en simplere fremstilling af fremtidige moduler. Undersøgelsen hævede teknologien for 3D CZT drift strip detektoren til et mere modulært design med en enklere elektrodegeometri, samtidig med at den stadig viste en sub-millimeter positionsopløsningsevne, moderat energiopløsningsevne ved 122 keV og god energiopløsningsevne ved 661,6 keV. Forbedringer i den samlede konfiguration og en dedikeret udlæsningselektronik kan reducere den dominerende elektroniske støj og hjælpe med yderligere at forbedre detektorens energiopløsningsevne. Derudover blev det fremhævet, at 3D CZT drift strip detektorteknologien ikke kun kan gavne fremtidens rumforskning, men en teknologioverførsel kan gøre den værdifuld på Jorden, f.eks. i fremtidige diagnostiske værktøjer til brystkræft.

Endeligt indikerede simuleringer, at det bør være muligt at betjene detektoren i en lille Compton kamera konfiguration med begrænsede videnskabelige mål. Med hensyn til en teknologi demonstration kunne sådan et instrument være værdifuld. Denne afhandling bringer 3D CZT drift strip detektoren tættere på et færdigt modul. Den sammenfatter projektets fund og udviklinger, og afsluttes med en perspektivering til 3D CZT drift strip detektorens fremtidige udviklinger, med håb om en dag at betjene den i rummet.

Popular Science Summary

The detection of light is essential to understanding our Universe. Observatories on Earth and in space make use of sophisticated instrumentation designed specifically for the light they examine. Light emitted in the Universe spans the entire electromagnetic spectrum, from low-energy radio waves to high-energy gamma-rays. X- and gamma-rays are generated in the most energetic phenomena occurring in the Universe, including, but not limited to, supernova explosions, relativistic jets from active galactic nuclei, and gamma-ray bursts. However, medium-energy X- and gamma-ray astronomy is one of the least explored fields in the Universe. Instruments observing in this energy range suffer from poor sensitivity. Only the next generation of space observatories will be able to make meaningful advances in this field, where new state-of-the-art detector technology will be a key contributor.

This PhD focuses on the development of 3D imaging detectors to operate in the medium X- and gamma-ray domain, centered around the 3D CdZnTe drift strip detector technology developed at DTU Space. Three main studies were conducted during the project. First, it was presented how the 3D spatial sensitivity of the detector could be used to conduct a finer detector material study and utilize this to improve the performance of the detector model. Secondly, a comprehensive characterization study of 10 detector modules was conducted. In this, it was shown that despite a simplification in the detector manufacturing process, the fine intrinsic spatial resolution and good energy resolution persisted. Furthermore, it was underlined that a technology transfer of the detector from space technology to medical applications can benefit future tools for breast cancer diagnostics. Lastly, a feasibility study of using the detector in a small satellite configuration for observations in the medium-energy X- and gamma-ray domain was conducted, stressing the suitability of the detector for future observatories within this energy domain.

Acknowledgments

First and foremost I want to thank my supervisor Irfan Kuvvetli for giving me the opportunity of pursuing this PhD. Thank you for supporting me throughout the entire PhD project, also both times I went on maternity leave. Thank you for all the hours you have dedicated to our discussions, teaching, and mentoring. I have learned so much.

I also want to thank Carl Budtz-Jørgensen for always providing review and constructive feedback on all my work. Your expertise have been a huge help throughout the project. Also thank you to Niels Lund for always checking in on how I am doing, and for all the interesting discussions on Compton cameras and Laue lenses. Thank you Denis Tcherniak for all your valuable work on the detectors and laboratory, and Michael Avngaard for always helping me out whenever I needed it.

Thank you to all our collaborators from Kromek on the MBI project, with a special thank you to Alexander Cherlin on your valuable feedback on my work, and insights on medical imaging.

Thank you to all my colleagues at DTU Space, especially my fellow early-career scientists, those of you who are still at DTU Space and the ones who continued on during my time here. Thank you for providing a comfortable work environment.

A special thanks to Andreas Zoglauer from UC Berkeley. I appreciate all the help and guidance you have provided me, both on video-calls and e-mail. I admire your work, and I am grateful for all your guidance, even though my external stay was implicated by the pandemic.

Thank you to all my friends and family for cheering me on. A special thanks to my almost-sister, my cousin Ida, for always making me laugh, for always correcting my grammar, and telling my how my punctuation should be done. I know it will not be perfect, but hopefully it is OK. And thank you to my big-brother Isak, for all the moral support and for fixing the front page image of this thesis in the last minute.

Thank you, to my good friend Lan, for being a great companion throughout high school and University. Thank you for reading through and correcting this thesis. I hope we will find ourselves working together once again, one day.

My two girls, Agathe and Celeste, who entered the world during this PhD. You have put everything into perspective - thank you. And thank you, Rasmus, for being my forever best friend, for being such a devoted dad to our girls, for always being helpful and supportive of my work, and for always patiently listening to my passionate talk about detectors.

Thank you to my parents, Anja and Thomas, for nurturing my passion for science since I was a young kid, even though you are from a completely different world. Thank you for keeping it creative, all the praise and encouragement, and for always looking after the girls whenever Rasmus and I needed to work.

Contents

List of Abbreviations

ADC	Analog to Digital Converter
ARM	Angular Resolution Measure
ASIC	Application-Specific Integrated Circuit
CCD	Charged Coupled Device
CCE	Charge Collection Efficiency
CSP	Charge Sensitive Preamplifier
CZT	Cadmium Zinc Telluride (CdZnTe)
DOI	Depth Of Interaction
DSM	Drift Strip Method
DSRI	Danish Space Research Institute
ESA	European Space Agency
FWHM	Full Width at Half Maximum
FoV	Field of View
GeV	Gigaelectron Volts
GRB	Gamma Ray Burst
HV	High Voltage
keV	kiloelectron Volts
LEO	Low Earth Orbit
LD-MBI	Low Dose Molecular Breast Imaging
MBI	Molecular Breast Imaging
MeV	Megaelectron Volts
MEGAlib	The Medium-Energy Gamma-ray Astronomy library
NIM	Nuclear Instruments and Methods
PCB	Printed Circuit Board
PI	Principal Investigator
SAA	South Atlantic Anomaly
S/N	Signal to Noise
TOF	Time Of Flight
TRL	Technology Readiness Level

Preface

This thesis was prepared at the Technical University of Denmark, in the Astrophysics and Atmospheric Physics department at DTU Space. The project spanned from May 2019 to October 2023, with maternity leave periods from November 2020 to July 2021 and from August 2022 to May 2023. As required by the Danish PhD program, 27.5 ECTS points were earned during the project.

The studies included in this thesis, were presented at the virtual conferences IEEE NSS MIC RTSD in 2020 and 2021, the Annual Danish Astronomy Meeting in Fredericia, Denmark in 2022, and the 24th International Workshop on Radiation Imaging Detectors in Oslo, Norway in 2023.

....   October 25, 2023
....

Selina Ringsborg Howalt Owe   Date

Don't search for all the answers at once.
A path is formed by laying one stone at a time.
- The Giant, Twin Peaks

1 Introduction

The detection of light is a fundamental aspect of understanding the Universe, uncovering its secrets, and answering yet unanswered questions. Observatories on the Earth's surface, or in space, require sophisticated, state-of-the-art instrumentation, designed specifically for the energy of the light they examine. Light emitted in the Universe spans the entire electromagnetic spectrum, from low-energy radio to high-energy gamma-rays. Several astronomical targets of interest are found within high-energy astronomy, particularly considering recent advances in multi-messenger astrophysics [1, 2]. Hard X- and gamma-rays with energies in the order of kilo-electron volts (keV) to gigaelectron volts (GeV) are generated in the most energetic phenomena occurring in the Universe, including, but not limited to, supernovae explosions, relativistic jets from active galactic nuclei, and gamma ray bursts (GRBs). Measuring the photons emitted by such compact objects is important to understand star formation and the evolution of the Universe. While high-energy astronomy generates significant interest and is recognized for its importance, instruments observing a subset of the range (the medium energy X- and gamma-ray range) suffer from poor sensitivity compared to neighboring energy ranges. The medium-energy X- and gamma-ray range refers to light with energies in the order of megaelectron volts (MeV). This is also referred to as "the MeV domain", and is one of the least explored energy ranges in the electromagnetic spectrum. Figure 1.1 shows sensitivities of instrumentation (current and past) observing the X- and gamma-ray domain. A gap in sensitivity is evident from 100 keV to 100 MeV when compared to the neighboring energy ranges. This gap in sensitivity is often referred to as "the MeV gap". It arises from the inherent difficulty of observing this energy domain. Firstly, the probability of high-energy photons interacting with the detector material is low. Furthermore, three energy-loss processes (photoelectric absorption, Compton scattering, and pair production) or a combination of them may occur. This results in a combination of a low interaction probability together with long-range secondaries. Additionally, a high background radiation rate exists which impacts the instrument's sensitivity, along with activation in the instrument and its surroundings itself [3].
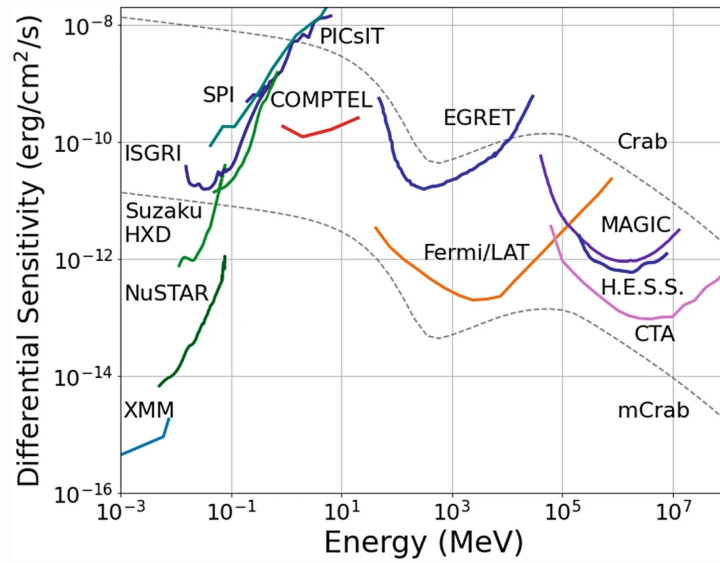

Figure 1.1: Differential sensitivity for X- and gamma-ray observatories (current and past). The limited performance achieved in the MeV domain is evident between 100 keV to 100 MeV, often referred to as "the MeV gap". Figure obtained from [3]. *Reproduced with permission from Springer Nature.*

Due to the difficulties of observing photons in the medium X- and gamma-ray region, the requirements for future observatories for the MeV-domain are demanding. Onboard detector technology must posses (among others) high stopping power, photon-by-photon detection, and high spatial, spectral, and timing resolution. For a detector to be included in any future large gamma-ray observatory, it must be thoroughly tested and have a high Technology Readiness Level (TRL).

The main focus of this PhD study is on the challenges of radiation detection and measurement in the medium X- and gamma-ray domain, on the basis of the 3D CdZnTe (CZT) drift strip detector technology developed at DTU Space. The project examines a subset of challenges associated with developing detectors for high-energy astronomy, based on the 3D CZT drift strip detector technology. With the given time frame of the project, the thesis considers three aspects related to the detector development:

1. **Detector model development and optimization:** The first part of the project investigates how the spatial sensitivity of the 3D CZT drift strip detector can be utilized to map the material electron mobility and lifetime in the detector bulk. This is important for compound semiconductor detectors, where charge transport properties are imperfect. A 3D map can be used to do 3D corrections of the detector response. Furthermore, it is particularly important for detector model development, since the inhomogeneity of the material impacts the signal response from the detector.

2. **Characterization and evaluation of new detector modules:** The second part of the project consists of a comprehensive characterization study of 10 3D CZT drift strip detector modules fabricated during the PhD study in collaboration with the company Kromek. The aim is to enhance the technology, while also investigating its suitability for a medical application within breast cancer diagnostics.

3. **Design and simulation study:** The final part of the project investigates the feasibility of using the 3D CZT drift strip detector in a Compton camera configuration onboard a small space instrument, for example on board a CubeSat. This is achieved through an in-orbit simulation study.

The project resulted in three papers, which represent the main work of this thesis, one paper for each of the above mentioned focus points. At the time of writing this thesis, two of the papers are peer-reviewed and published [4, 5] (Appendix A and B), and the final paper was submitted for review in September 2023 (Appendix C). The work conducted in this thesis underlines the suitability of the 3D CZT drift strip detector for use in high-energy astronomy instrumentation, and additionally, the transfer of the technology into other areas, such as medical applications.

1.1   Thesis outline

This thesis consists of the following chapters:

- **Radiation Detector Theory:** An overview of X- and gamma-ray radiation detector theory. This includes radiation interactions with matter, the basic principles of radiation detectors, general detector types, and an overview of semiconductor detector theory in relation to CZT detectors.

- **Scientific Space Instruments for X- and Gamma-ray Astronomy:** An overview of the common measurement techniques for X- and gamma-ray astronomy is given including telescope types and detectors used for these. Furthermore, considerations for future X- and gamma-ray astronomy instrumentation is given.

- **The 3D CZT Drift Strip Detector:** In this chapter, the overall theory of the 3D CZT

drift strip detector developed at DTU Space is given. This includes the general concept and operation, together with an overview of the detector laboratory and measurement setup. The latest versions of the detector is introduced, and finally the detector response and data analysis procedure is described.

- **Summary of Papers:** In this chapter, the main work of this thesis is summarized. Three papers cover the results of this thesis. The first paper investigates how the 3D spatial sensitivity of the detector can be used to map the detector material properties, together with improving detector model performance. The second paper is a comprehensive characterization of 10 detector modules, in relation to use in medical, but also space applications. The final paper is a feasibility study of using the detector in a small Compton camera Space mission for technology demonstration purposes.

- **Conclusion:** Finally, the findings of this thesis are outlined. Final conclusions are drawn, together with a discussion of what the future holds for the 3D CZT drift strip detector technology.

2 Radiation Detector Theory

Detection and measurement of X- and gamma-ray radiation is crucial in various fields and applications. High-energy radiation detectors reside in complex scientific instruments such as particle accelerators to study the structure of matter, or on board spaceborne telescopes observing high-energy radiation emitted in the hot and violent Universe. In everyday use on Earth, the detectors can, for example, be found at hospitals embedded in medical diagnostic systems, such as CT- and PET-scanners, or operating in airport luggage security systems.

Detectors for X- and gamma-ray radiation are diverse in material, operation, and capabilities. The appropriate detector for a given application depends on the requirements. This chapter will provide an overview of high-energy radiation detection and measurement.

2.1 Interaction of X- and gamma-rays with matter

Detection of high-energy radiation depend on the interaction between the radiation, and the detector material. Radiation such as alpha- and beta-particles, protons, neutrons, and X- and gamma-rays, can ionize material as it passes through. Understanding how ionizing radiation interacts with matter is therefore crucial. In this thesis, only X- and gamma-ray radiation is considered.

X- and gamma-ray photons mainly interact with matter by the four processes: Elastic scattering, photoelectric absorption, Compton scattering, and pair production. In the process of elastic scattering, no energy is transferred to the detector material, only the direction of the radiation is affected. The three remaining processes are fundamental for measurement and detection, since they deposit energy to be measured. The three processes are distinct, and the probability of the interaction type depends on the atomic number of the absorber material and the energy of the incident radiation. Figure 2.1 illustrates the relative importance of the three interaction types. The lines indicate where the probability of the neighboring processes is equal. Here it is seen that photoelectric effect dominates in the lower energy range. As the atomic number of the
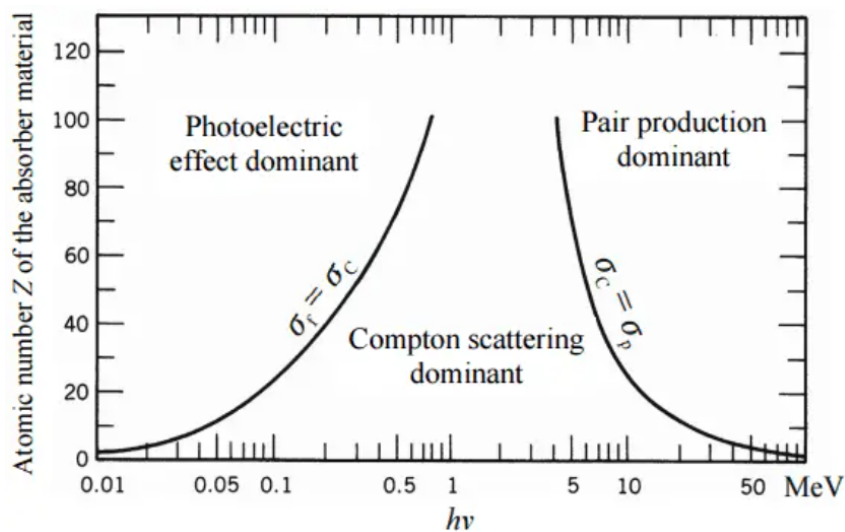

Figure 2.1: Relative importance of the photoelectric absorption, Compton scattering, and pair production interaction types with matter. The lines show the values for atomic number and energy, where the two neighboring processes are equal. Figure obtained from [6].

absorber material increases, so will the probability of photoelectric absorption towards medium energies. For the medium energies (the MeV domain) Compton scattering is dominant. At high energies, pair production is dominant, and as the atomic number of the absorber material increases, so will the probability of pair production towards medium energies. In the following sections, these three interaction processes are described.

2.1.1 Photoelectric absorption

The dominating interaction type in the lower energy range is photoelectric absorption. Figure 2.2 illustrates the photoelectric absorption process, where an interaction between an incident photon and an absorber atom occurs. In the process, the photon is replaced by an energetic photoelectron ejected by the absorber atom from one of its bound shells. This leaves an ionized absorber atom with a vacancy in one of its bound shells. The vacancy is filled by a free electron or by rearrangement of electrons from other shells of the atom, generating a characteristic X-ray or Auger electron. Photoelectric absorption is predominant for photons of low energy and the probability is enhanced when the atomic number of the absorber material increases. The energy of the ejected photoelectron, E_{e^-}, is equal to the difference in energy between the incident photon energy, hv, and the binding energy of the atom, E_b,

$$E_{e^-} = hv - E_b \tag{2.1}$$

where h is Planck's constant and v is the photon frequency [7].
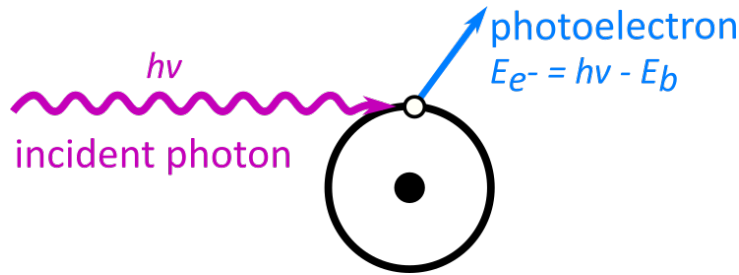
Figure 2.2: Illustration of photoelectric absorption. The incident photon interacts with the absorber atom, and is replaced by an energetic photoelectron.

2.1.2 Compton scattering

In the medium-energy domain, Compton scattering is dominant. The probability depends on the atomic number of the absorber, as illustrated in Figure 2.1, where Compton scattering becomes more probable at a larger energy range as the atomic number of the absorber material decreases. Compton scattering is an interaction between the incident photon and an electron in the material of interaction. As the photon interacts with the electron, it transfers some of its energy to the electron, which is then recoiled, and the photon is scattered by an angle, θ. An illustration of the Compton scattering interaction is given in Figure 2.3(left). Assuming the electron to be at rest, the scattered photon energy, hv', can be described by [8]

$$hv' = \frac{hv}{1 + \left(\dfrac{hv}{m_0 c^2}\right)(1 - \cos\theta)} \tag{2.2}$$

where $m_0 c^2 = 0.511$ MeV is the rest mass energy of the electron [7]. The electron mass is denoted m_0, and the speed of light c. The kinetic energy of the recoil electron, E_{e^-}, is given by the difference between the incident photon energy and the scattered photon energy

$$E_{e^-} = hv - hv' = hv \left(\frac{\frac{hv}{m_0 c^2}(1 - \cos\theta)}{1 + \frac{hv}{m_0 c^2}(1 - \cos\theta)} \right). \tag{2.3}$$

The scattering angle of the photon depends on the amount of energy that is transferred to the electron. The photon can be scattered with an angle $0° < \theta \le 180°$. The following two boundary cases exist [7]:

1. $\theta \simeq 0°$: In this case, the photon is scattered with an angle close to zero, resulting in the recoil electron to have a minimum amount of energy transferred. The scattered photon has close to the same energy as the incident photon.

2. $\theta = 180°$: The incident photon is back-scattered towards its origin, and the maximum amount of energy possible is transferred to the recoil electron.

The differential scattering cross section $d\sigma/d\Omega$ for Compton scattering was derived by O. Klein and Y. Nishina [9] for the case of unbound electrons at rest, and is given by

$$\left(\frac{d\sigma}{d\Omega} \right)_{unbound} = Z r_0^2 \left(\frac{1}{1 + \alpha(1 - \cos\theta)} \right)^2 \left(\frac{1 + \cos^2\theta}{2} \right) \left(1 + \frac{\alpha^2(1 - \cos\theta)^2}{(1 + \cos^2\theta)(1 + \alpha(1 - \cos\theta))} \right) \tag{2.4}$$

where r_0 is the classical electron radius, Z is the atomic number of the scattering material, and $\alpha = hv/m_0 c^2$ [7]. The angular distribution of the differential scattering cross section is shown in Figure 2.3(right) for a selection of incident photon energies. It shows that for lower energies, forwards and backwards scattering are almost equally probable. As the energy of the incident photon increases, the larger the tendency is to forward scatter.
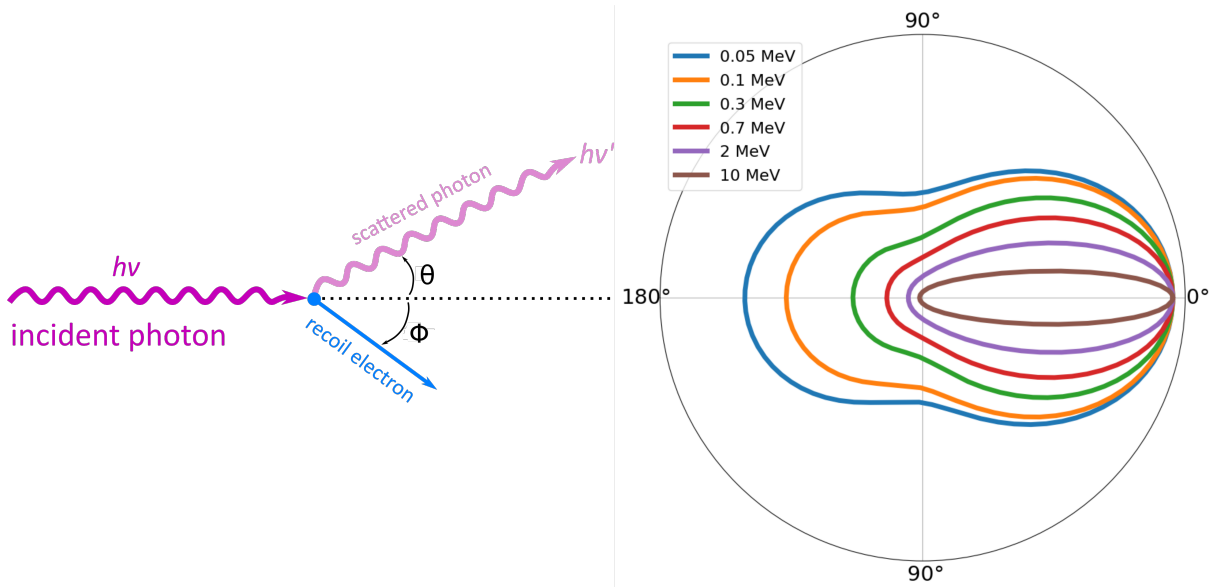
Figure 2.3: (Left) Schematic of the Compton scattering interaction. The incident photon interacts with an electron, resulting in part of the photon energy to be transferred to the recoil electron, and the photon to scatter at an angle, θ, that depends on the deposited energy. (Right) Differential scattering cross section as function of Compton scatter angle, with photon incidence direction from the left.

The Compton scattering interaction can be utilized as an imaging technique in the Compton camera instrument. This will be introduced in Chapter 3 of this thesis. In the following sections,

two key phenomena related to Compton scattering are described, since they have an important impact on the Compton camera instrument design.

2.1.2.1 Doppler broadening

In reality the electrons are neither free nor at rest. As a consequence, the distribution of energy between the scattered photon and the recoil electron changes from that predicted by Eq. (2.2). Therefore, a broadening in the lines in the energy spectra measured at fixed scatter angles will occur [10, 11]. This is referred to as Doppler broadening [12]. In 1975, R. Ribberfors derived an expression for the differential scattering cross section that considers the momentum distribution of the bound electrons [13, 11]. This is given by

$$\left(\frac{d\sigma}{d\Omega}\right)_{bound} = \left(\frac{d\sigma}{d\Omega}\right)_{unbound} S_i^I(hv, \theta, Z) \tag{2.5}$$

where the incoherent scattering function of the i-th shell electrons in the impulse approximation is denoted S_i^I [11].

The fact that the electrons are bound and not at rest has the following consequences compared to the case where the electrons are free and at rest [11]:

1. A change in the scatter probabilities, especially at lower energies, where the photons will have a somewhat higher chance of scattering.

2. A change in the scatter angle distribution, where small and large scatter angles will be suppressed a bit. This effect will reduce as the energy increases.

3. A change in energy distribution between recoil electron and scattered photon. This results in the measured scattering angle to differ from the one predicted by Eq. (2.2).

Doppler broadening will impose a lower limit to the angular resolution for a Compton camera, and is directly related to the atomic number of the detector material [12].

2.1.2.2 Polarization

If radiation from a linearly polarized source interacts by Compton scattering, the polarization information is somewhat preserved. Compton cameras will therefore inherently be sensitive to polarization [3, 12].

The following differential cross section applies, for a linearly polarized source

$$\left(\frac{d\sigma}{d\Omega}\right)_{unbound,pol} = \frac{r_0^2}{2}\left(\frac{hv'}{hv}\right)^2\left(\frac{hv'}{hv} + \frac{hv}{hv'} - 2\sin^2\theta\cos^2\chi\right) \tag{2.6}$$

where χ is the azimuthal scatter angle. The polarization signature of the linearly polarized incident photons is given by

$$P(\chi) = P_0 + A\cos\left(2\left(\chi - \chi_0 + \frac{\pi}{2}\right)\right) \tag{2.7}$$

where χ_0 is the direction of the original polarization vector, A is the amplitude, and P_0 is the offset of the azimuthal scatter angle distribution [12]. The polarization signature for a 100% linearly polarized beam is illustrated in Figure 2.4.

The modulation describes the polarization response of the detector, and is the relation between the amplitude and the offset. For a 100% linearly polarized source this is described by[12]

$$\text{modulation} = \frac{P_{\max} - P_{\min}}{P_{\max} + P_{\min}} = \frac{A}{P_0}. \tag{2.8}$$
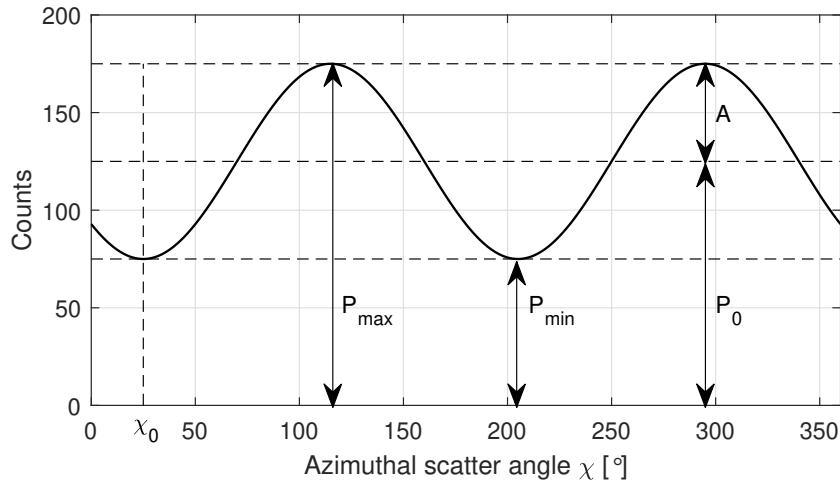
Figure 2.4: Schematic illustrating the polarization signature for a 100% linearly polarized source. Figure obtained from [14].

2.1.3 Pair production

At high energies, pair production becomes relevant. A schematic of the interaction is given in Figure 2.5. In the process of pair production, the high-energy photon (> 1.022 MeV) completely disappears and is replaced by an electron-positron pair. The positron range is short and will annihilate, producing two annihilation photons of energy 511 keV each. The interaction occurs in the electromagnetic field near the protons in the nuclei of the absorbing material atoms. For energies exceeding four times the rest mass of the electron, the interaction can also occur in the electromagnetic field of an electron [12]. The minimum photon energy required to produce the electron-positron pair is twice the rest mass of the electron. Therefore, the process of pair production will not occur for incident photons with energies lower than 1.022 MeV[7]. The energy of the electron and positron generated in the interaction is described by

$$E_{e^-} + E_{e^+} = h\nu - 2m_0c^2 \tag{2.9}$$

where E_{e^-} is the electron energy and E_{e^+} is the positron energy.
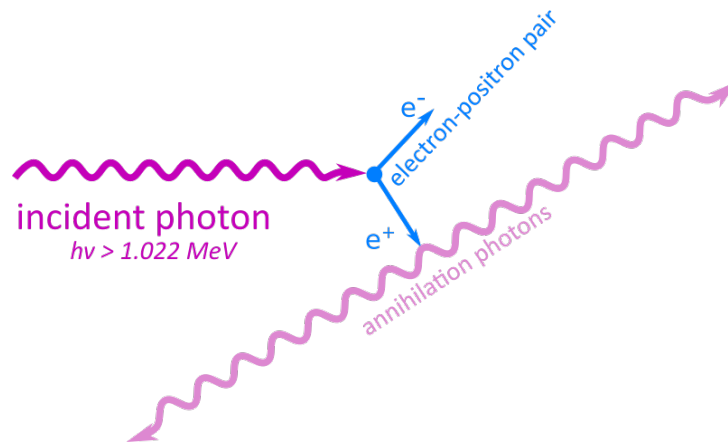
Figure 2.5: Schematic of the pair production interaction. The incident photon with an energy greater than 1.022 MeV is replaced by an electron-positron pair. The positron will shortly after the interaction annihilate, resulting in two photons of 511 keV each.

2.2   Basic principles of radiation detectors

The purpose of an X- and gamma-ray detector is to detect and measure high-energy photons as they interact with the detector material. When the radiation interacts with the bulk of the detector, it does so by one of the aforementioned interaction processes, causing a measurable quantity. This is referred to as the detector signal. By measuring and analyzing this signal by assistance of an external electronic circuit, it is possible to establish characteristics of the incoming photon. Due to the nature of high-energy radiation, there is currently no single detector design perfect for all applications. Detectors vary in detection method, operational mode, material, electrode geometry, design, and capabilities. However, a common framework for radiation detectors exist. In this section, some of the common detector characterization principles will be introduced. The features of the X- and gamma-ray spectrum for an arbitrary detector, on the basis of the three interaction processes, will be described. Finally, some of the most general detector principles will be briefly summarized.

2.2.1   Detector characteristics

The capabilities of a detector system depends on the specific detector design, operation, and material. The most simple detector types only count the number of photon interactions, with no information on interaction type, position, time, or energy. While other detectors possess spatial and spectral photon-by-photon detection. How well the detector collects the incident photons and resolves the energy, interaction position, and time, is described by the detector characteristics. In the following sections, some of the common detector specifications are described.

2.2.1.1   Full Width at Half Maximum

The resolution of a detector is conventionally characterized by the Full Width at Half Maximum (FWHM). If the detector is set to measure a quantity of a specific value, for example the energy of a monochromatic source, the spread in the actual measurement of the detector can be expressed by the FWHM. More specifically, the FWHM is the width of the measurement distribution, at half height of the measurement peak. This is illustrated in Figure 2.6, for a spectral measurement of a source with energy E_0. The resolution is then given by $R = \text{FWHM}/E_0$.
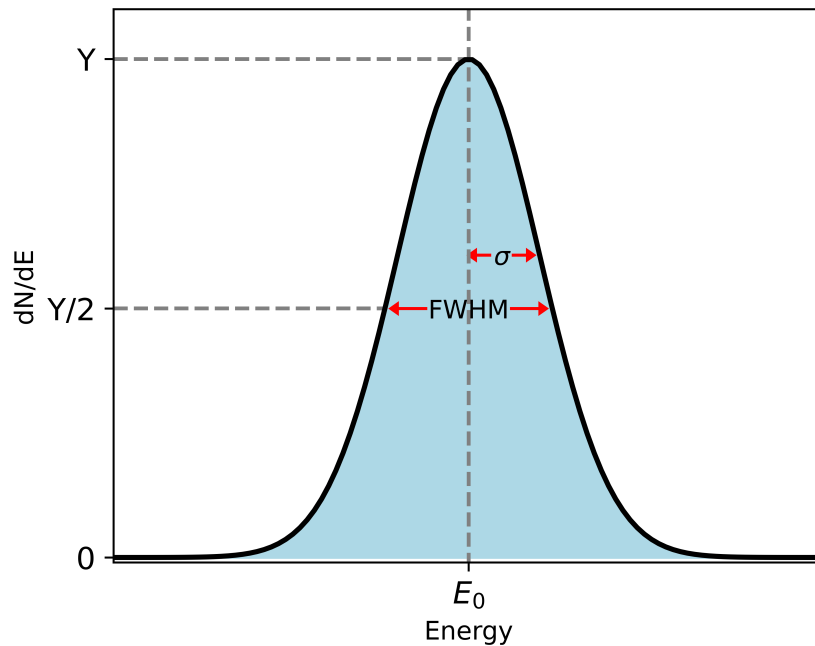

Figure 2.6: Definition of the FWHM measure to determine detector resolution. A Gaussian shaped peak will have the FWHM $= 2.35\sigma$.

2.2.1.2 Efficiency

The efficiency of a detector describes how well it records the emitted radiation quanta from a given source. Detector efficiency strongly depends on the detector material, the detector geometry, and the energy of the incident radiation. A thin detector with a bulk material of high stopping power can have a higher efficiency than one with a thick material of low stopping power.

The detector efficiency can be described by its absolute efficiency, $\varepsilon_{\mathrm{abs}}$, and its intrinsic efficiency, $\varepsilon_{\mathrm{int}}$. The absolute efficiency is dependent on the distance between the source and the detector, whereas the intrinsic efficiency is independent on the distance to the source. The two efficiencies are defined as follows [7]

$$\varepsilon_{\mathrm{abs}} = \frac{\text{number of recorded pulses}}{\text{number of radiation quanta emitted by source}},\tag{2.10}$$

$$\varepsilon_{\mathrm{int}} = \frac{\text{number of recorded pulses}}{\text{number of radiation quanta incident on detector}}.\tag{2.11}$$

The two efficiencies are related by the solid angle between the source and detector

$$\varepsilon_{\mathrm{int}} = \varepsilon_{\mathrm{abs}} \frac{4\pi}{\Omega}.\tag{2.12}$$

Ideally, the intrinsic efficiency of a detector is 100%. However, it is often seen that a detector is less than 100% efficient since X- and gamma-rays can penetrate large thicknesses of material without interacting.

2.2.1.3 Spectral resolution

The spectral resolution (or energy resolution) of a detector is a definition of how precise it can determine the energy of an incoming photon. The energy resolution of a detector can vary as a function of energy. There are three main contributors to the energy resolution of a detector, defined as follows:

- **Drift:** The drift contribution arises due to imperfections in charge carrier collection efficiency. As the charge carriers drift through the detector material towards collection they can be trapped or recombine, resulting in insufficient charge collection and thereby lost signal.

- **Noise:** The electronic readout system will introduce noise resulting in an uncertainty to the measured signal.

- **Statistical fluctuation:** The statistical noise in a detector system arises from the fact that there is a statistical spread in the number of charge carriers generated by an interaction. The statistical fluctuation contribution to the uncertainty in the energy determination represents the absolute minimum fluctuation which will always be present despite how perfect the rest of the detector is. It is the theoretical limit to the spectral resolution of a detector. The statistical limit to the resolution is given by [7]

$$R|_{\mathrm{Statistical\ lim.}} = 2.35\sqrt{\frac{F}{N}}\tag{2.13}$$

where F is the Fano factor [15] and N is the number of generated charge carriers.

These three contributors to the spectral response of the detector all have a certain dependency on the radiation energy. The drift contribution will increase as the incident radiation energy

increases, since more charges are generated, and thus more charges can be trapped. The electronic noise contribution is constant at all energies, and will therefore often be the dominating contributor for low energies. The statistical fluctuation contribution also increases as energy of the incident radiation increases, since the increased amount of charge carriers allow for larger statistical fluctuation.

The total measured spectral FWHM for the detector is the squared sum of each individual source to the FWHM [7]

$$(FWHM)^2_{total} = (FWHM)^2_{statistical} + (FWHM)^2_{noise} + (FWHM)^2_{drift} \cdots \qquad (2.14)$$

2.2.1.4   Spatial resolution

If the detector possesses the ability to quantify the interaction position of a photon in the detector volume, it has a spatial sensitivity. The spatial resolution (or position resolution) of the detector is also sometimes described as the "intrinsic spatial resolution" to underline the fact that it is the measurement of the interaction position inside the detector, and not its imaging capability.

Spatial sensitivity of a detector is often achieved through segmented electrodes, where the signal induced on the electrodes can be used to determine the interaction position. Some detectors only have a spatial sensitivity in one dimension, while others have in two or three dimensions. If the detector consists of strip electrodes on both sides, it is often the intersection of the two triggered electrodes that denotes the 2D position. In this case the spatial resolution will be equal to the strip pitch. Pixelated detectors can determine the position of the interaction from the collecting pixel, and thereby the spatial resolution is equal to the pixel size. In both cases, the detector would only be 2D sensitive. For a detector to have spatial sensitivity in 3D, the depth of the interaction in the detector must also be determined. This is often done either by measuring the drift time of the charge carriers, or by measuring the relationship between the induced signal on each side of the detector. Some detectors have even more sophisticated methods to determine the position resolution, and it is often evaluated experimentally and described by the FWHM of the measured interaction position.

2.2.2   Features of the X- and gamma-ray spectrum

The X- and gamma-ray interaction processes produce clear features in the spectrum measured by detectors with spectral sensitivity. For a monochromatic source, these features are especially recognizable in the spectrum. It is important to understand the detector response, since it contains valuable information about the radiation and how it interacts in the detector material.

In this section the most important distinguishable features of the X- and gamma-ray spectrum will be described.

2.2.2.1   Photoelectric absorption

As described in Section 2.1.1, a photoelectric absorption interaction results in the entire photon energy being deposited in the detector material. For a monochromatic source, the resulting response in the detector spectrum from photoelectric absorption events is the photopeak, see Figure 2.7. The broadening of the peak is governed by the energy resolution of the detector. If a significant amount of characteristic X-rays escape the detector, a second peak (the X-ray escape peak) will occur at a lower energy than the photopeak, at a distance corresponding to the characteristic X-ray energy. This is most probable for small detectors.

2.2.2.2   Compton scattering

The spectral response to Compton scattering measurements is illustrated in Figure 2.8. Since all scattering angles in the detector are probable for a specific incident photon energy, a range of energies will be deposited in the detector, resulting in a spectral shape referred to as the

Compton continuum. For low scatter angles, the deposited energy is close to zero, whereas for maximum scatter angles, the deposited energy is equal to the incident photon energy minus the maximum electron energy [7]

$$E_C = hv - E_{e^-}|_{\theta=\pi}. \tag{2.15}$$

The maximum energy of the Compton continuum is referred to as the Compton edge. In reality, the electrons are bound, which will have a rounding effect in the spectral shape of the Compton edge. This is however often overshadowed by the energy resolution of the detector which will also introduce a rounding of the Compton edge.
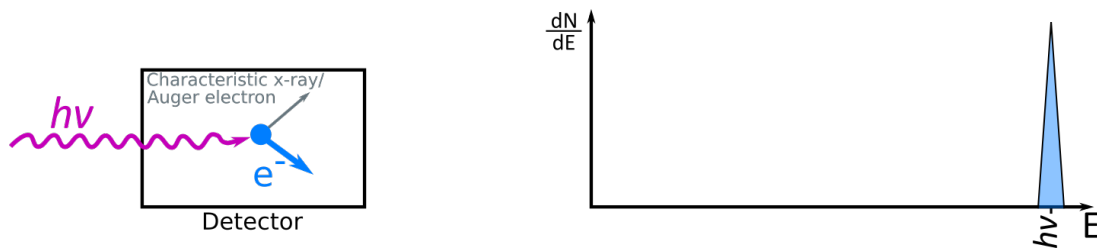
Figure 2.7: Spectral response of an energy-calibrated detector measuring only photoelectric absorption events. The source has a monochromatic energy of hv. In this case the characteristic X-rays do not escape the detector material.
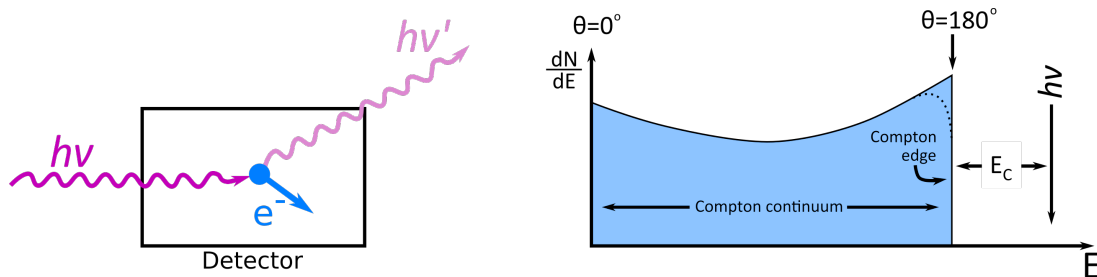
Figure 2.8: The spectral response of a detector measuring Compton scattering interactions where the scattered photon escapes the detector volume. The spectrum will display a Compton continuum of all the possible energies for the given photon incident energy. In the ideal case, the Compton edge will display a sharp edge. However, due to the bound electrons, and the fact that the detector has a finite energy resolution, the edge will round as illustrated by the dotted line.

2.2.2.3   Pair production

For the interaction of pair production to contribute to the photopeak of the spectrum, the two annihilation photons must interact by complete absorption. If one or both annihilation photons escape repeatedly, this will result in a feature in the detector spectrum, illustrated in Figure 2.9. If just one annihilation photon escapes repeatedly, a single escape peak will occur 511 keV below the incident photon energy in the spectrum. If both annihilation photons regularly escape the detector volume during measurement, the escape peak will be a double escape peak 1.022 MeV below the incident photon energy. Therefore, detectors measuring pair production must often consist of large detector volumes, to ensure the detection of the annihilation photons.

Figure 2.9: The spectral response of a detector measuring pair production interactions where either one or both annihilation photons escape the detector volume. This will result in the generation of a single and a double escape peak.

2.2.2.4   Passive material contributions

The above mentioned cases for a spectral response of a detector measuring monochromatic source radiation, did not consider passive material. Passive material refers to any material in the detec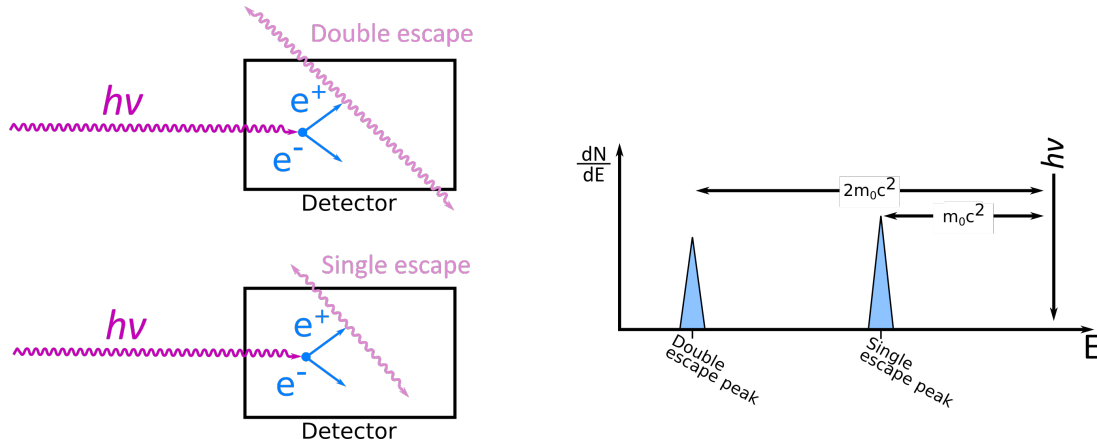tors vicinity that is not part of the sensitive detector itself. This can include, for example, electronics, shielding, and structural components. No detector system is free from passive material. If interactions occur often in the passive material, it may influence the spectral response of the detector. This also depends on which interaction types occur in the passive material:

- **Photoelectric absorption** events in the passive material can generate characteristic X-rays which then interact in the detector.

- **Compton scattering** in the passive material can result in scattered photons interacting with the detector material. In longer Compton scattering sequences, some of the interactions can be in the passive material, and some of them in the detector, resulting in missing signal.

- **Pair production** occurring in the passive material can result in annihilation photons interacting with the detector material. Annihilation photons generated in the detector can also escape and interact with passive material by Compton scattering, and scatter back to the detector. Furthermore, annihilation photons interacting by photoelectric absorption in the passive material can generate characteristic X-rays which then interact with the detector.

In this section a brief overview of the features of the X- and gamma-ray spectrum was given. The features present strongly depend on the source energy, detector material, and therefore interaction type. Being able to distinguish the features and interpret the detector response is essential, when it comes to detector development and characterization.

2.2.3   Detector types

In this thesis, the main focus is a semiconductor detector technology. However, a brief overview of other detector types will be given in this section, before the more thorough definition of semiconductor detectors. A combination of different detector types is normal in instrument development, since the choice of detector depends on requirements and applications.

Detectors can roughly be divided into two groups; direct and indirect detection. Detectors with direct detection specifically measure the generated charge carriers in the detector volume,

where detectors with indirect detection measure another secondary measurable quantity. In this section, some of the most common detector types will be described, based on [7].

The first three detectors described are all gas-filled detectors; thus, the detector bulk material is a gas. They all, in different ways, derive the electronic output signal from ion-pairs (a positive ion and a free electron) formed within the gas.

- **Ionization chambers:** This detector is the most simple form of a gas-filled detector. It operates by an applied electric field over the gas medium, and collects ion-pairs generated from radiation interactions in the medium.

- **Proportional counters:** This detector type is also a gas-filled detector, however, it makes use of the phenomenon "gas multiplication", where the charge from the original ion-pairs is amplified to create a larger signal. A strong electric field near the collecting anode results in an electron amplification, and therefore, the pulses are larger for this detector type compared to the ionization chamber.

- **Geiger-Mueller counters:** The Geiger-Mueller counter is a version of the proportional counter, however, it embeds far stronger electric fields. This results in an enhancement of the avalanche to a point where all pulses generated in the counter are of equal amplitude, regardless of the initial number of ion pairs. Therefore, this detector is not able to provide spectral information, but can exclusively be used as a counter.

The following two detectors are often used in combination with each other. The scintillator material itself does not detect the radiation, for this a photomultiplier is used.

- **Scintillation:** In the process of scintillation, the scintillator material emits visible light as X- and gamma-rays interact with the material. This weak light signal, generated from the interaction, can then be converted to an electrical signal.

- **Photomultiplier tubes and photodiodes:** This detector type converts the visible light signal from a scintillator material to a usable current pulse. This is done with embedded photocathodes converting the incident light photons into photoelectrons. The photoelectrons are then multiplied by an electron multiplier, amplifying the signal. At the end, the generated electrons are collected at the anode. The signal itself cannot be converted to a position finer than that of the scintillator material.

Finally, there is the semiconductor detector. The implementation of semiconductor materials in radiation detectors allows for the creation of a much larger number of carriers compared to any other detector type. The increase in information carriers per pulse reduces the statistical limit on the energy resolution. Therefore, the best possible energy resolution is achieved by semiconductor detectors.

- **Semiconductor detectors:** This detector type operates by the generation of electron-hole pairs in the detector material. They are drifted towards collection by an electric field and measured by an external electronic circuit. The material used and the electrode geometry vary widely, and many different semiconductor detectors exist. This technology will be introduced more thoroughly in the following section.

2.3   Semiconductor detectors

Semiconductor detectors (or solid state detectors) can be great for many applications. They achieve a much better energy resolution compared to that of scintillator detectors. This is due to the inefficiency in the generation of charge carriers in scintillator detectors. Using semiconductor detectors, the number of charge carriers per interaction is increased, and therefore reduces the

statistical limit to the energy resolution. In this section the overall theory of semiconductor detectors will be described.

Solid materials be can sub-grouped into metals and non-metals, where non-metals are comprised of insulators and semiconductors. The semiconductor material is an intermediate between the conductors and insulators, and holds a resistivity between $10^{-2}\Omega$cm and $10^8\Omega$cm [16]. The resistivity of the material governs whether it is classified as an insulator or a semiconductor. Therefore, the distinction between the two is vague, due to the conductivity being strongly affected by the temperature. The difference really depends on the temperature at which the materials are evaluated [16].

The bandgap of a material, separating the valance band and the conduction band, defines whether the material is a metal, semiconductor, or insulator. The valance band corresponds to the outer-shell electrons bound to explicit lattice sites in the material crystal structure. The next higher-lying band is the conduction band where the electrons can freely migrate through the crystal, thereby contributing to the material electrical conductivity [7]. In Figure 2.10 an illustration of the valance and conduction band of the different materials is shown. The semiconductor band gap is smaller than that of insulators, but larger than that of metals. For some semiconductors, the thermal excitation at room temperature will result in the elevation of electrons from the valance band to the conduction band and, therefore, need to be cooled to avoid this. Other semiconductor materials have a larger band gap and can therefore be operated at room temperature.

As X- or gamma-ray radiation interacts with the semiconductor material, it can elevate electrons from the valance band to the conduction band. In this process, electron-hole pairs are generated. The electron constitutes an electron elevated from the valance band to the conduction band. The hole represents the position of a missing electron in the valance band in the lattice structure of the crystal. These are the charge carriers generated along the path of the charge particle interactions in the detector. The motion of the electron-hole pairs in the applied electric field in the detector is what generates the detector signal [7].

In the following sections, the different aspects of a semiconductor detector will be described, from the detector bulk material, to the charge carrier properties, and finally, to the signal formation.
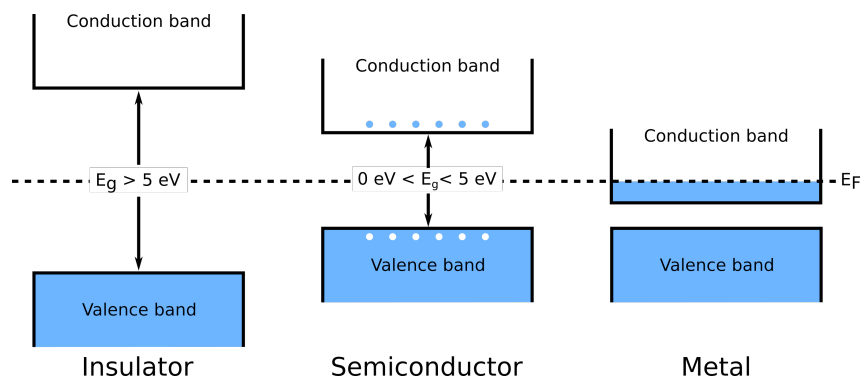
Figure 2.10: Schematic an insulator, semiconductor, and metal. In the metal electrons constantly occupy the conduction band. In the semiconductor, the bandgap is smaller than that of the insulator. Electrons can be elevated from the valance band to the conduction band.

2.3.1 Material

The semiconductor material used for the detector bulk is the fundamental specification of a semiconductor detector. This affects several aspects, such as operational temperature, charge carrier mobility and lifetime, radiation interaction cross section, and possible active bulk size.

The semiconductor material can consist of a single element or a compound of several elements. The material is described by the atomic number, density, and resistivity.

Possible semiconductor materials are plenty. Examples of single element materials which are widely used in radiation detectors are silicon (Si) and germanium (Ge). These materials can be manufactured pure in large bulk, and still possess excellent charge carrier transport properties. While these detector materials are widely used in various fields, they have their disadvantages. Silicon has a low stopping power, and germanium require cooling to cryogenic temperatures. The introduction of compound semiconductor materials are favorable due to their higher atomic number, resulting in an increase of the cross section of photoelectric absorption. Furthermore, several compound materials allow for room temperature operation with no or modest cooling, due to sufficiently large band gaps. Examples of compound materials are Cadmium Telluride (CdTe), Cadmium Zinc Telluride (CdZnTe), and Gallium arsenide (GaAs). The disadvantage of compound semiconductor materials are the poor hole mobility compared to the electron mobility. They often require either interactions only to occur close to the cathode side of the detector, or by operating the detectors as single polarity sensing, thus only depending on the electron signal.

Figure 2.11 illustrates the cross sections as a function of energy for Si, Ge, and CZT. Both Ge and Si have considerably smaller cross sections for photoelectric absorption. Already at 60 keV, Compton scattering becomes more dominant for Si. CZT has a larger cross section for photoelectric absorption compared to Ge and, at the same time, does not require cooling. However, charge transport properties of CZT are significantly worse, compared to Ge, especially for holes. Production of CZT is challenging, and can result in non-uniformity in the material, high defect density, and deep subsurface damages (grain boundaries).
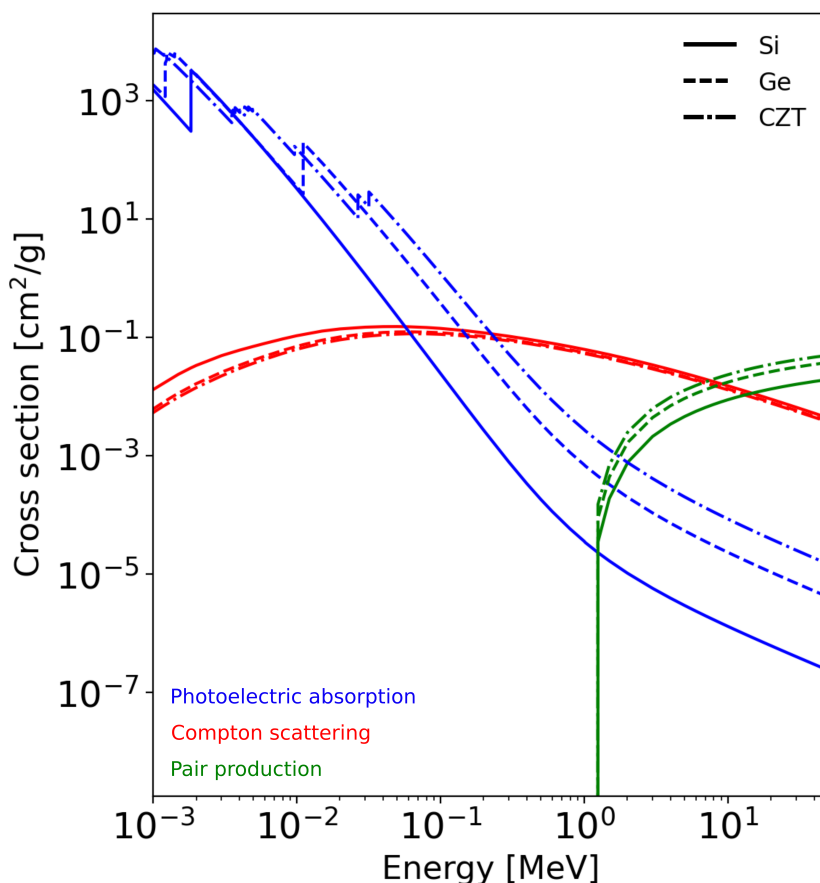

Figure 2.11: Si, Ge, and CZT cross sections for photoelectric absorption, Compton scattering, and pair production. Silicon has the lowest cross section for photoelectric absorption, where Compton scattering starts dominating already at 60 keV. CZT cross section for photoelectric absorption is slightly larger than that of Ge. Data extracted from [17].

2.3.2   Charge collection

When the high-energy photon interacts with the semiconductor material it results in the generation of electron-hole pairs. If an electric field, E, is applied to the semiconductor material, it will result in the motion of the charge carriers along the direction of the applied field, see Figure 2.12. Electrons will drift towards collection at the anode, while holes will migrate towards the cathode. The holes migrate when an electron leaves its normal valance site to fill the hole, and the new valance site is the new hole position [7].

The drift velocity of the electrons and holes, v_d, can for low to moderate electric field intensity be described by the electric field strength and the charge carrier mobility, μ.

$$v_{d,h} = \mu_h E \tag{2.16}$$
$$v_{d,e} = \mu_e E$$

where the subscript, e, denotes electrons and, h, holes. The drift time, t_d, it takes for a charge to traverse a distance, x, in the electric field is then given by

$$t_{d,e} = \frac{x}{v_e} = \frac{x}{\mu_e E} \tag{2.17}$$
$$t_{d,h} = \frac{x}{v_h} = \frac{x}{\mu_h E}.$$

The drift of the charges in the detector is governed by the mobility and lifetime of the charges in the given material. This will impact the amount of trapping the electron-hole pairs will experience towards collection. In the following sections these phenomena will be described.
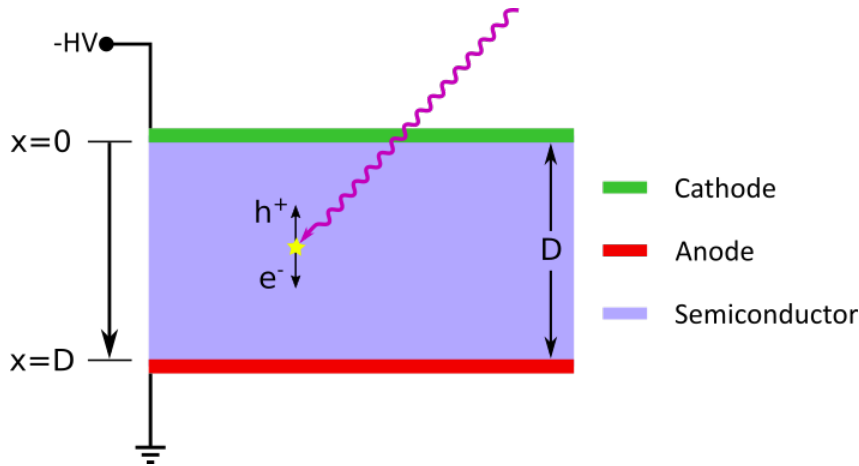
Figure 2.12: Illustration of a simple semiconductor detector. The interaction from a high-energy photon will generate electron-hole pairs. The electrons will drift towards collection at the anode, while the holes will drift towards collection at the cathode.

2.3.2.1   Trapping

When generated electron-hole pairs drift under the influence of an applied electric field in the semiconductor detector, they will do so until they are collected at the given electrode, recombine, or get trapped. Deep impurities in the material will trap and immobilize the charges for a longer period of time, where recombination centers will recombine electrons and holes. Both will result in the trapped or recombined carriers to not contribute to the measured signal, resulting in an attenuation of the signal.

A charge cloud, q_0, will decay over time, t, following the exponential expression

$$q(t) = q_0 \exp\left(\frac{-t}{\tau}\right) = q_0 \exp\left(\frac{-x}{\mu E \tau}\right) \tag{2.18}$$

where μ is the charge carrier mobility, and τ is the charge carrier lifetime.

K. Hecht described in 1932 [18] the relation between the charge collected at the electrode, and the initial generated charge by the photon interaction. This, he did in relation to the charge carrier drift length [19]. The two-carrier Hecht equation is given by [7, 19]

$$Q = eN_0 \left\{ \frac{\lambda_e}{D} \left[1 - \exp\left(\frac{x_i - D}{\lambda_e}\right) \right] + \frac{\lambda_h}{D} \left[1 - \exp\left(\frac{-x_i}{\lambda_h}\right) \right] \right\} \tag{2.19}$$

where N_0 describes the initial number of electron-hole pairs, e is the electron charge, x_i is the radiation interaction depth (measured from the cathode), D is the thickness of the detector, Q is the induced charge, and lastly λ is the trapping length [7]. The trapping length describes the mean distance a charge carrier travels before being captured. Ideally this measure must be greater than the thickness of the detector. The trapping length is given by

$$\lambda = \mu \tau E. \tag{2.20}$$

The Charge Collection Efficiency (CCE) of a detector system is described by the relation between Q and Q_0,

$$\text{CCE} = \frac{Q}{Q_0} \tag{2.21}$$

where Q_0 is the induced charge if the initial generated number of electron-hole pairs are all collected.

2.3.2.2 Carrier lifetime and mobility

While compound semiconductor detectors, such as CZT, holds the advantage of high atomic number serving higher stopping power, together with wider band gap to ensuring room temperature operation, they suffer from worse charge transport properties. The charge transport of holes in CZT is extremely poor and will strongly affect the spectral resolution, if spectral measurements rely on the hole contribution to the signal.

The charge carrier transport properties of a material are described through the charge carrier lifetime, τ, and mobility, μ. The charge carrier lifetime is given in units of [s]. It describes the rate of trapping the charge carriers experience, as they drift from origin towards the collecting electrodes. The charge carrier mobility is given in units [cm^2/Vs]. It is a measure of the influence of an an applied electric field on the charge motion in the bulk of the material. The larger the μ the better mobility in the bulk. A decrease in charge mobility implies an increase of impurity concentration in the material. Electron and hole mobility of Si and Ge are significantly larger than that of CZT, and the two carrier mobilities are roughly equal. For CZT, the hole mobility is much worse than the electron mobility [7]. Often when defining the quality of a semiconductor material, it is described by the product of mobility and lifetime, specified by the $\mu\tau$-product.

When determining the $\mu\tau$-product of a detector bulk, measurements are taken at varying applied voltage biases (V). This varies the electric field strength inside the detector between measurements, and thereby affects the electron drift time and amount of charge trapping. The methods often make use of pulse shape analysis of current or charge signals, generated in the detector as it is irradiated by a laser pulse, α-particles, or an X-ray source [19, 20].

The conventional method for assessing the $\mu\tau$-product of a detector bulk relies on fitting the Hecht equation (Eq. 2.19). However, this method requires a curve fitting procedure and tends to underestimate the $\mu\tau$-product [21].

Other methods exist for determining the charge carrier properties. A direct measurement method to determine the transport properties for electrons was presented by He et al. [22]. This method extracts the $\mu_e\tau_e$-product from the electric field strength, electron drift distance, and photopeak position using a single polarity sensing detector, using the relation

$$\ln\left(\frac{N_1}{N_2}\right) = \frac{y_d}{\mu_e\tau_e}\left(\frac{1}{E_2} - \frac{1}{E_1}\right) \tag{2.22}$$

where N_1 is the photopeak position measured with an electric field strength of E_1, N_2 is the photopeak position measured with an electric field strength of E_2, and y_d is the electron drift distance.

Bolotnikov et al. [21] presented a method for extracting the electron drift time utilizing the relation between the photopeak position and electron drift time at different operational bias voltages

$$\ln\left(\frac{N_1}{N_2}\right) = \frac{1}{\tau_e}\left(t_{d2} - t_{d1}\right) \tag{2.23}$$

where t_{d1} is the electron drift time measured at an electric field strength E_1 and t_{d2} is the electron drift time measured at an electric field strength E_2.

When determining μ by its own, the time of flight (TOF) method is often applied [19, 20]

$$\mu = \frac{y_d}{Et_d}, \tag{2.24}$$

in this method the charge carrier mobility is extracted by knowing the drift distance, y_d, E is the applied electric field strength, and t_d is the charge drift time.

2.3.2.3 Diffusion

As the charge carrier drifts, the charges will be influenced by diffusion. Diffusion is the process of random thermal motion, resulting in the charges diffusing away from their original position. As the electron-hole pairs drift towards collection, they will ideally follow the exact electric field lines connected to their original position towards the collecting electrode. However, due to diffusion, a spread in the arrival position is introduced. The broadening of the charge cloud, due to diffusion, can affect the precision of which the position measurement can be made.

2.3.3 Leakage current

Even in the case where no ionizing radiation interacts with the detector material, a small current will flow in the semiconductor, caused by the application of the high voltage. This is leakage current. It can be divided into two contributors:

- **Bulk leakage current:** The leakage current in the bulk of the semiconductor material is the flow of current through the material itself.

- **Surface leakage current:** The leakage current on the surface of the semiconductor material is the flow of leakage between electrodes. It is especially problematic when the electrodes are close.

It is important that the contribution to the current signal from the leakage current is small compared to the contribution from radiation interaction.

2.3.4 Signal formation and the Shockley-Ramo theorem

The induced signal in the detector arises due to the fact that the charge carriers move in the electric field after they are generated by the incident photon interaction. The motion of the carriers induces the signal from the point where the charges start moving, until they are collected at the electrodes. The signal formation timeline is as follows:

1. An incoming photon deposits energy in the detector material through photoelectric absorption, Compton scattering or pair production, resulting in the generation of electron-hole pairs.

2. The charge, q, starts to move, which results in an induced charge, Q, on the detector electrodes.

3. The process of inducing the signal lasts until the charges are collected at the electrodes, and the pulse is fully developed.

The conventional way of calculating the induced charge starts with solving the Poisson equation [7]

$$\nabla^2 \varphi = \frac{\rho}{\epsilon} \tag{2.25}$$

where the electric potential is denoted φ, the charge density is denoted ρ and, finally, the dielectric constant of the detector medium is denoted ϵ. The charge density can vary within the detector volume. Assuming no charges are trapped, the charge density is $\rho = 0$ and the Poisson equation reduces to the Laplace equation

$$\nabla^2 \varphi = 0. \tag{2.26}$$

After choosing the Laplacian operator, ∇^2, appropriate for the given detector geometry, and defining the relevant boundary conditions, the equation must be solved. For complex geometries and detector shapes, this requires numerical techniques provided by computer software. From this, a numerical solution for the electric potential φ anywhere in the detector medium is obtained [7]. From this information, the electric field at any point can be derived by

$$E = -\mathrm{grad}\varphi. \tag{2.27}$$

To calculate the induced charge, the instantaneous electric field, $\mathbf{E}$, must be calculated for each point of the moving charge, q, along its path, and then calculating the induced charge Q by integrating the normal component of $\mathbf{E}$ over the surface $\mathbf{S}$ of the electrode [23]

$$Q = \oint_S \epsilon \mathbf{E} \cdot d\mathbf{S}. \tag{2.28}$$

This process is tedious. However, understanding the signal formation in a detector is crucial when it comes to optimizing the measurement quality of time, energy, position, and shape. The detector technology must be optimized both in topology and readout, for the desired application of the detector.

A more general and much more simple method was independently developed by both Shockley [24] and Ramo [25]. In this method, the induced charge on the electrodes in a detector from the motion of the charge carriers can be calculated using what is referred to as the *weighting potential*, φ_0. In this theorem, it is stated that the induced charge on a given electrode, is equal to the product of the carrier charge and the difference in the weighting potential from the beginning to the end of the carrier path [7]. The weighting potential is not a real physical potential in the detector, but a mathematical tool to simplify the process of calculating the induced charge. The weighting potential can be found as a function of position by solving the Laplace equation for the given detector geometry, with the following artificial boundary conditions [7]:

1. The voltage of the electrode for which the induced charge is to be calculated must be set equal to 1.

2. Voltages for all other electrodes are set to zero.

3. Trapped charges in the detector volume is ignored, thus solving the Laplace equation, Eq. (2.26), instead of the Poisson equation, Eq. (2.25).

The induced signal from a charge moving from $\mathbf{x}_i$ to $\mathbf{x}_f$ is then, using the Shockley-Ramo theorem, calculated by

$$\Delta Q = -q[\varphi_0(\mathbf{x}_f) - \varphi_0(\mathbf{x}_i)]. \tag{2.29}$$

Thereby, the induced signal can easily be calculated, using the concept of weighting potentials. The total induced signal, Q_{tot}, will be the sum of the electron contribution, Q_e, and hole contribution, Q_h,

$$Q_{tot} = Q_e + Q_h. \tag{2.30}$$

The weighting potential distribution in a detector describes how a charge carrier induces a signal as it drifts toward collection. While the charge carrier drifts through the detector towards the collection point, it induces charge on all electrodes. The amount of charge induced depends on the distributions of the weighting potentials. In Figure 2.13, the calculated weighting potentials for a pixel detector are displayed. Figure 2.13(left) illustrates the detector geometry with a planar cathode and pixelated anodes. In Figure 2.13(right), the calculated weighting potentials as a function of detector depth are shown. These calculations are performed along the axis perpendicular to the center of the central pixel, P_1. The weighting potential for the case of a planar anode is provided for comparison. The weighting potential of a planar anode results in a linear distribution throughout the detector medium. In contrast, the weighting potential for P_1 is more concentrated in the vicinity of the pixel. Weighting potentials for the two pixels next to P_1 are also presented. The weighting potentials of these electrodes are not zero; therefore, transient signals are induced at neighboring pixels even as the charge moves toward collection at P_1.
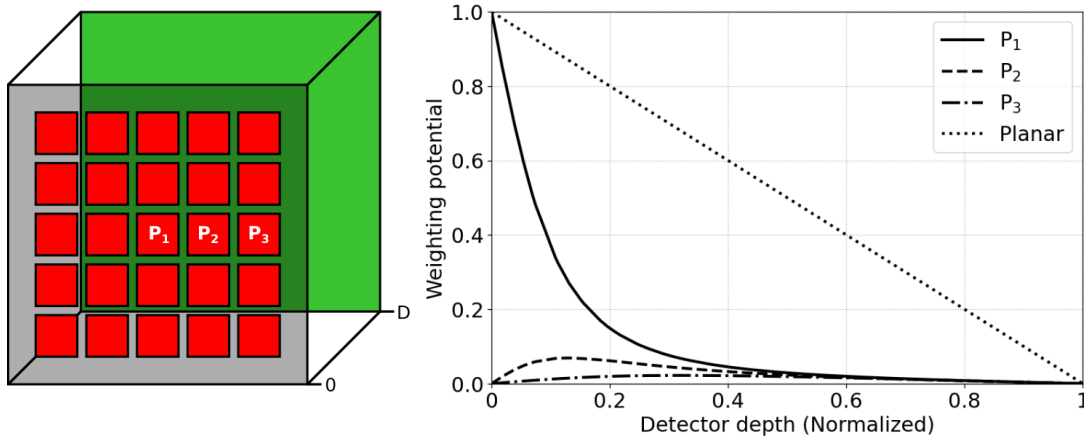
Figure 2.13: (Left) Depiction of a pixel detector configuration featuring pixelated anodes (red) and a planar cathode (green). (Right) The graph shows the calculated weighting potentials for three pixels calculated along the axis perpendicular to pixel P_1. All pixels have sizes that are 10% of the detector thickness.

The more compact weighting potential close to the pixelated anode is attributed to the small pixel effect. The smaller the ratio between the electrode size and detector thickness, the more compact the weighting potential will be near the electrode. The small pixel effect is illustrated in Figure 2.14. In this figure, the weighting potential for a pixel is calculated perpendicular to the center of the pixel. It is calculated for three cases where the pixel size is 10%, 20%, and 40%

of the detector thickness. It is evident that the weighting potential becomes more compact as the pixel size decreases.

Figure 2.14: Plot of the weighting potentials related to three different pixel electrode sizes. As the pixel size decreases (with respect to detector thickness), the small pixel effect is increased [7].

As stated in Eq. (2.30), the total induced signal on an electrode is the sum of the signals induced by each of the two charge carriers. Therefore, if one charge carrier experiences significant trapping, it will have a significant impact on the total induced charge [23].
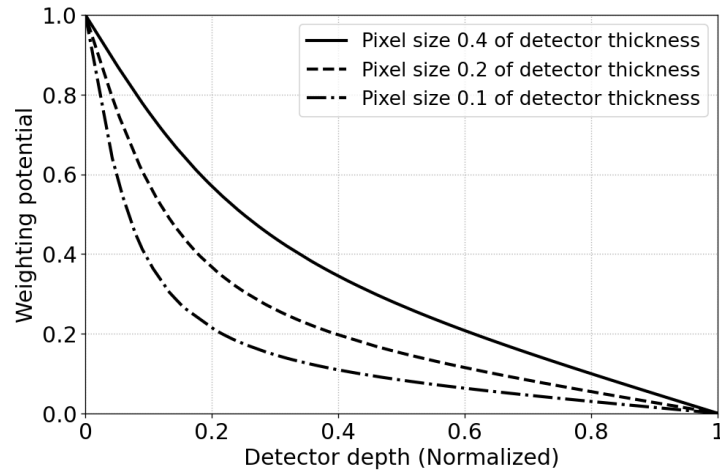
Consider the case of a planar semiconductor detector, as shown in Figure 2.15(a). A gamma-ray photon interacts at position x in the detector. The generated electrons drift towards collection at the anode, and the holes drift towards collection at the cathode. In Figure 2.15(b), the corresponding weighting potential for the planar anode is displayed, which is linear throughout the depth of the detector. In Figure 2.15(c), two cases for the corresponding measured energy spectrum are provided. In the case where electrons and holes experience no trapping, a photopeak will appear at the incoming photon energy. In the case where holes have little to no mobility, the resulting spectrum will instead be a distribution of energies ranging from zero to hv. The poor hole mobility in a material such as CZT will, therefore, have a negative impact on the spectral response of a planar detector. However, the small pixel effect can be utilized to
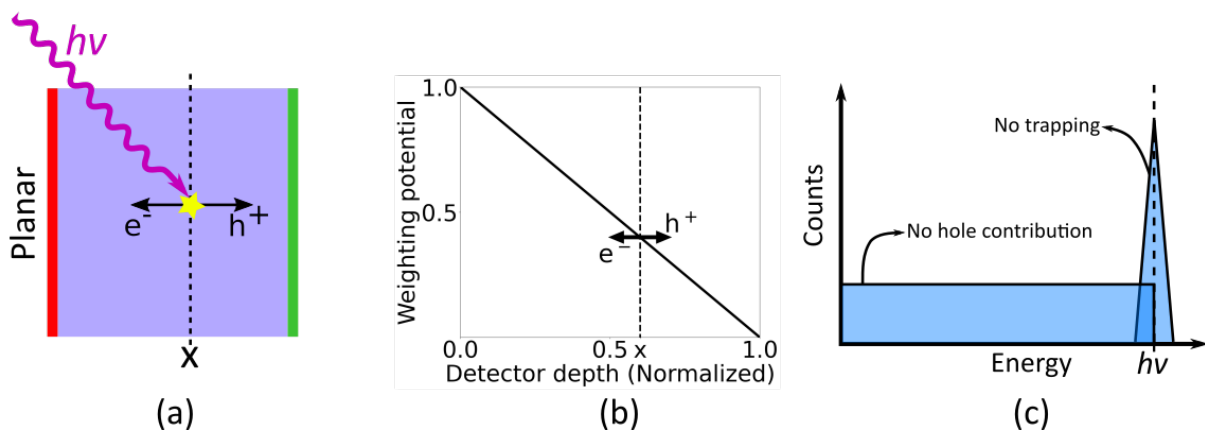

Figure 2.15: An illustration of: (a) a planar detector with the anode (red), cathode (green), and a gamma-ray interaction, (b) the weighting potential of the anode and the photon interaction position, along with the drift direction of the two charge carriers, (c) the resulting energy spectra for the case where no trapping occur, and the case where the holes do not move.

mitigate this issue.

Consider instead the case of a pixelated detector in Figure 2.16(a). In this case, the small pixel effect on the collecting anode results in a more compact weighting potential close to the collecting anode, as depicted in Figure 2.16(b). Most of the signal is induced as the charges drift close to collection at the anode, and therefore, the contribution of holes to the signal is reduced. In Figure 2.16(c), an illustration of the resulting energy spectrum is shown. A clear photopeak will be visible. Some tailing to the left of the photopeak can occur due to interactions happening close to the anode, where the electrons will not traverse the full weighting potential.
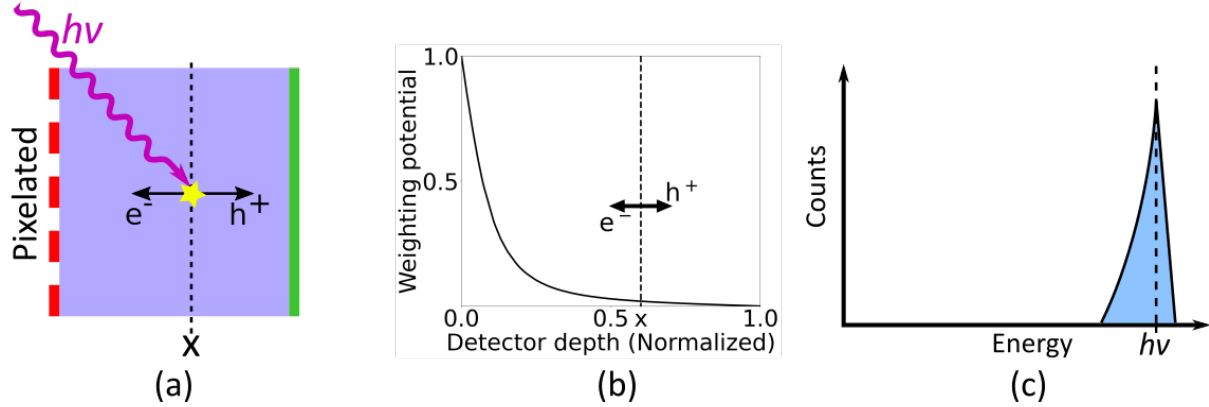
Figure 2.16: Illustration of (a) a pixel detector with anode (red) and cathode (green), and a gamma-ray interaction. (b) Illustration of the weighting potential of the anode, and the photon interaction position together with drift direction of the two charge carriers. The pixel size is 10% of the detector thickness. (c) The resulting energy spectrum, with no hole contribution. A tailing effect can be seen left of the photopeak. This is contributed from photon interactions close to the pixel side of the detector, where the generated electrons do not traverse the full weighting potential.

The weighting potentials are not actual physical potentials within the detector but rather mathematical tools used to calculate the induced signals. These tools are powerful and must be employed when designing the electrode geometry, as they have a significant impact on signal formation within the detector. Specifically, the small pixel effect and the potential to reduce the contribution of hole movement are foundational concepts in the 3D CZT drift strip detector, which will be described in Chapter 4. However, before introducing the 3D CZT drift strip detector, the following chapter will provide insight into scientific instruments for X- and gamma-ray astronomy.

3 Scientific Space Instruments for X- and Gamma-ray Astronomy

The detection of light is essential to understanding our Universe. Observatories on Earth and in space make use of dedicated instrumentation, designed specifically for the light they examine. Figure 3.1 illustrates the penetration depths of light in the Earth's atmosphere along the electromagnetic spectrum. Therefore, whether an observatory should be ground based or spaceborne depends on the light to be examined. X- and gamma-ray radiation from space does not reach the surface of the Earth, consequently observatories must be on balloon flights or in space. Observatories for very high-energy gamma-ray radiation can be ground-based by detecting secondaries generated in the interaction between the high-energy gamma-rays and the Earth's atmosphere.

Light in the X- and gamma-ray domains of the electromagnetic spectrum spans a broad range of energies. As described in Section 2.1, this light interacts in different ways depending on its energy and the detector material. Therefore, various instrument designs and imaging methods exist for X- and gamma-ray astronomy. The optimal method depends on the energy range of the light and the scientific requirements of the instrument. In this chapter, some common instrument types used for X- and gamma-ray astronomy will be reviewed. This review includes a brief summary of the instrument concepts, the types of detectors used, and examples of instruments that have been used in the past or are currently in operation. Finally, a prospect is given.
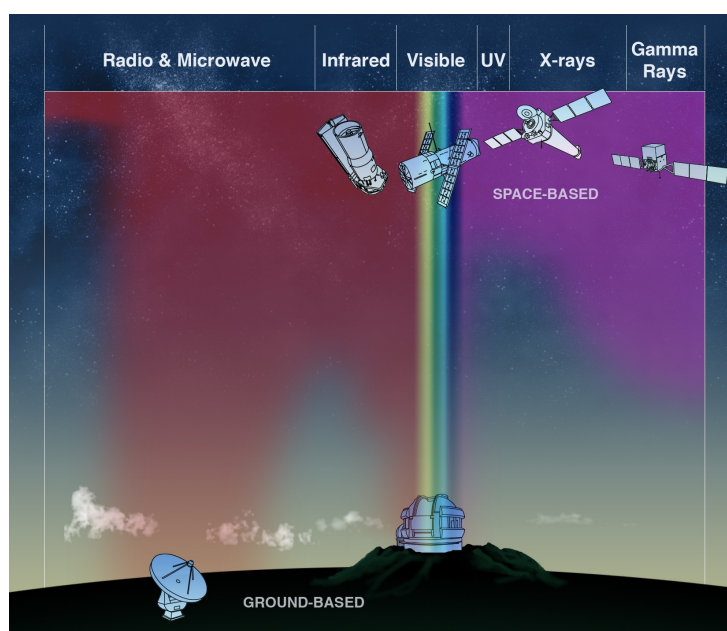
Figure 3.1: Instruments observing the electromagnetic spectrum are either ground based or spaceborne, depending on the penetration depth of the radiation in the Earth's atmosphere. X- and gamma-rays do not penetrate the atmosphere, so observatories must either be in space or carried by balloons. High-energy gamma-rays can be observed from the ground by studying the secondaries generated when gamma-rays interact with the Earth's atmosphere. Image credit: *NASA/CXC/M.Weiss.*

3.1 Coded mask instrument

The coded mask instrument is a technique that resembles that of a pinhole camera, as illustrated in Figure 3.2. This instrument couples a mask, with a unique pattern, placed at a distance above a position-sensitive detector plane. The mask absorbs some of the incident radiation, resulting in a shadow image on the detector plane. This shadow image is used to reconstruct the original location of one or more sources. The technique is especially useful in the hard X-ray band (10-100 keV) but can also be applied to low-energy gamma-ray (100 keV-10 MeV) observations. However, when the energy increases above a few MeV, the mask becomes more transparent, and

the Compton interaction process becomes dominant, rendering the technique ineffective [26]. The possibility of a broad energy range, combined with a wide field-of-view (FoV), makes the coded mask aperture particularly well-suited for monitoring the transient sky. One disadvantage of this instrumentation type is a low signal-to-noise (S/N) ratio, which is attributed to the non-focusing nature of the instrument and its large detector area.
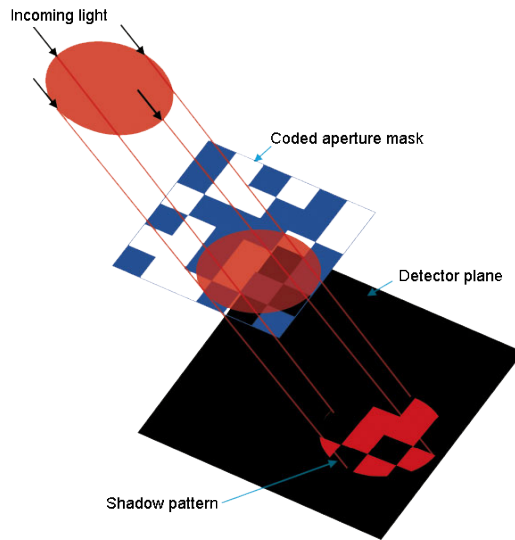

Figure 3.2: Illustration of the coded aperture imaging technique. A coded mask is positioned above the detector plane at a certain distance. The mask creates a shadow pattern of the incoming radiation on the detector plane. This unique shadow pattern can then be used to reconstruct the image. Image credit: *NASA*.

Coded aperture imaging has been successfully implemented in several spaceborne observatories, utilizing various types of detectors, including gas-filled microstrip detectors, semiconductor detectors (both single and compound), and scintillator detectors. Examples of observatories that have utilized coded aperture imaging include:

- **ASIM (Atmosphere-Space Interactions Monitor):** The "Modular X- and Gamma-ray Sensor" (MXGS) on board ASIM [27], launched in 2018 and is still in operation as of September 2023. The instrument consists of a layer of pixelated CZT detectors for low-energy detection and a layer of Bismuth Germanate (BGO) scintillators coupled to photomultiplier tubes for high-energy detection. The coded mask absorbs low-energy photons, producing a shadow pattern on the CZT detectors within an observational range of 15-400 keV. DTU Space is the Principal Investigator (PI) of the ASIM mission. Furthermore, DTU Space were responsible for design, characterization, and selection of the CZT crystals used for the MXGS instrument [28]. The mission primarily focuses on observing upper atmosphere thunderstorms on Earth [29, 30], but it has also observed a giant flare from a magnetar [31].

- **INTEGRAL (The INTErnational Gamma-Ray Astrophysics Laboratory):** INTEGRAL, launched in 2002 and is still in operation as of September 2023, with a planned reentry in 2029. It features three coded mask instruments. SPI (Spectrometer on INTEGRAL) observes in the energy range of 18 keV to 8 MeV using Ge semiconductor detectors cooled to 85K. IBIS (Imager on Board the INTEGRAL Satellite) combines CdTe semiconductor detectors and Caesium iodide (CsI) scintillator detectors to observe in the range of 15 keV to 10 MeV. Finally, JEM-X (The Joint European X-Ray Monitor) consists of two microstrip gas detectors and observes in the energy range of 3-35 keV [32]. DTU Space (formerly the Danish Space Research Institute) was a major contributor as a PI of the JEM-X instruments onboard INTEGRAL [33]. Throughout its lifetime, the INTEGRAL mission has made significant contributions to astrophysics. Two notable examples include the discovery of gamma-ray bursts in relation to gravitational waves from a kilonova [1, 34] and the detection of a significant number of new X-ray sources [35].

- **Swift (Neil Gehrels Swift Observatory):** Swift was launched in 2004 and remains operational as of September 2023. The "Burst Alert Telescope" (BAT) on board operates in the energy range of 15-150 keV and consists of a coded mask with pixelated CZT detectors. The BAT instrument has observed more than 1300 GRBs [36].

3.2   Focusing telescope

Another technique that can be employed in the X-ray regime is focusing optics. Focusing X-rays differs significantly from conventional focusing techniques at lower energies and are often referred to as grazing incidence optics. An illustration of a nested Wolter-type X-ray focusing optics is provided in Figure 3.3. The mirrors are frequently arranged in such a nested manner to increase the collecting area. Various mirror curvatures are used to focus the X-rays in a double-bounce configuration, with the Wolter-I configuration being a common choice for astrophysical applications. The X-ray reflectance is enhanced by depositing thin film coatings that alternate between materials with high and low atomic numbers. The detector is mounted at a distance from the focusing mirrors, known as the focal length, where the radiation is focused onto the detector plane. Focusing the source flux onto a smaller detector area, in a background dominated observation, will improve sensitivity drastically by increasing S/N ratio [37, 38]. Common for instruments using X-ray optics is that they observe in the low-energy X- and gamma-ray range. Currently, no focusing optics instruments above 79 keV are operational in space [39]. Efforts are made to advance the technology into higher energies, for example, the proposed instrument HEX-P (High Energy X-ray Probe) observing in the energy range 0.1-150 keV (as of September 2023) [40].
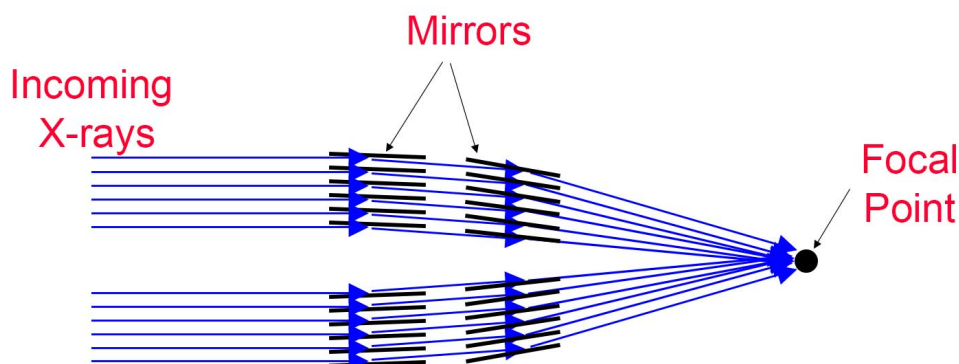
Figure 3.3: Illustration of an X-ray telescope mirror configuration. Credit: *NASA's Imagine the Universe.*

Focusing X-ray optics have been successfully implemented on several space observatories. Some examples include [38]:

- **Chandra:** The Chandra telescope was launched in 1999 and is a Wolter-I focusing optics telescope. It operates in the energy range of 0.1-10 keV and is equipped, among other, with Charged Coupled Device (CCD) detectors [41].

- **XMM Newton:** XMM Newton, also launched in 1999, observes in the energy range of 0.1-12 keV with embedded CCD detectors. It has a larger effective area than Chandra, allowing for spectroscopic studies of fainter sources [42].

- **Swift (Neil Gehrels Swift Observatory):** The Swift telescope also includes the X-ray telescope (XRT), which consists of Wolter-I X-ray optics and a CCD detector. It observes in the energy range of 0.2-10 keV [43].

- **NuSTAR (Nuclear Spectroscopic Telescope Array):** NuSTAR, launched in 2012, is currently the X-ray focusing telescope observing at the highest energies, with an observational range of 3-79 keV. It utilizes pixelated CZT detectors and CsI scintillator detectors for anti-coincidence shielding [39].

Efforts are made within development of other techniques of focusing X-rays, such as Laue/Fresnel lenses, or Lobster eye optics.

3.3   Compton camera

In the 1960s, most instruments used for X- and gamma-ray astronomy were based on photoelectric absorption or pair production [3]. These instruments proved to be inefficient in the MeV domain, where the dominant interaction mechanism is Compton scattering, described in Section 2.1.2. A dedicated effort to measure both the energy and positions of Compton interactions led to significant progress in developing a more sensitive telescope for the MeV domain, namely the Compton telescope or Compton camera. Such an instrument utilizes the Compton scattering interaction for imaging.

An illustration of the Compton camera concept is provided in Figure 3.4. The Compton camera comprises a volume of spectral and spatially sensitive detectors that record the energy and position of multiple Compton scattering interactions. This information enables the recovery of the original energy and direction of the incoming photon. When measuring the energies and positions of a fully constrained event, it is possible to restrict the position of the source to a cone (event circle) in the sky with an opening angle denoted as θ. As multiple photons from the same source are measured, the event circles overlap in the image space, revealing the location of the source. However, a challenge with the Compton camera lies in the requirement for the photon to be fully absorbed. Deriving the direction and energy of the initial gamma-ray solely from the first Compton interaction is not possible. Furthermore, recording the position and energy of every single Compton scattering event is necessary to reconstruct the interaction [3]. The angular resolution of the Compton camera is described by the Angular Resolution Measure (ARM), which is the smallest angular distance between the actual origin of the photon, and the event circle [12].
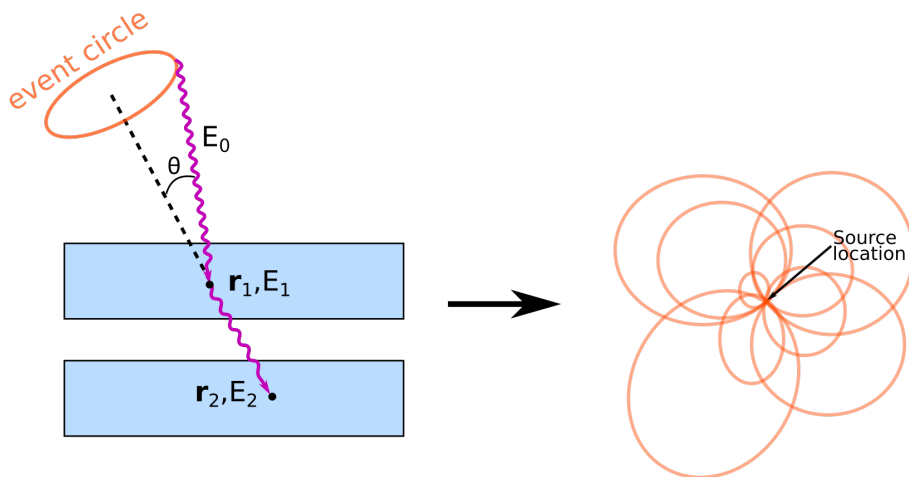
Figure 3.4: Illustration of a Compton camera measuring a two-site event: A Compton scattering event followed by a photoelectric absorption event. The incoming photon energy, denoted as E_0, is determined from the two interactions by $E_0 = E_1 + E_2$, and the event circle is determined from the Compton scattering angle θ of the first interaction. Multiple interactions result in several event circles. The overlap of these event circles reveals the location of the source [3].

The types of Compton telescopes can be roughly divided into three categories [3, 12], which are also summarized in Figure 3.5.

(a) **The Classic Compton Camera** consists of two detector planes, separated enough to measure the TOF of the scattered gamma-ray. The first plane is the scatter layer, where the Compton scattering interaction occurs before it is fully absorbed by photoelectric absorption in the absorber layer (collimator). The configuration is illustrated in Figure 3.5(a).

(b) **The Compact Compton Camera** consists of one or more 3D position-sensitive detectors, allowing for the measurement of multiple Compton scattering interactions. The configuration is illustrated in Figure 3.5(b).

(c) **The Compton Camera with Electron Tracking** utilizes many thin layers of detectors, enabling the measurement of the recoil electron track. This telescope type is also sensitive to pair production events by measuring the electron and positron trajectories. The configuration is illustrated in Figure 3.5(c).

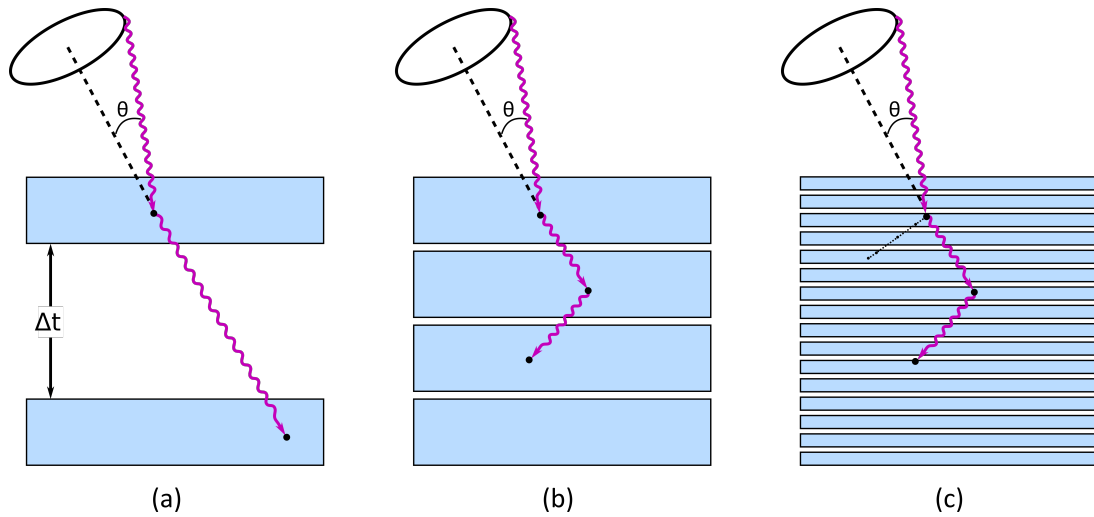**Figure 3.5:** Illustration of the three overall Compton camera configuration types. (a) Classic Compton camera (b) Compact Compton camera (c) Compton camera with electron tracking.

In the classical Compton camera design, differentiation between events starting at the top or bottom is possible. However, only two interactions are measured. In the compact Compton camera, several (more than two) Compton scattering interactions are measured, providing redundant information. This redundant information is then used to order the interactions using Compton sequence reconstruction methods. In the last telescope type, where the electron track is also known, it is possible to reduce the reconstructed cone to a segment of the cone. There are several advantages to using a Compton camera. Firstly, it utilizes the dominant Compton scattering interaction in the MeV regime, increasing the telescope sensitivity. Additionally, it offers a large FoV. The telescope is also sensitive to polarization, as described in Section 2.1.2.2, and only a few photons are required to recover the source position if the background is effectively suppressed. However, the original photon is measured multiple times, introducing uncertainty for each measurement, which is then propagated into the recovery of the photon's origin and energy. The design can become extremely complex and requires the use of intricate reconstruction algorithms. Furthermore, Doppler broadening introduces a fundamental limit to the achievable ARM [12], as described in Section 2.1.2.1. Ultimately, the Compton camera is only as good as its event reconstruction algorithms and its suppression of background.

Few Compton cameras have been deployed in spaceflight. However, it might be a good candidate for MeV astronomy instrumentation to improve sensitivity. Examples of a previous and a future instrument are:

- **CGRO (NASA's Compton Gamma Ray Observatory):** The first Compton camera to successfully operate in space was COMPTEL [44], an instrument on board CGRO, which was operational from 1991 to 2000 [3]. The detector configuration followed that of the classic Compton camera. The first detector layer consisted of a low atomic number scintillator detector to enhance Compton scattering cross section, and the second detector layer contained a high atomic number scintillator to enhance the cross section of photoelectric absorption [3]. The instrument's energy range was 0.75-30 MeV, covering the MeV range. Although the instrument's sensitivity was modest, COMPTEL made groundbreaking scientific contributions [3, 45].

- **COSI (The Compton Spectrometer and Imager):** The COSI instrument is a Compton telescope planned for launch in 2027 [46]. It is designed for the energy range of 0.2-5 MeV. The instrument consists of 16 strip Ge detectors with a position resolution of 1.5 mm^3, along with an anti-coincidence shield made of BGO scintillators with photomultiplier tubes for readout. Additionally, a mechanical cryocooler is used to cool the Ge detectors.

3.4　Pair telescope

As the name indicates, the pair telescope is designed to detect and measure pair production interactions. Some pair telescopes are just counters, where other also posses imaging capabilities. Many different pair telescopes have been constructed, and they can vary in design. An illustration of a typical pair conversion instrument design is given in Figure 3.6. It is a layered instrument consisting of conversion layers, with material properties that increase the probability of a photon undergoing a pair conversion interaction in the material. Spatially sensitive detectors are then used to track the movement of the electron-positron pairs. Finally, the electron-positron pairs deposit the remainder of their energy in the calorimeter. The measured tracks and final energy deposit are then used to assess the total energy and direction of the incident photons. The dominant cosmic ray background is managed by an anti-coincidence system located above the tracker and calorimeter [47].
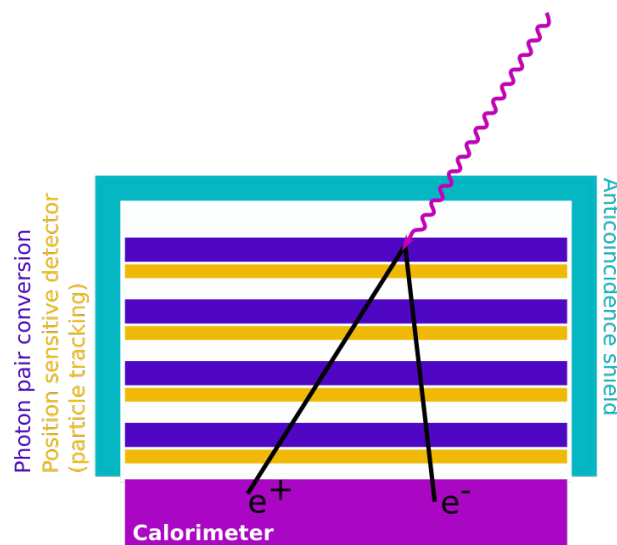

Figure 3.6: Illustration of a pair telescope design. Passive material layers of high atomic number provide a bulk where pair production interactions can occur. Position sensitive detectors then track the generated electrons and positrons, before they deposit the remainder of their energy in the calorimeter.

Many pair production instruments have been operated, either in balloon flight or in space. Two examples of important instruments using pair conversion are:

- **CGRO (NASA's Compton Gamma Ray Observatory):** EGRET (The Energetic Gamma Ray Experiment Telescope) [48] was a pair production telescope on board CGRO, which was operational from 1991-2000. The energy range of EGRET was 20 MeV-30 GeV.

- **Fermi-LAT:** The Large Area Telescope (LAT) [49] on board the Fermi-LAT (formerly known as "the Gamma-ray Large Area Space Telescope", GLAST) is a pair conversion gamma-ray telescope. It is still in operation as of September 2023. It consists of Si strip detectors for tracking, CsI Scintillator arrays as the calorimeter, and anti-coincidence scintillator detectors.

3.5 Prospect

The aforementioned instrument types clearly illustrate that energy of the light and mission requirements require vastly different approaches. The choice of detector chosen to fly on board a space mission will therefore also be driven by the science and instrument requirements. And when it comes to space technology, it is not always possible to use the newest state-of-the-art detector. Higher level missions require a more developed detector with high TRL to minimize the risk of failure. Essentially, new improved state-of-the-art detector technology must increase their TRL to become relevant for future high level missions for high-energy astronomy.

Since the beginning of X- and gamma-ray observatories in space, there have been numerous technological advances. Detector technology itself has improved drastically in this time. However, observatories in low-to-medium-energy gamma-ray astronomy (0.1-100 MeV) suffer from poor sensitivity, leaving this part of the electromagnetic spectrum as the least explored [3]. Several larger scale missions have been proposed, often combining the Compton and pair telescope into one, as for example the AMEGO [50, 51] and ASTROGAM [52] instrument concepts. And a combination of these might definitely prove powerful, but a large effective area is required together with an effective background suppression. Future observatories should ideally be sensitive both to continuum spectral studies, polarization, and nuclear line studies. Many astrophysical phenomena emit radiation within this energy range, as illustrated in Figure 3.7, which was constructed by the AMEGO team.

Many interesting advances in technology might be an important factor for future observatories within X- and gamma-ray astronomy. Formation flights and adaptive optics could be an essential technology for future focusing telescopes. And with the introduction of multi-messenger astronomy, especially with the future launch of the "Laser Interferometer Space Antenna" (LISA), gravitational waves will become an even more important and powerful probe. Especially, when considering transient phenomena, a combination of light and gravitational waves is important. Many efforts are made in increasing the probability of observing the light from transient events, using CubeSat instruments such as Glowbug [53], BurstCube [54], and MoonBEAM [55].

Common for all the instrument types and mission concepts are that detectors play an important and substantial role in the instrument design. It is imperative, especially contemplating future missions within X- and gamma-ray astronomy, that excellent detectors are used. The 3D CZT drift strip detector developed at DTU Space could serve as a viable candidate for inclusion in any of these instrument types, whether it is as a calorimeter in a pair telescope, integrated into a Compton camera configuration, used as a planar detector for coded mask imaging, or incorporated into focusing optics telescopes.

Despite possessing many of the desired qualities for future high-energy astronomy detectors, such as room temperature operation, photon-by-photon detection, event characterization, sub-

millimeter position resolution, and excellent energy resolution, technology advancements are required for the detector to be used for future observatories. The next chapter will provide an overview of the 3D CZT drift strip detector technology, before summarizing the findings of this PhD project.
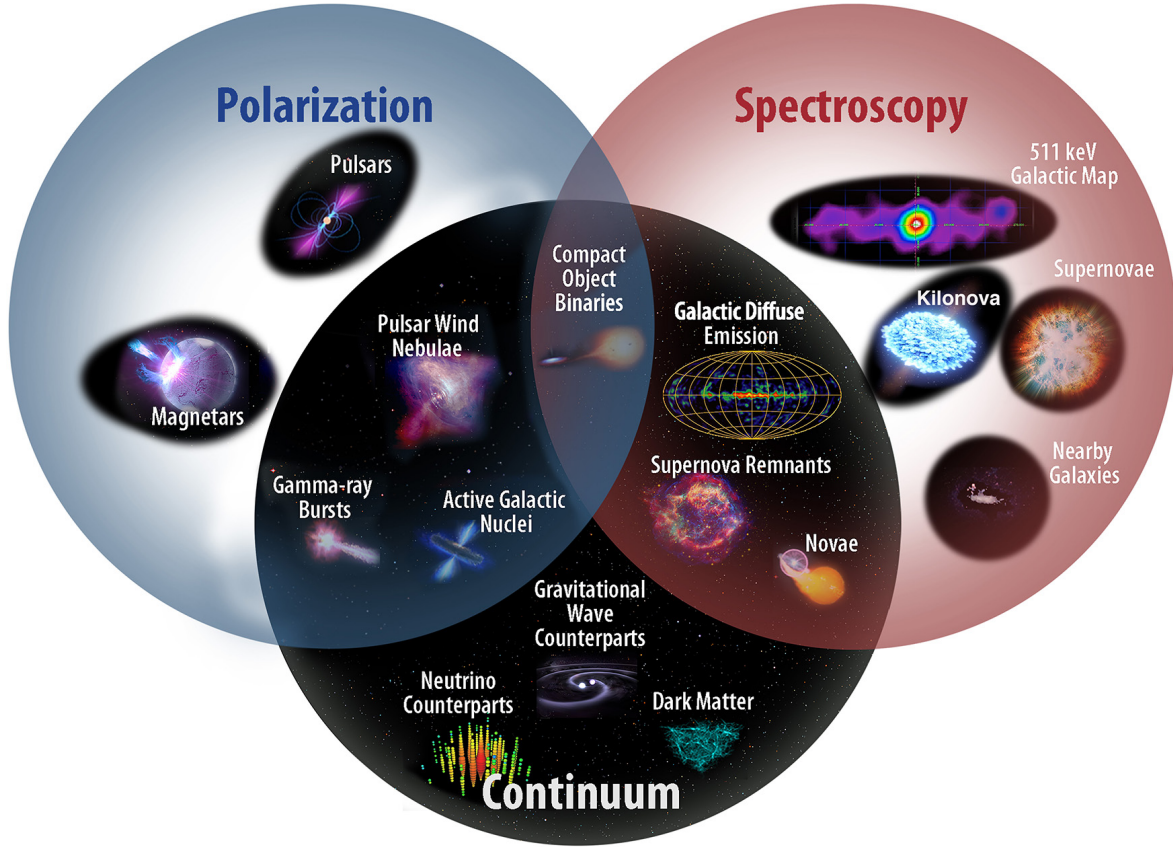

Figure 3.7: Examples of different astronomical phenomena that can be observed when employing observations within polarization, spectroscopy, and continuum. Image credit: *NASA, the AMEGO team* [50].

4   The 3D CZT Drift Strip Detector

DTU Space, formerly known as the Danish Space Research Institute (DSRI), has played a significant role in the development of space instrumentation since the beginning of the space age in the 1960s. DSRI was established in 1968 with the core mission of ensuring a scientific return on Denmark's European Space Agency (ESA) membership through instrument development. In 2007, DSRI was included in a merger, resulting in DTU Space - the space institute at the Technical University of Denmark. DTU Space developed technology is included in many missions, such as ESA missions like INTEGRAL and ASIM, NASA missions like Juno and NuSTAR, and the ESA/NASA James Webb Space Telescope. DTU Space is also involved in technology development for future missions such as Athena [56] and LISA [57].

DTU Space showcases key competences in high-energy instrumentation for X- and gamma-ray radiation, including both focusing optics and detector development. The detector group at DTU Space has provided novel detector development throughout this time period, contributing to the development of microstrip gas detectors for JEM-X onboard the INTEGRAL mission [32, 33], as well as the design, calibration, and selection of the CZT detectors onboard the ASIM mission.

In the late 1990's, the detector group at DTU Space (formerly DSRI) started a development program focused on enhancing the spectral performance of CZT detectors. This effort led to the creation of a unique electrode geometry and readout technique implemented in the 3D CZT drift strip detector, also referred to as the Drift Strip Method (DSM) [58, 59].

In this chapter, the general concept of the 3D CZT drift strip detector is reviewed, together with an overview of the detector laboratory and measurement setup. An overview of the latest detector modules is provided. Additionally, the detector response and data analysis procedure is described.

4.1   Timeline

In this section, the timeline of the 3D CZT drift strip detector will be presented, highlighting some of the most essential technological advances. This will provide the reader with an overview of the status up until the point of the beginning of this project. The timeline is summarized in Table 4.1.

In 1998, two papers were published [58, 59] presenting a novel electrode geometry for CZT detectors. The geometry was based on the principle of Frisch grids used in gas detectors, reducing the sensitivity of the detector to one of the charge carrier types. This was used to compensate the CZT detector from the poor hole movement in the material, making the detector almost unipolar sensing to the electrons. This is the basis of the 3D CZT drift strip detector technology. At this point in time, CZT material quality was worse than what is feasible today. The DSM was used to map grain boundaries in the material in 3D with a 2D-scan and depth of interaction measurements [60], and it was shown that with a dedicated low noise read-out electronic, it was possible to reach a factor 2 of the Fano-factor energy resolution for pixelated CZT drift strip detectors. In 2014, four prototype detectors of size 2cm $\times$ 2cm $\times$ 0.5cm was fabricated [61], and the detector technology patented in 2015 [62]. A readout setup using high speed digitizers was implemented, and the specific algorithms for position determination was developed and verified [63] displaying a spectral resolution of 1% at 661.6 keV and 0.4 mm intrinsic spatial resolution in 3D at the same energy. Another patent was acquired in 2018 [64], and it was shown that these position algorithms could be extended to include Compton interactions inside the same

detector volume, and that one single detector crystal could be operated as a Compton camera [65]. This is especially favorable for a space application where the source flux is dim.

Table 4.1: Key points in the 3D CZT drift strip detector development timeline. Years in blue indicate developments before this project, while years in green indicate developments during this project.

Year	Description
1997	Concept development of the CZT drift strip detector [58, 59].
2002	Mapping of grain boundaries using the DSM [60].
2005	High-energy resolution demonstration of pixelated drift strip detectors [66].
2014	Manufacturing of 3D CZT drift strip detector prototypes [61].
2015	Patent: *X-Ray and Gamma-Ray Radiation Detector* (Patent No. WO2015078902) [62].
2017	Development of position algorithms for the 3D CZT drift strip detector [63].
2018	Patent: *Semiconductor detector with segmented cathode* (Patent No. WO2018065024) [64].
2018	Operation of the 3D CZT drift strip detector as a Compton camera, and full characterization of the 3D CZT drift strip detector prototype [14, 65].
2019	Commencement of the *3D Molecular Breast Imaging* (MBI) project in collaboration with Kromek Group plc [67].
2021	Development of a detector model with a 3D map of electron mobility and lifetime [4, 19].
2023	Full characterization of 10 3D MBI detector modules [5].
2023	Feasibility study of using the 3D CZT drift strip detector in a Compton camera configuration in space (under review).

4.2 The detector concept

The 3D CZT drift strip detector concept is a specific electrode geometry designed to screen the collecting anodes from the poor movement of the holes in CZT. It is based on a geometrically weighted electrode design, which is chosen such that the weighting field, described in Section 2.3.4, of the anode is insensitive to the movement of the holes. This significantly improves the spectral properties of CZT, when the induced signal is not degraded due to inefficient hole collection. In Figure 4.1, a schematic of the electrode geometry and electrical diagram is shown. On each side of the CZT crystal, electrode strips are deposited. On one side cathodes, and on the other side perpendicular are the anodes and drift strips. The cathodes are illustrated as green, the anodes as red, and drift strips as blue. The initial detectors employing the DSM had a planar electrode as cathode, however, the newer implementations have a segmented cathode design. The biasing configuration is designed to direct the electrons towards the anode. The anodes are at ground potential, and the cathodes are negatively biased. The operating bias of the cathodes depend on the detector, but the standard is between -450 V and -350 V. In between each collecting anode is a drift strip section consisting usually of three drift strip electrodes. High

voltage is applied to each group of drift strips by a voltage divider. The central drift strip in between the anodes are biased at 2/3 of the input drift voltage. The two outer drift strips are biased at 1/3 of the input voltage. The input voltage on the drift strips (before the voltage divider) is set to 1/3 of the cathode bias voltage. Thus, for a system setup with -450 V for the cathodes, the anodes will be at ground potential, and the drift strips will have an input voltage of -150 V. This results in the center drift strips being biased at -100 V and the outer drift strips at -50 V. The electrons will drift towards collection at the anode in the given drift cell where the interaction occurred. The anode is placed at the center of the drift cell, and the drift cell boundaries are at the center drift strip electrode in between the anodes. Thus a drift cell consists of a single anode and four drift strips, two on the right and two on the left of the anode, as illustrated in Figure 4.1.
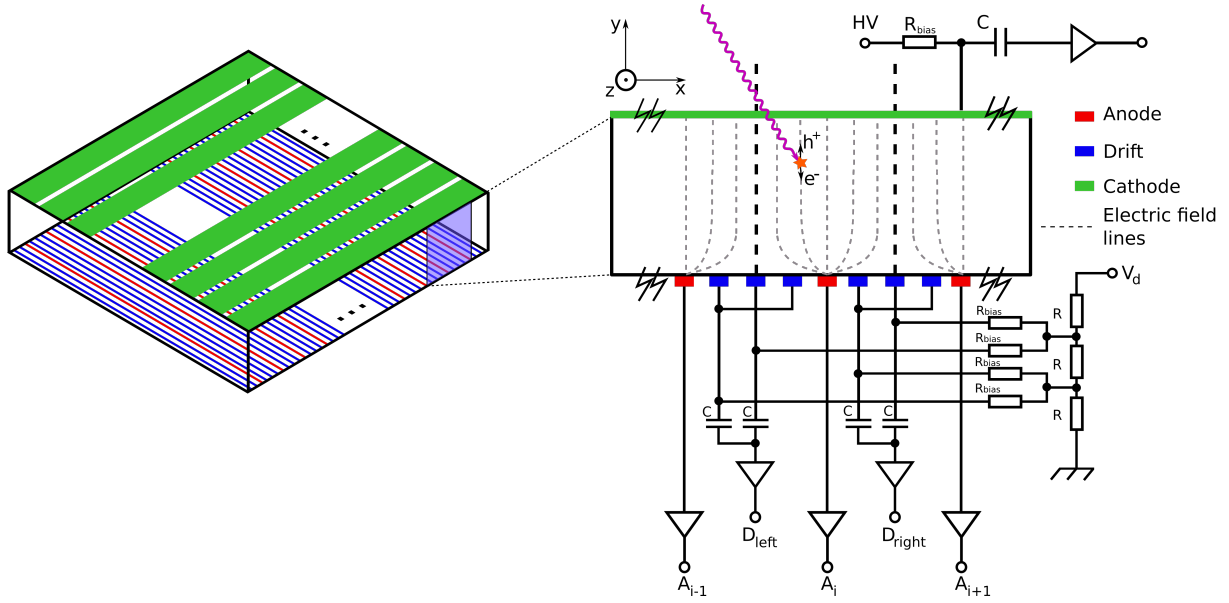

Figure 4.1: Schematic of the 3D CZT drift strip detector electrode geometry, and the electrical diagram of a single drift cell in the detector.

4.2.1 Signal formation

The signal formation occurs in the time between the photon interaction and charge collection at the anode, as described in Section 2.3.2. The photon interaction results in the generation of electron-hole pairs. The charges will start to drift under the influence of the electric field. The electrons drift towards collection at the anode in the center of the drift cell where the interaction took place, and the holes will drift, with poor mobility, towards the cathode. The induced signal is dependent on the weighting potential as described in Section 2.3.4. All electrodes sense the charge movement from start to end of their drift path. In this section the signal formation, and specific detector response will be summarized.

The weighting potential distributions for the anode, right drift strip, and cathode are illustrated in Figure 4.2. The induced signal on the electrodes are as follows:

1. **Anodes:** The weighting potential of an anode is shown in Figure 4.2(left). The small size of the anode strip ensures that its weighting potential is compact around the electrode, as a consequence of the small pixel effect. Therefore, a signal in the anode will have a slow rise until shortly before charge collection, where the signal will increase rapidly. The anodes will not experience a considerable contribution from the holes.

2. **Cathodes:** The weighting potential of a cathode is shown in Figure 4.2(center). The

cathodes have a more linear distribution of their weighting potential, and cathodes close to the interaction will sense the charge movement as soon as it begins. The induced signal will increase until charge collection.

3. **Drift strips:** The weighting potential of a drift strip section is shown in Figure 4.2(right). The drift strips are biased negatively, and therefore directs the electric field lines towards the anode. Their weighting potential distribution is not as compact as for the anodes, therefore, they sense the electron charge cloud movement before the anode, as it moves closer and then away from the drift strip towards collection at the anode.

Understanding the weighting potential distribution in the 3D CZT drift strip detector allows for a better understanding of the generated pulse shapes. In the next section, some common types of generated pulse shapes will be presented, followed by an explanation of the interactions that can cause the specific responses.
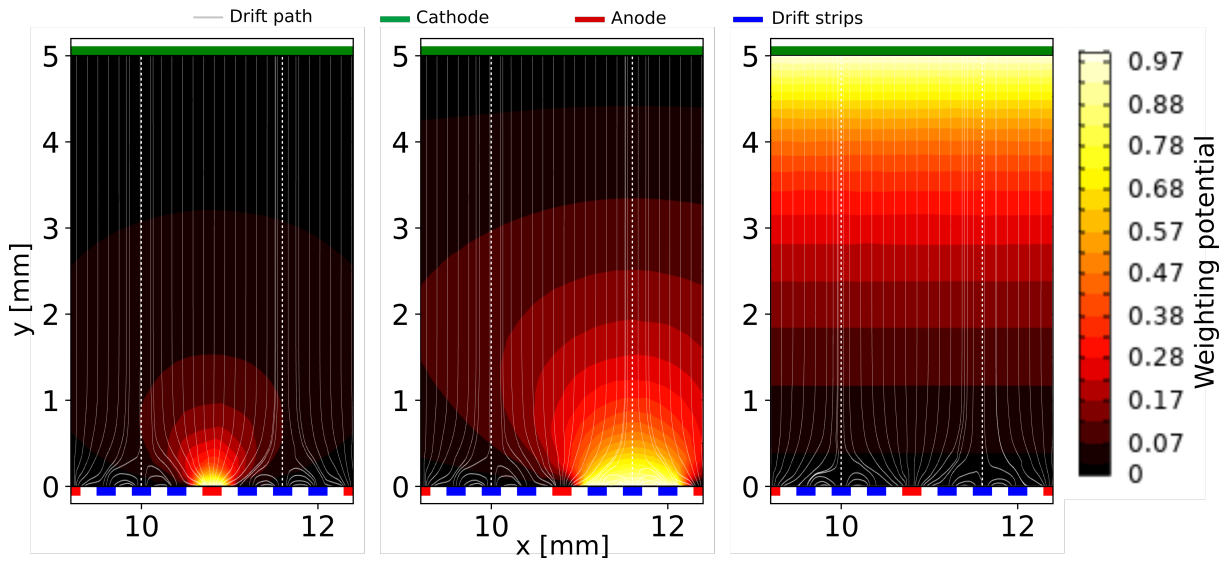

Figure 4.2: Calculated weighting potential distribution in the detector for the (left) anode, (center) right drift strips, and (right) cathodes. The weighting potentials were calculated using the COMSOL Multiphysics ® software [68].

4.2.2 Event types

If the 3D CZT drift strip detector signal is sampled with a high rate, the entire pulse shape is measured. Analyzing the pulse shape can reveal what kind of interaction took place. In this section the most common event types will be described. In this project no source with energy higher than 1.02 MeV was used, therefore, no pair production events will be included.

The single site event is the case where the photon interacts with the detector material once, resulting in a single electron charge cloud to be detected. Examples of interactions leading to this event type are

(a) The photon interacts by photoelectric absorption, depositing its entire energy in the detector.

(b) The photon interacts in a single Compton scattering interaction followed by the scattered photon escaping the detector.

Illustrations of the two interaction examples are given in Figure 4.3. The generated signal in the detector is also illustrated. The collecting anode will display a sharp rise in the pulse shape, as the electron charge cloud approaches collection. The nearest cathodes to the interaction display

a linear rise until collection. The drift strip signal display a rise as the electron charge cloud
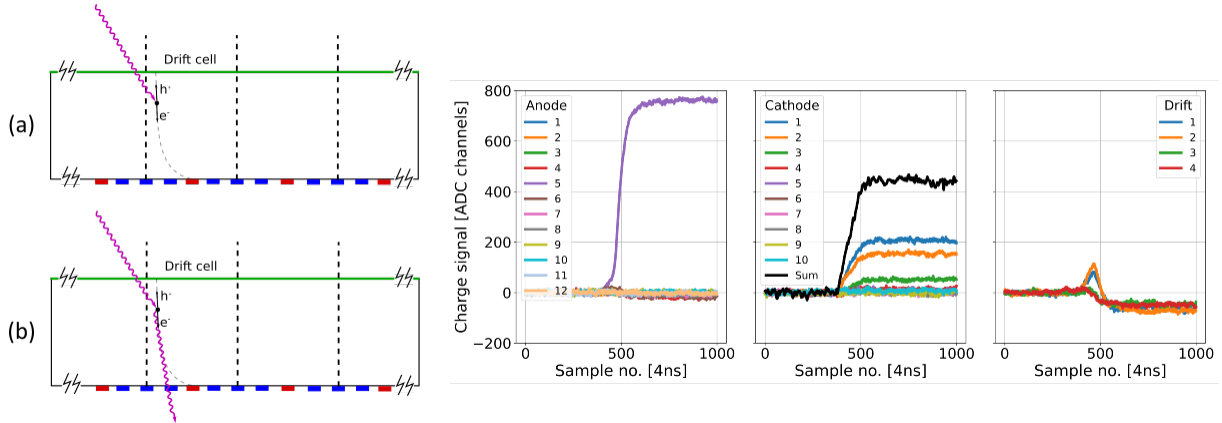approaches, followed by a decrease as the electron charge cloud is collected at the anode.

Figure 4.3: Illustration of photon interactions that can result in a single site event (left), and an example
of a resulting detector response (right).

The single cell multiple event interaction type is when several interactions occur in the
detector material, all within the same drift cell. Because all interactions takes place within the
same drift cell, they are all collected by the same anode. Examples of interactions leading to
this event type are

(a) One or more Compton scattering interactions followed by a photoelectric absorption in
the same drift cell.

(b) One or more Compton scattering interactions in the same drift cell followed by a photon
escape.

Figure 4.4 illustrates the interaction type, together with an example of the detector response. In
this interaction type, the electron charge clouds will drift towards collection at the same anode.
The fact that they approach the anode at different distances, will result in the anode sensing
the electron charge clouds with an offset. Therefore, the signal of the anode will show a specific
staircase shape, one for each of the electron charge clouds. The cathode will display a decrease
in its slope of the signal after collection of the first interactions. Similarly, the drift strips will
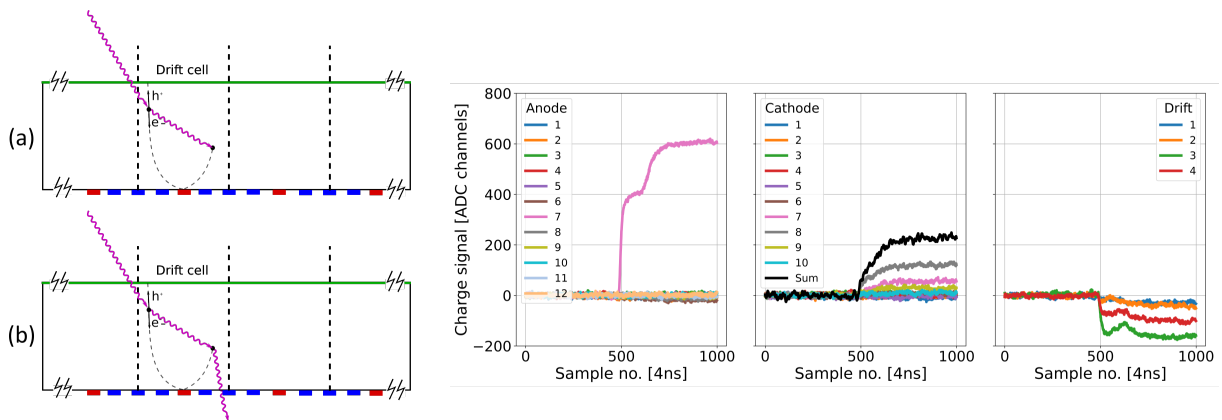sense the movement of two or more electron charge clouds, resulting in a convoluted signal.

Figure 4.4: Illustration of photon interactions that can result in a single cell multiple event (left), and
an example of a resulting detector response (right).

The multiple cell event interaction is similar to the single cell multiple event. In this case however, the interactions occur in different drift cells. Therefore the signal is collected by several anodes, instead of just one. Examples of interactions leading to this event type are

(a) One or more Compton scattering interactions followed by a photoelectric absorption in multiple drift cells.

(b) One or more Compton scattering interactions in multiple drift cells followed by a photon escape.

Figure 4.5 illustrates this interaction type, together with an example of the detector response. The anode signal will in this case be similar to that of the single site event, since two or more anodes just collect a single electron charge cloud. The cathode signal however will be similar to that of the single cell multiple event. The drift signal signature depends on whether the drift cells share readout. If they share a readout, the signal will be convoluted as for the case of the single cell multiple event. If they do not share a readout, it will be similar to that of the single cell event.
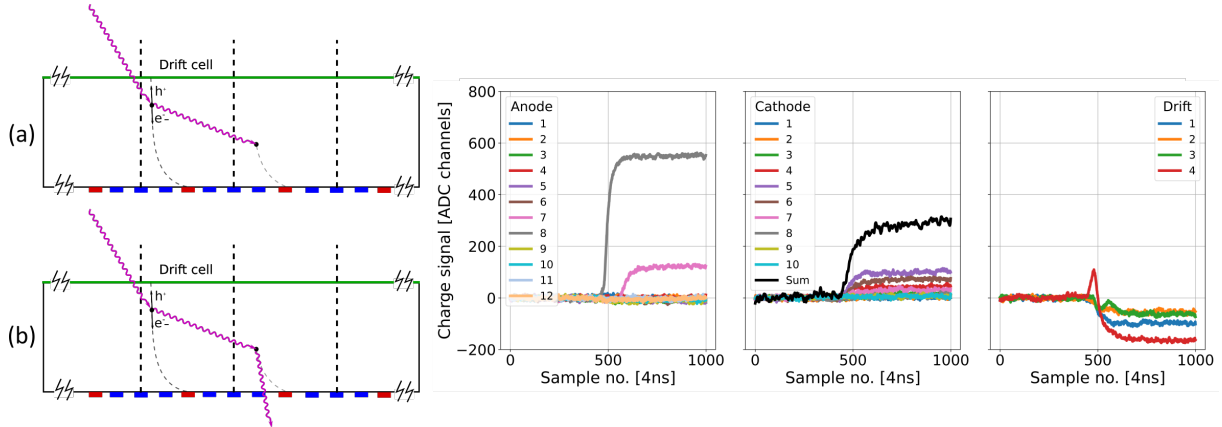
Figure 4.5: Illustration of photon interactions that can result in a multiple cell event (left), and an example of a resulting detector response (right).

The cosmic ray interaction is clearly distinguishable from other events originating from an X- or gamma-ray source in the laboratory. An example of the detector response to such an interaction is given in Figure 4.6. In this event type, the detector pulse heights are very high, and many electrodes are activated simultaneously.
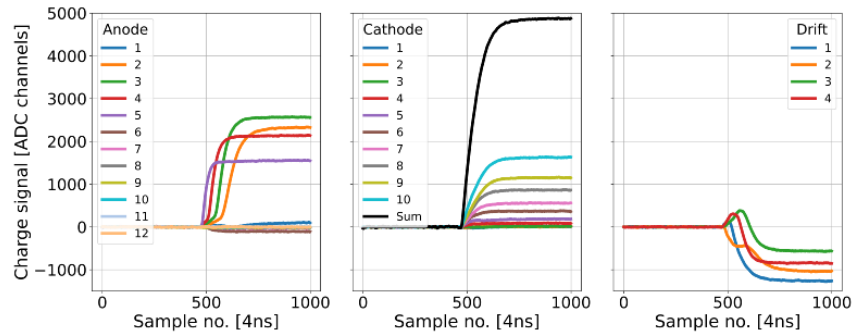
Figure 4.6: Example of the detector response to a cosmic ray event in the 3D CZT drift strip detector.

4.3   Laboratory setup

The detector laboratory at DTU Space has evolved during the course of this project, adapting to the advancements in 3D CZT drift strip detector technology. However, some general laboratory setup equipment persisted. In Figure 4.7 a box diagram of the 3D CZT drift strip detector laboratory setup is shown, and some of the common laboratory equipment which is generally used in all current 3D CZT drift strip detector setup is summarized as follows.

A radioactive source is used for the experimental measurements in the laboratory, a selection of radioactive sources are used. In Table 4.2 the sources used in this project are summarized. The sources are either used with or without collimation, depending on the experimental requirements.

Table 4.2: Radioactive sources used in the project.

Source	Energy [keV]
^{241}Am	59.6
^{57}Co	122, 136
^{137}Cs	661.6

A collimator is placed after the source, if this is used for the given experimental setup. Full illumination (or flood illumination) measurements are, as the name suggest, measurements of an uncollimated radiation source, where the entire detector surface is illuminated. This measurement type is used when spectral properties of the detector are assessed, and for gain/energy calibration measurements. A slit-beam collimation is used to shape the beam into a thin line on the detector, used when assessing the detectors intrinsic spatial resolution.

A high voltage power supply is connected to the detector to supply high voltage (HV) for cathode and drift electrodes. A change in the HV is for example used when assessing the $\mu\tau$-product of the detector material. For normal operational purposes the cathode bias is in the range $V_c = -350$ V to -450 V and the drift bias $V_d = -120$ V to -150 V.

The external electronic circuit consists of Nuclear Instrumentation Module (NIM) standard Charge Sensitive Preamplifiers (CSPs) for each readout channel, resulting in a voltage pulse
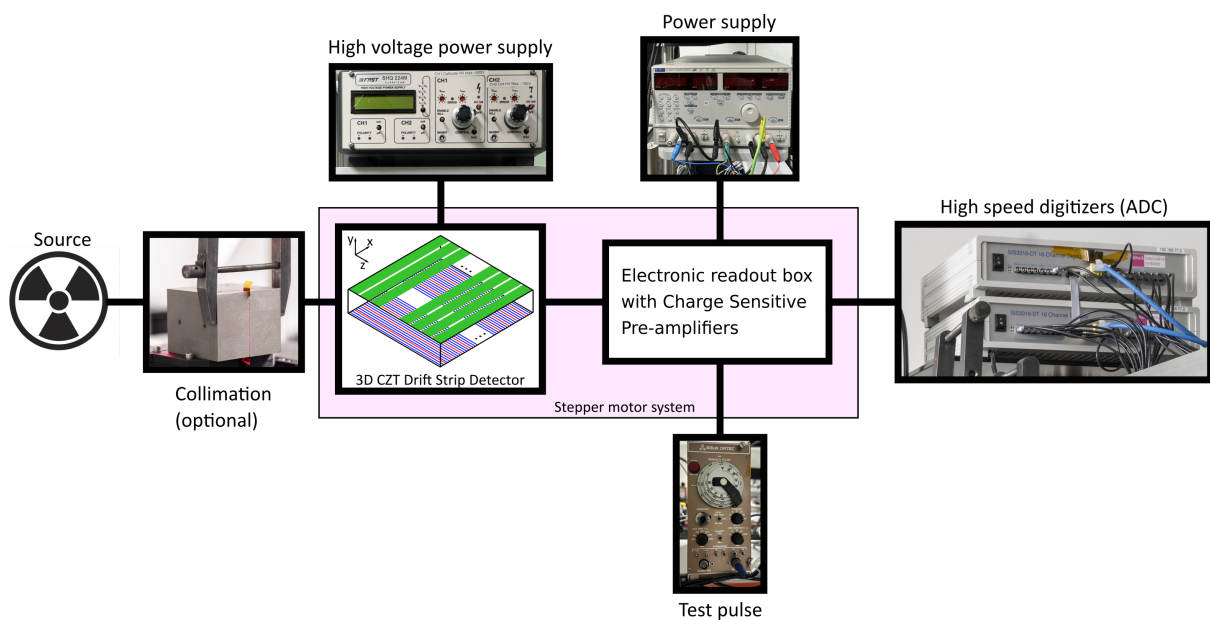

Figure 4.7: Box diagram of the 3D CZT drift strip detector setup in the DTU Space detector laboratory.

signal. A power supply is connected to the electronic readout of the detector.

A test pulse can be connected to the electronic readout box for characterization of the electronic system. This is used to evaluate the performance of the electronics.

A stepper motor system is the base of the entire setup. The detector and the electronic readout box is mounted on the three-axis stepper motor system. This allows for movement of the detector in between measurements. During this project, three different stepper motor systems were used. The second system was a Thorlabs stepper motor system, however, the weight of the detector and electronic readout showed to be too heavy for the motors. Instead a larger Velmex stepper motor system was implemented and connected to the LabVIEW readout routines.

High speed digitizers includes Analog to Digital Converters (ADC), which sample and convert the signal with a high speed. The high speed digitizers are SIS3316 (developed by the company Struck Innovative Systeme), 14-bit, high speed digitizers. They consist of 16 input channels each connected to ADCs. They sample the signal with a rate of 4ns, such that the entire pulse shape generated by the charge movement is sampled.

A computer is connected to the high speed digitizers, high voltage power supply, and stepper motors, such that it all can be controlled using a LabVIEW interface. Here, input for HV, trigger threshold, measurement time, sample length, trigger delay, can be specified, together with specifications for the stepper motors for slit beam measurements.

4.4   Detector versions

Since the 3D CZT drift strip detector concept development in 1997 and until today, various iterations of the detector technology has been fabricated. The three latest versions of the detector are connected to this project and will be presented in this section.

The three 3D CZT drift strip detector versions span from the prototype fabricated in 2014 [61] until today with the detector modules developed during the 3D MBI project [67]. Common for the prototypes are that they are based on the unique electrode geometry and bias structure, that makes them the 3D CZT drift strip detector described in Section 4.2. The three versions of the detector are depicted in Figure 4.8 and summarized in Table 4.3. In the following sections the three detector versions will be summarized.
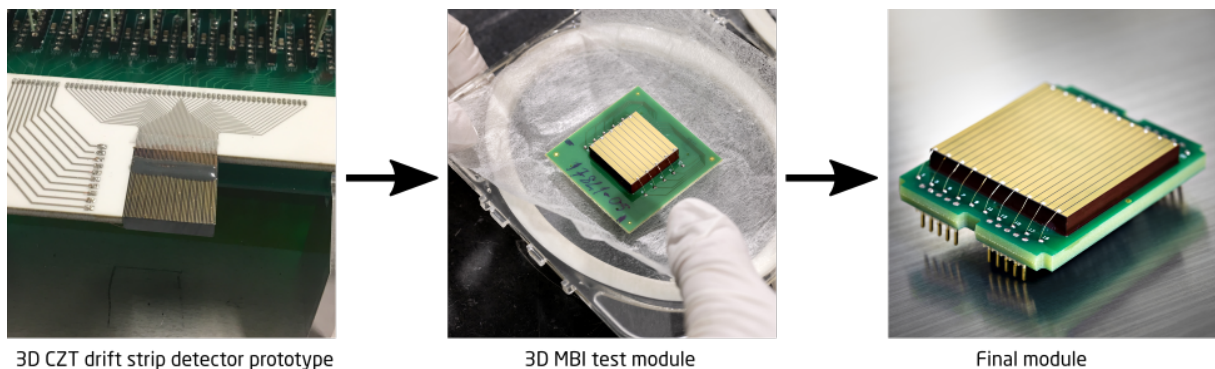

3D CZT drift strip detector prototype   3D MBI test module   Final module

Figure 4.8: The three versions of the 3D CZT drift strip detector covered in this thesis.

**Table 4.3:** Overview of the three versions of the 3D CZT drift strip detector covered in this thesis.

Version overview			
Version	Protoype	3D MBI test module	Final module
Size	$20\times5\times20$ mm^3	$20\times5\times20$ mm^3	$40\times5\times40$ mm^3
Amount	5	10	3
Crystal manufacturer	Redlen	Kromek	Kromek
Electrode deposition	Ohmic contact and oxide layer	Ohmic contact	Ohmic contact

4.4.1 Prototype
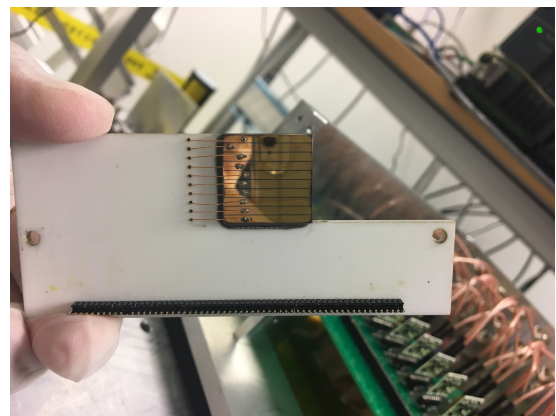
The 3D CZT drift strip detector prototype, manufactured in 2014 [61], is of size $20\times5\times20$ mm^3. The crystal was manufactured by Redlen, and electrode deposition was done at IMEM-CNR. The anode strips and cathode strips were deposited by ohmic contact. For the drift strips, a thin Al$_2$O$_3$ isolation layer were deposited with a uniform thickness, before drift strip metallization was aligned to the anodes. The detectors were bonded to a 3 mm thick alumina-PCB (printed circuit board) providing the electrical connection between electrodes of the detector and the electronic readout system. Photographs of a detector prototype sample are shown in Figure 4.9. The left image is the detector mounted at the electronic readout system seen from the anode and drift side. The right image shows the cathode side of the detector and wire-bonding to the PCB.

The detector electrode configuration consists of 12 anodes with three drift strips in between each anode (two drift strips at the edges). The electrode width is 0.15 mm with a gap of 0.25 mm in between neighboring electrodes. On the other side of the detector, 10 cathodes are deposited with a width of 1.9 mm and a gap of 0.1 mm in between each.

The first characterization study of this detector only included the first four drift cells, and showed a sub-millimeter position resolution of 0.4 mm in all three dimensions. It also displayed an energy resolution of $\sim 1\%$ at 661.6 keV [63]. Later on, the entire detector bulk was characterized and showed a position resolution of < 0.5 mm in all three dimensions, and an energy resolution of $< 1.6\%$ at 661.6 keV [14, 65]. Furthermore, this module was operated as a single-detector Compton camera. By illuminating the detector with a monochromatic source, and extracting energy and position information of two-site interactions in the detector, it was possible to reconstruct an
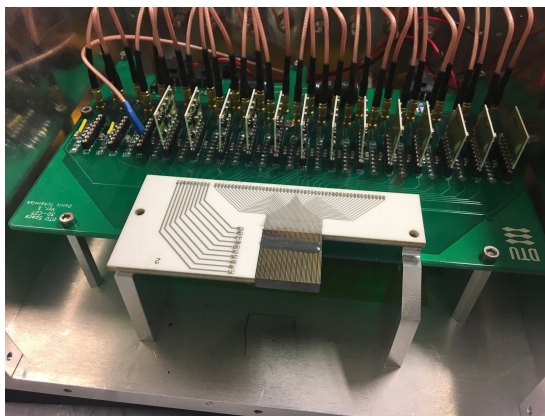
(a) Anode/drift strip side

(b) Cathode side

Figure 4.9: A 3D CZT drift strip detector prototype module (a) anode side and (b) cathode side.

image of the true source location [65]. The setup suffered from electronic noise being a significant contributor to the energy resolution of the detector. This detector version is associated with the first publication in this project [4], where the electron mobility lifetime of the detector was mapped in 3D. This study is presented in Chapter 5.

4.4.2 3D MBI test modules

The 3D MBI test modules were designed and manufactured in close collaboration between DTU Space and Kromek. This was a part of the MBI project funded by the Eurostars Horizon 2020 programme [67]. The goal of this project was to advance the 3D CZT drift strip detector technology for use in a disruptive MBI device for breast cancer diagnosis. And by that, investigate the compatibility between the 3D CZT drift strip detector technology and a new low-dose stationary tomographic MBI concept [69]. The collaboration resulted in 10 3D MBI test modules of size $20\times5\times20$ mm^3.

One of the important design considerations of the 3D MBI test modules was to lower the cost and difficulty of production. Therefore, the oxide layer between the CZT material and the drift strips, that was introduced in the prototype detector, was discarded. Instead all anodes and drift strips were deposited at once using an ohmic contact process. The anode and drift strip width and gap in between is 0.2 mm. The cathode width is 1.8 mm with a gap of 0.2 mm in between each.

The development of the new 3D MBI test modules required an agile setup. Simple substitution between detector modules in the laboratory setup was preferred. Furthermore, changes in the electronic readout PCBs should be possible without drastic impact on the mounted CZT detector crystal. To accommodate this, a stack of PCBs were designed. Figure 4.10 illustrates the 3D MBI test module and the corresponding PCB stack, together with naming of each PCB. The detector module itself was mounted on a single PCB, named "the CZT attachment board". The cathodes are connected by wire-bonding, and drift and anode electrodes by bump-bonding. The board is then plugged in to a PCB stack of three: The anode biasing board, the cathode biasing board, and the digitizer interface board. The *anode biasing board* configures the drift cells into four readout sections, grounds the anodes, and provides the drift strip electrodes with high voltage bias. The *cathode biasing board* configures the cathode readout and provides high voltage bias for the cathodes. Lastly, the *digitizer interface board* where the entire PCB stack connects into the high speed digitizer readout system [5]. With this, the 3D MBI modules had a reduced production complexity compared to the prototype detector, due to the exclusion of the oxide layer in the electrode deposition process. Furthermore, substitution of detector modules
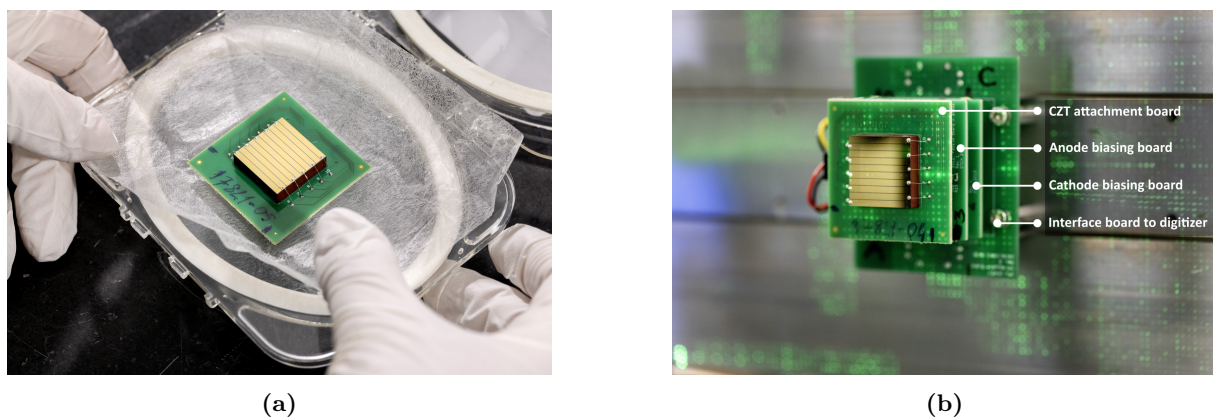

(a)	(b)

Figure 4.10: 3D MBI test modules (a) in container and (b) mounted on PCB stack for measurement.

was a simpler procedure.

A comprehensive characterization study of all the detector modules was carried out during this project [5], and is presented in Chapter 5.

4.4.3   3D MBI final modules

The 3D MBI project [67] resulted in the production of three final modules. These modules have the same electrode design as that of the 3D MBI test modules. The modules are of size 40×5×40 mm^3. An image of the final module is provided in Figure 4.11.

The final laboratory setup for the module is still under development, and therefore the characterization work is still ongoing. It is expected that the detector will have similar electrical characteristics as the 3D MBI test modules, and similar spatial and spectral resolution. The electronic readout system is different than that of the 3D MBI test modules, which may affect electronic noise in the system, hopefully to the better. Especially the CZT material quality will be interesting to assess, since the crystals are larger. It may be expected that grain boundaries will be more common for these detector. Although the characterization work of the modules is still ongoing, the dimension of the detector was used for the final paper simulation study done in this project, which is presented in Chapter 5.
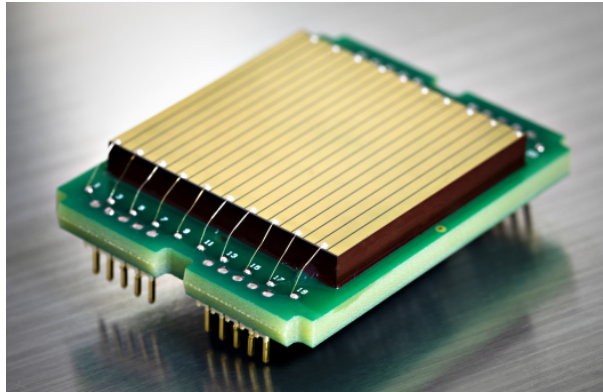

Figure 4.11: The final module manufactured during the 3D MBI project [67]. Crystal size is 40×5×40 mm^3. Anodes and drift strips are connected to the PCB by bump-bonding, and the cathodes are connected by wire-bonding.

4.5   Data analysis

The source code for the entire data analysis pipeline for the 3D CZT drift strip detector was developed in Python. It comprises scripts for the overall data analysis flow for the 3D CZT drift strip detector, from raw data outputted by the high speed digitizer system to the final data visualization. The most common data processing algorithms and procedures used when working with data from the 3D CZT drift strip detector will be described in this section.

4.5.1   Reading raw data

The high speed digitizers measure the generated pulse shapes in each channel of the detector for every triggered event. The sampled data is read with a Python script that stores data in a multidimensional array structure. For the case of the prototype and 3D MBI test modules, 26 readout channels are connected to the detector. Thus, for a measurement of N interactions, the data set, `rawData`, then consists of $N \times 26$ pulse shapes for a given measurement. And, for each interaction there are 26×`sampleLength` data points, where `sampleLength` is the number of samples in each pulse. The default value is 1000 samples. For the current state of the detector, focused mainly on detector performance possibilities and analysis, data size is not a limitation. In Figure 4.12, a plot of the 26 raw data pulse shapes for a photon interaction in the detector

is given. The pulse height of each signal is calculated by a subtraction of the mean value of the samples in the baseline signal from the mean value of the signal after full formation. As each event is read out and stored, the pulse heights for all pulse shapes are calculated simultaneously, and stored in an array of size $N \times 26$ named ADC_PH. When sampling data, it is possible to define the trigger delay, triggerDelay, of a measurement, and therefore this value is also extracted as the data is read. This quantifies at what sample value the trigger occurred. In Table 4.4 these variables are summarized for a brief overview.
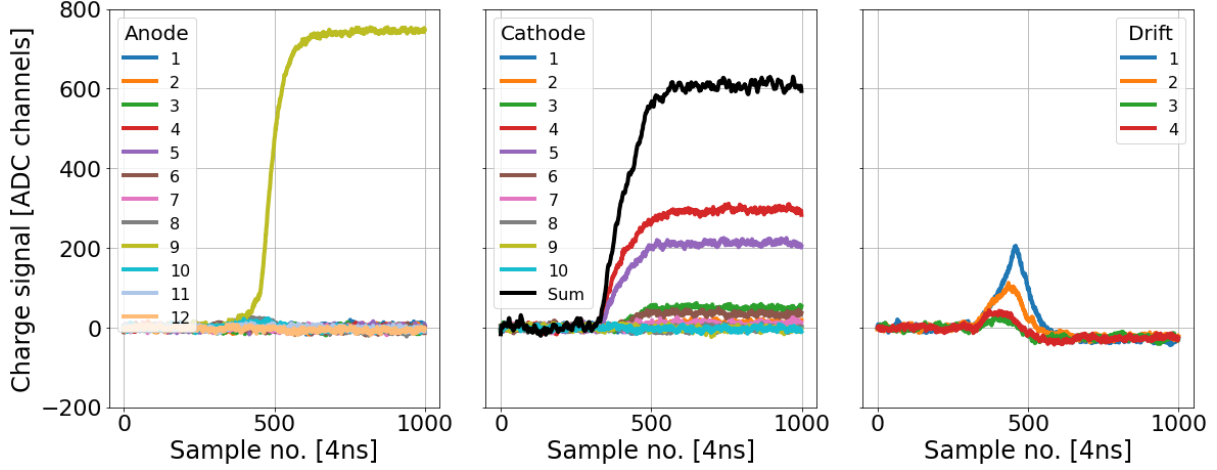
Figure 4.12: 26 raw data pulse shapes for an arbitrary event in the 3D CZT drift strip detector.

Table 4.4: Raw data output from the 3D CZT drift strip detector.

Variable name	Description
rawData	A multidimensional array structure containing $N \times 26$ pulse shapes for the given measurement. For each event, it contains all samples for each of the 26 channels. ($N \times 26 \times$ sampleLength).
ADC_PH	An $N \times 26$ array containing pulse heights for each channel.
sampleLength	Returns the sample length of a given data set. The default sample length is 1000 samples.
triggerDelay	The trigger delay on a data set. Default value is half the sample length.

4.5.2 Gain/energy calibration

It is an absolute necessity to do a gain/energy calibration before calculating the position of interactions in the detector, since the ratio between pulse heights are used to asses interaction positions in the detector.

The gain calibration of the detector system makes sure to calibrate all signal amplitudes and corrects for the difference in gain in the CSPs. It is calibrated at the same time as the ADC signal is converted to units of energy [keV]. Three sources are used when gain/energy calibrating the detector. A linear regression of the known source energy and the measured pulse height in ADC channel, allows us to determine a linear relation between the measured signal in ADC channels, E_{ADC} and the true source energy in keV, E_{keV},

$$E_{\text{keV}} = a \cdot E_{\text{ADC}} + b \tag{4.1}$$

where a is the slope of the relation, and b the intersection with the y-axis.

The method requires determining the ADC channel value of the full induced signal of the electrode in question. Even though the method of calibrating the electrodes are similar for all electrode types, there are some variations. The methods will be described here. An illustration of the data analysis process is given in Figure 4.13.

Anodes: When collecting data for the anode gain/energy calibration, the system is operated in its usual mode, where the signal is triggered by the anodes. A high trigger threshold is set, such that only the upper part of the Compton continuum is included, since photopeak data is used for the calibration. The peak energy is determined by fitting the photopeak with a Gaussian. The relation between the incoming photon energy in keV and the extracted peak energy in ADC channels is then fitted with a linear relation as given in Eq. (4.1).

Cathodes: The same full illumination measurement used for the anodes, can be used for calibrating the cathodes. For the cathodes, the pulse height histogram is not displaying a photopeak, instead it has a plateau-like shape. The half height at the edge of the plateau represents full induced signal on the cathodes. The further process is similar to that of the anodes, fitting a linear regression to the relationship between the true source energy and the ADC channel value for the half height of the edge of the cathode pulse height histogram.

Drift: The procedure for gain/energy calibration of the drift strips is similar to that of the anodes. However, to achieve a photopeak shape for the drift strip pulse height histogram, they must collect the electrons. Therefore, modifications are made to the setup before doing full illumination measurements. First of all, the high voltage of the drift strips is changed to 0 V, such that they collect the electrons. Furthermore, the digitizer settings are modified such that
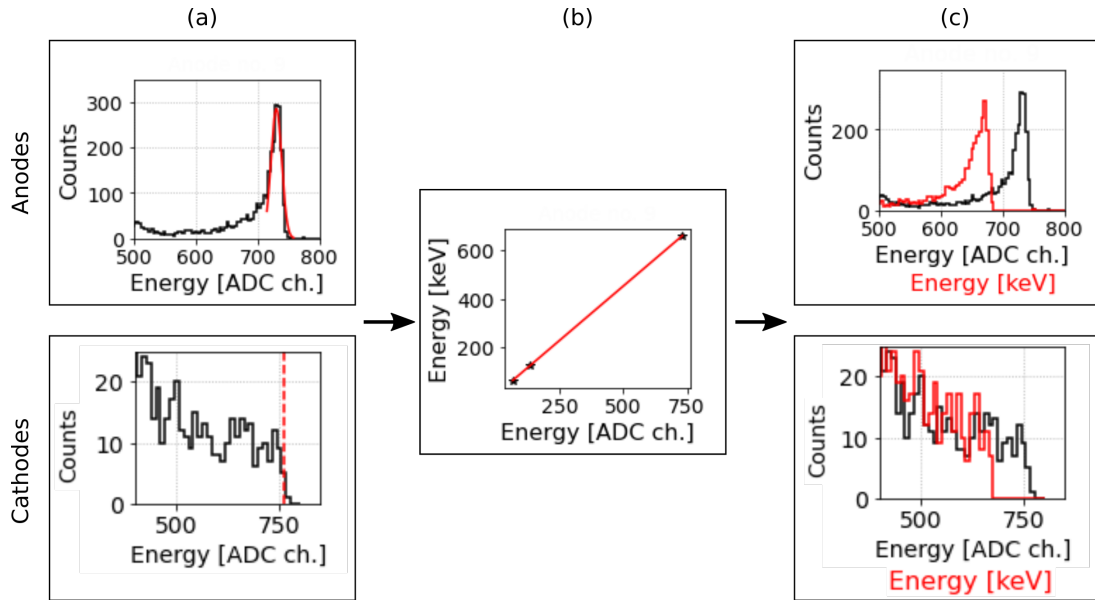
Figure 4.13: Illustration of the gain/energy calibration data analysis process. Full illumination measurements were done using three sources (Table 4.2) (a) The energy in ADC channels is determined for the fully induced signal. This corresponds to the photopeak for the anodes, and the half height of the plateau edge for the cathodes. (b) The linear relation between the energy in keV and the measured energy in ADC channels are then determined. (c) The linear relation can be used to convert the signal from ADC channels to keV.

the system triggers on a rise in the drift strip pulses instead of the anode pulses. The following data analysis is then similar to that of the anodes.

4.5.3 Data sorting algorithm

An algorithm for sorting the data from the 3D CZT drift strip detector consists of a pulse shape and height analysis procedure. It assigns a key to each event, indicating what type the given event is, following the event types described in Section 4.2.2. An overview of the grouping is given in Table 4.5. The sorting algorithm returns an array of $(1 \times N)$ with a key for each event assigning it to a specific event type.

Table 4.5: Overview of keys returned by the sorting algorithm, defining which event types occurred for a given data set.

Key	Event type	Description
0	Single event	One interaction, one triggered anode.
1	Single cell multiple event	Several interactions, one triggered anode.
2	Multiple cell event	Several interactions, several triggered anodes.
3	Cosmic ray	Many triggered electrodes, huge energy deposit.
-1	Undefinable	Does not fit any of the above requirements.

The input to the sorting algorithm is the anode pulse heights and shapes. It loops through every single event to determine the type of event that occurred. The first check is whether the maximum anode pulse height is above a predefined threshold. This indicates that a lot of energy was deposited in the detector, and the event is then considered to be a cosmic ray event. Next it investigates the number of activated anodes. An anode is activated if the pulse height is above a low threshold, this indicates that the anode collected an electron charge cloud. If the number of activated anodes is more than one, it is assigned as a multiple cell multiple event. If only one anode is activated, two possible event types exist. The single event or the single cell multiple event. In this case, pulse shape analysis is necessary to determine the event type. The derivative of the activated anode signal is analyzed in terms of number of peaks. If only one peak occurs, it is a single event. If there is more than one peak, it is a single cell multiple event. An example of charge and current signal of a single cell multiple event is given in Figure in Figure 4.14. In Algorithm 1, the flow of the sorting algorithm is summarized.
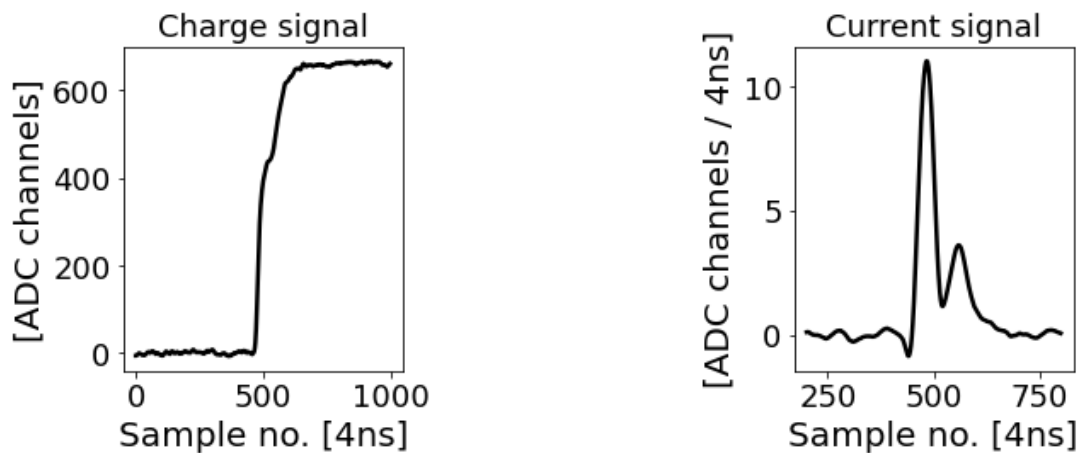

Figure 4.14: The sorting algorithm counts the number of peaks in the current signal for the anode, to determine if it is a single interaction or multiple interaction event. One peak indicates it is a single event, whereas multiple peaks indicate that it is a single cell multiple event.

Algorithm 1 The sorting algorithm

   Input: Anode pulse heights and shapes.
   for n from 1 to N **do**
      Calculate number of activated anodes.
      if maximum anode pulse height $>$ ph$_{max}$ **then**
         `event type = 3`.
      else if number of activated anodes $= 1$ **then**
         Count number of peaks in the current signal.
         if number of peaks > 1 **then**
            `event type = 1`
         else if number of peaks $= 1$ **then**
            `event type = 0`
         end if
      else if number of activated anodes > 1 **then**
         `event type = 2`
      else
         `event type = -1`
      end if
   end for

4.5.4 Position calculation

The 3D CZT drift strip detector has an intrinsic spatial sensitivity in 3D. The achievable intrinsic spatial resolution of the detector in 3D is sub-millimeter and have several times been displayed to be less than 0.5 mm FWHM at 661.6 keV [5, 63, 65].

To achieve the sub-millimeter intrinsic spatial resolution in 3D, specific algorithms are used to calculate the interaction position of a photon. For this, the distinct pulse shapes generated by the 3D CZT drift strip detector are used. The algorithms used have been described in previous works [4, 5, 14, 63, 65], but will briefly be summarized in the following for single interaction events. The algorithms presented here are the most up to date in terms of absolute position. A description of the algorithms used for calculation of position of double site events (Compton scattering) can be found in [14, 65]. The dimensions of the detector are summarized in Figure 4.15 where x-axis is perpendicular to the anodes. The y-axis is between the anode and cathode plane, and the z-axis is perpendicular to the cathodes.
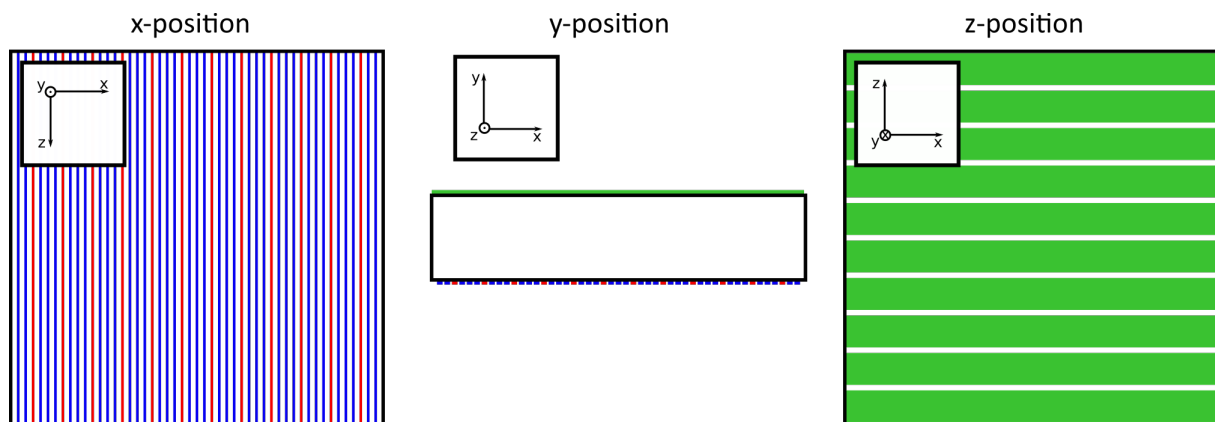

Figure 4.15: Illustration of the x-, y-, and z-dimension of the 3D CZT drift strip detector. The x-axis is defined perpendicular to the anodes. The y-direction is defined along the depth of the detector. The z-direction is defined along perpendicular to the cathodes.

4.5.4.1   x-position

The x-position is calculated utilizing the anode and drift strip signals. More precisely, the activated anode number, x_{trig}, provides a rough estimate of the x-position of an interaction. The amplitude of the inverted current signals of the left and right drift strip, A_{DL} and A_{DR}, are then used to provide a finer positioning. Figure 4.16 illustrates an activated anode pulse shape and the two corresponding inverted current signals used to determine the x-position of the given event. To calculate the x-position the following equation is used [63],

$$x_{\text{pos}} = 0.4 + \left[x_{\text{trig}} + F \cdot \frac{A_{\text{DR}} - A_{\text{DL}}}{A_{\text{DR}} + A_{\text{DL}}} \right] \cdot P_{\text{an}} - \frac{P_{\text{an}}}{2} \tag{4.2}$$

where the constant 0.4mm is the offset between the edge of the detector and the first drift strip, P_{an} is the anode pitch of 1.6 mm, and F is an adjustable scaling factor to calibrate the x-position algorithm for the specific detector.
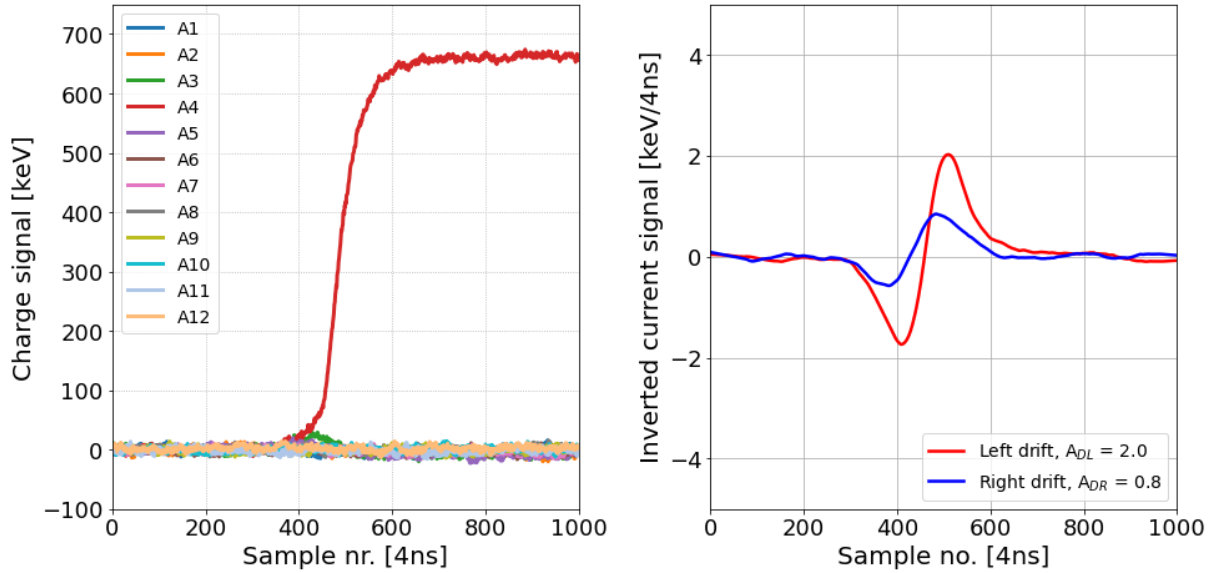
Figure 4.16: Determining the x-position for an interaction in the 3D CZT drift strip detector requires identifying the collecting anode number (left). The finer positioning is then calculated by determining the peak amplitudes of the inverted current signals for the two neighboring drift strips (right).

4.5.4.2   y-position

The y-position calculated using the depth-of-interaction (DOI) method. The relationship between the activated anode pulse height, A_m $(m = 1, 2, ..., M)$, and the sum of each cathode pulse height, C_j $(j = 1, 2, ..., J)$. M is the total number of anodes, and J is the total number of cathodes. An example of the anode pulse shape and cathode summed pulse shapes used for the y-position calculation is given in Figure 4.17.

The equation used to determine the y-position is given by [63]

$$y_{\text{pos}} = \frac{\sum_{j=1}^{J} C_j}{A_m} \cdot d_{\text{CZT}} \tag{4.3}$$

where d_{CZT} is the detector thickness.
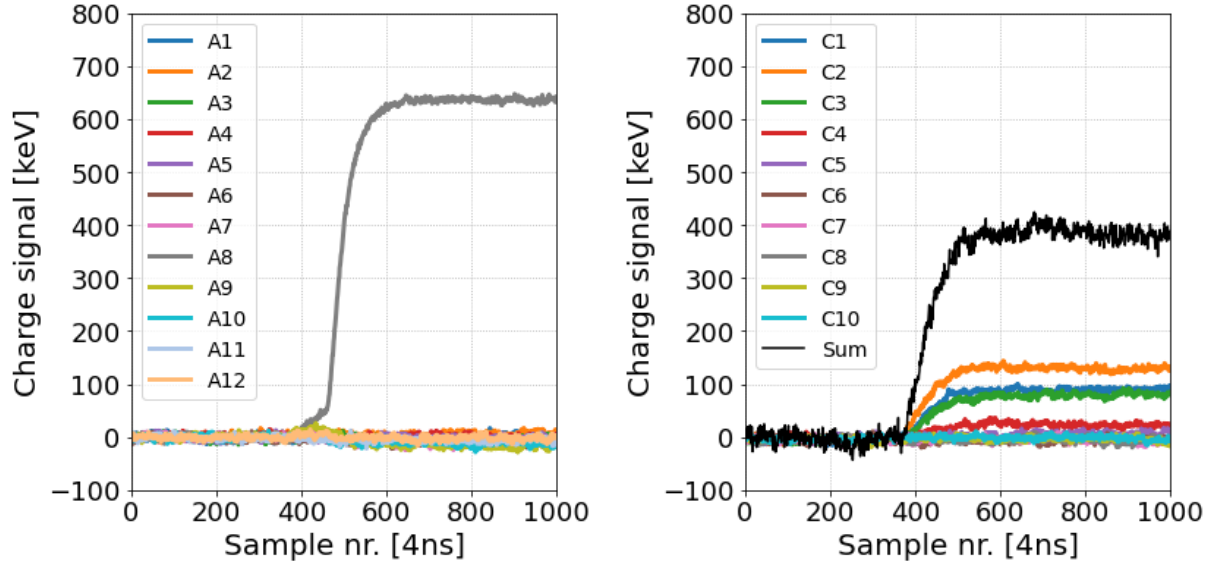
Figure 4.17: An illustration of the anode charge signal, and the summed cathode charge signal. The relation between the two pulse heights provides the y-position of the interaction.

4.5.4.3 z-position

The z-position is calculated by a center of gravity method. All cathode pulse heights are used for the calculation, in the equation [63]

$$z_{\text{pos}} = \frac{\sum_{j=1}^{J} j \cdot C_j}{\sum_{j=1}^{J} C_j} \cdot P_{\text{ca}} - \frac{P_{\text{ca}}}{2} \tag{4.4}$$

where P_{ca} is the cathode pitch. An illustration of the cathode pulse height shapes, and the pulse height distribution along the z-position are given in Figure 4.18.
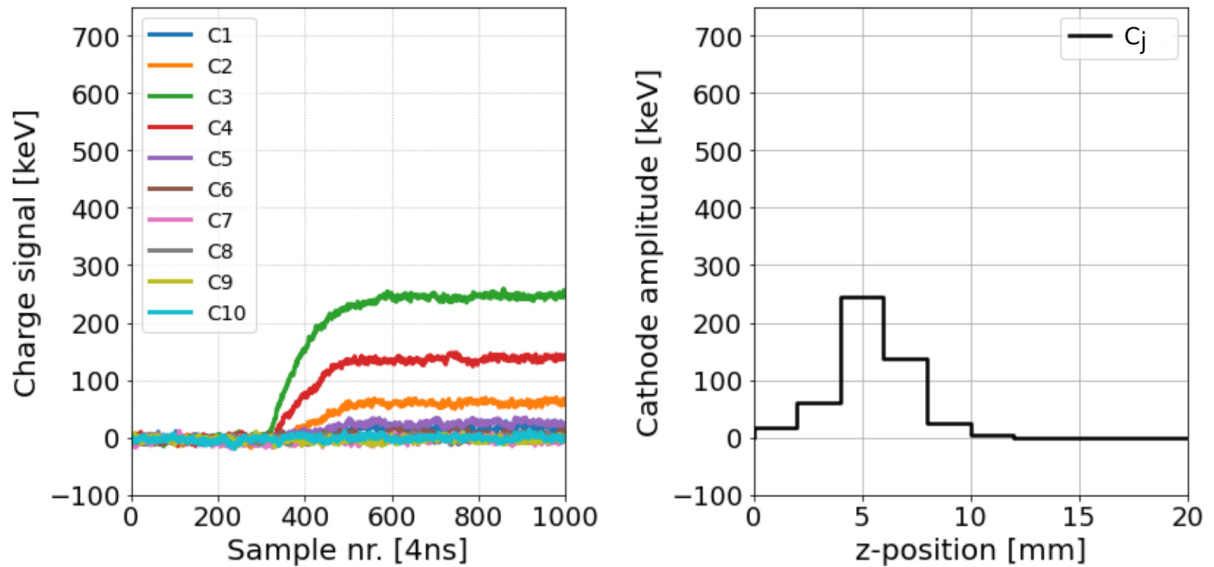
Figure 4.18: Cathode pulse shapes (left) and the resulting pulse heights along the z-direction (right).

This method however falls short close to the cathode side. In this case, the events occur so close to the cathodes that some of the cathode pulse shapes will display a decrease in the charge signal before an increase. This will reduce the position sensitivity to that of the cathode pitch.

The position accuracy can be improved by only considering the induced charge over the last part of the collection, C_j^*. Now pulse heights are calculated from a delayed start time, t_0^*, until the collection time t_1 as follows

$$C_j^* = C_j(t_c) - C(t_s^*) \tag{4.5}$$

where the delayed start time is defined as $t_0^* = t_1 - dt^*$, where dt^* is an adjustable drift time parameter [63]. These new pulse heights can provide a better distribution as shown in Figure 4.19. The reader is referred to [63] for further information on this method.
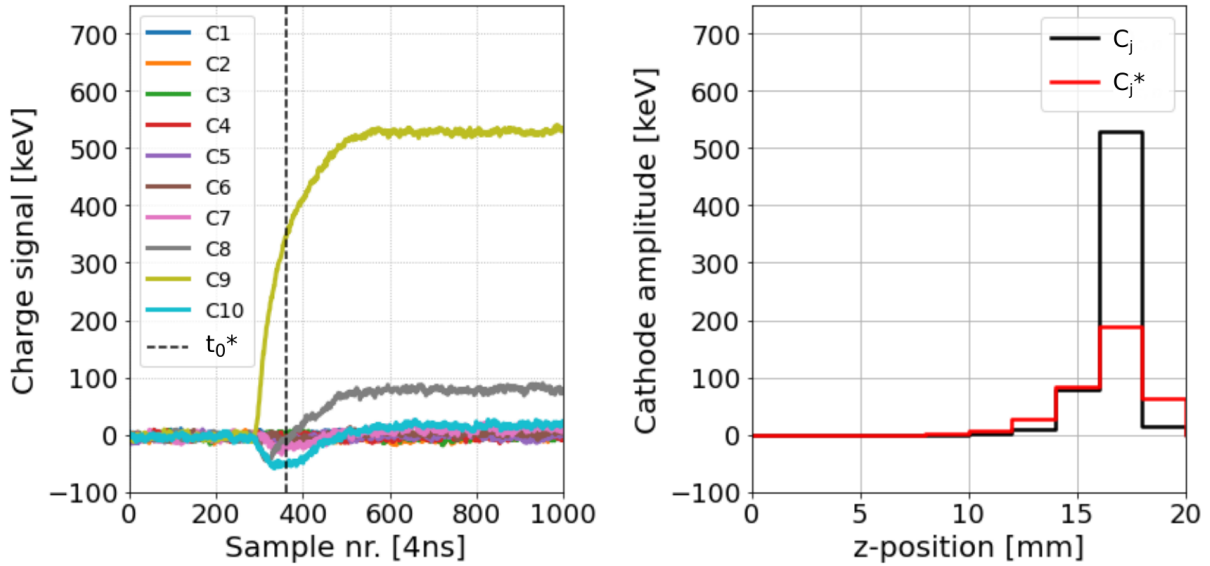

Figure 4.19: Cathode pulse shapes (left) and the resulting pulse heights along the z-direction (right) before and after calculating the pulse heights with a delayed start time.

4.5.5 Energy calculation

The 3D CZT drift strip detector also has a spectral sensitivity. It is able to determine the energy deposited by a photon interaction. The energy resolution has been demonstrated to $\sim 1\%$ at 661.6 keV [63]. Currently the energy resolution displayed by the detector is limited by the electronic noise of the laboratory setup.

The deposited energy in the detector is proportional to the number of generated electron-hole pairs. Therefore, the induced signal on the anode by the electron charge cloud is a reflection of the photon energy. By energy calibration of the detector with known sources, it is possible to convert the induced signal from an ADC signal to keV, as described in Section 4.5.2. The pulse height spectrum of a monochromatic source will result in a photopeak at the incoming radiation energy, as described in Section 2.2.2, with a FWHM corresponding to the spectral resolution of the detector. In Figure 4.20(left), an energy spectrum of a ^{137}Cs source measured by a 3D CZT drift strip detector is shown. The photopeak displays a clear tail towards the left of the peak. This tail represents photon interactions where the generated electron charge cloud have experienced more trapping, or where they do not traverse the entire weighting potential of the anode, thus not inducing a full signal. This tailing effect is in fact very dependent on the photon interaction position in the detector, and the 3D intrinsic spatial sensitivity of the detector can be utilized to correct the spectral information.

The spectral measurements are corrected using a 3D lookup table for the specific detector at hand. The energy correction is done by fitting the energy of a known source measured by an energy calibrated detector. The photopeak position is fitted along slices in the y-direction and pixels in the x/z-directions. With these, a correction factor is calculated and used to correct

measured energy. In Figure 4.20(right) the resulting corrected energy spectrum of a ^{137}Cs source measured by a 3D CZT drift strip detector is shown.

The contributions to insufficient signals are

1. **y-direction:** If the electron charge cloud drifts far before collection it will experience more trapping, reducing the induced signal. If the event occurs close to the anode, it will not traverse the entire weighting potential, resulting in a reduced signal.

2. **x/z-directions:** Along the x-direction, a charge cloud generated close to the drift cell boundary will drift longer than if it was generated directly above the anode. Due to the shape of the electric field lines, it will drift further, and therefore experience more trapping. Along the z-direction, material non-uniformity can contribute to areas with more trapping.

The 3D correction method of the spectral measurement was originally described in [63], and for further information on the method, the reader is referred to this work.
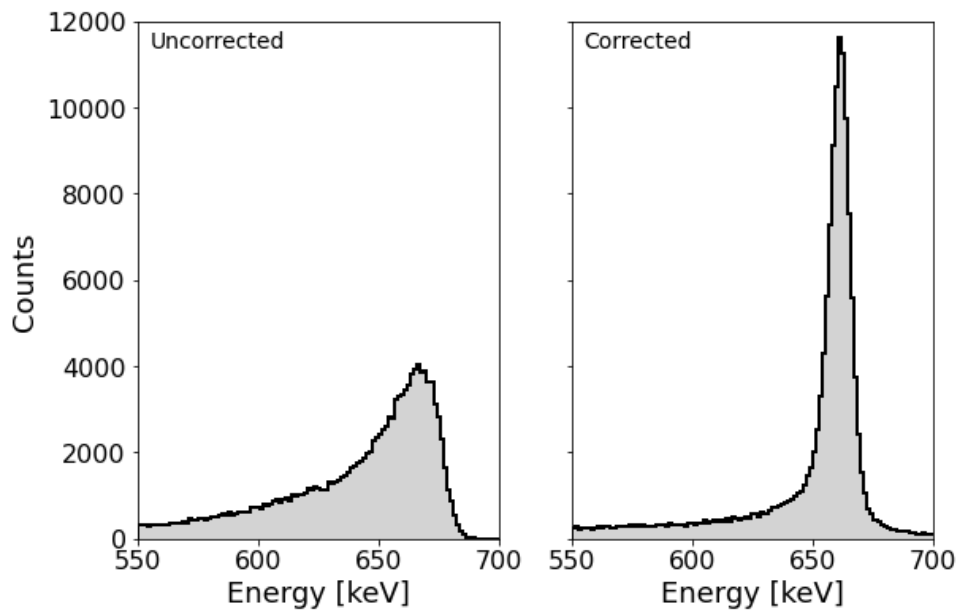
Figure 4.20: Energy spectrum of a ^{137}Cs source measured by a 3D CZT drift strip detector. The left spectrum is before energy correction, and the right spectrum is after the energy correction.

4.5.6   Electron drift time calculation

The electron drift time in the 3D CZT drift strip detector, is the time between the photon interaction and electron charge cloud creation, to the point of which the electron charge cloud is collected at the collecting anode. The electron drift time is affected by the HV bias applied to the detector, the higher the bias, the faster the collection. The electron drift time is determined by pulse shape analysis of the activated anode, and the summed cathode signal. Figure 4.21(left) illustrates the pulse shape of an activated anode. The collection time of the electron charge cloud is denoted t_1. It is the point where the anode pulse shape flattens after the steep rise. This point can be determined by analyzing the derivative of the anode charge signal, as illustrated in 4.21(right). The point at the end of the peak is the collection time of the electron charge cloud. This can then be included in the summed cathode pulse shape signal of the cathodes. A slope is then fitted to the cathode summed signal, and the intersection between the slope and the baseline of the signal denotes the beginning of the charge cloud movement, t_0, as illustrated in Figure 4.22. The electron drift time, in the case of a sample time of 4ns, is then given by

$$t_d = (t_1 - t_0) \cdot 4\text{ns}. \tag{4.6}$$

The sum of the cathode signals can also be used to determine t_1 instead of using the derivative of the anode signal. In this case, the intersection between the slope and the pulse height baseline provides the collection time. However, this can be tricky for events occurring close to the anode, as they induce a minimum signal on the cathodes.
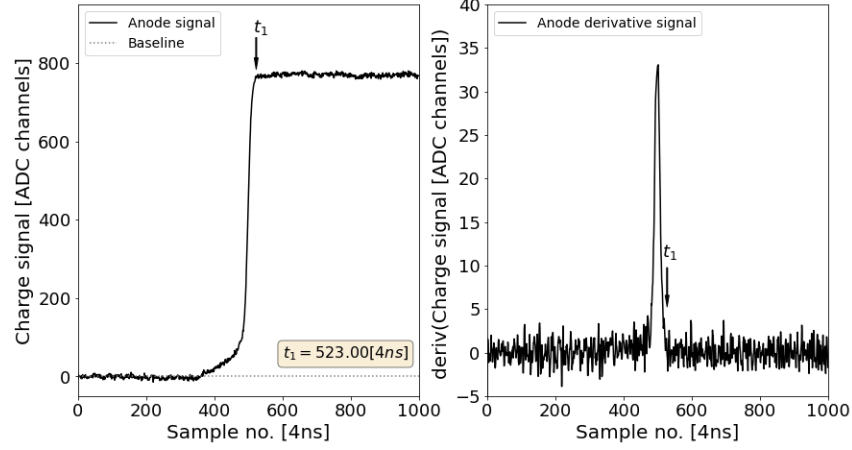
Figure 4.21: Pulse shape analysis of the activated anode charge and current signal to determine the collection time, t_1, of the electron charge cloud.
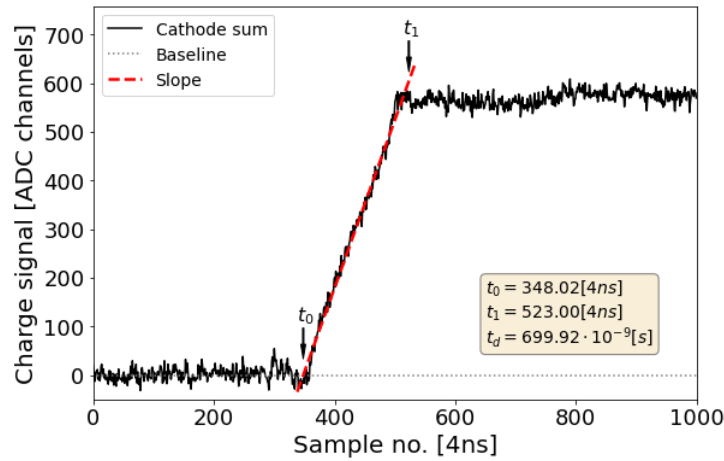
Figure 4.22: Pulse shape analysis of the summed cathode charge signal to determine the start time, t_0, of the electron charge cloud movement. Figure obtained from [4] © IEEE 2021.

5   Summary of Papers

This chapter contains a summary of the three papers this thesis has contributed.

The first paper investigates the possibility of utilizing the spatial sensitive nature of the 3D CZT drift strip detector to investigate the non-uniformity of the detector material in terms of electron mobility and lifetime. Knowledge of the carrier mobility and lifetime in the detector is essential when modelling pulse shape formation, and can be used for data correction.

The second paper is a comprehensive characterization study of the 10 fabricated 3D MBI test modules manufactured during this project. It investigates the performance of the detectors with new manufacturing processes differing from that of the 3D CZT drift strip detector prototype. Furthermore, it evaluates the application of the 3D CZT drift strip detectors in new emerging MBI systems.

The third paper investigates the feasibility of operating 3D CZT drift strip detectors in a small Compton camera in space. Operating the detectors in a small payload, for example on a CubeSat, can increase the TRL of the 3D CZT drift strip detector.

5.1   Paper 1: Carrier Lifetime and Mobility Characterization Using the DTU 3-D CZT Drift Strip Detector

Carrier Lifetime and Mobility Characterization Using the DTU 3-D CZT Drift Strip Detector

S. Howalt Owe, I. Kuvvetli, and C. Budtz-Jørgensen

This paper was the first to be published during this thesis work. It focuses on producing a reliable 3D map of the detector material properties with the purpose of being used as a look-up table by a detector model. The initial results were presented in an oral presentation at the IEEE NSS MIC RTSD 2020 conference. Following the conference, the findings were submitted in IEEE Transactions on Nuclear Science in November 2020, and after a minor revision accepted in March 2021 [4]. The paper is attached in Appendix A, or can be found using the link https://doi.org/10.1109/TNS.2021.3068001. After the publication, we were invited to include the findings in a review chapter on methods for determining carrier lifetime and mobility. The resulting chapter is published in the Springer book "High-Z Materials for X-ray Detection" [19].

5.1.1   Introduction and motivation

Heavy element semiconductor compound materials, such as CZT, has proven to be valuable as detector materials in a wide range of applications, including medical imaging, security, and space exploration. The larger band gap allows for room temperature operation, while the high atomic number ensures a higher quantum efficiency. Despite the considerable potential, CZT does face certain limitations. Charge trapping within the material leads to ineffective charge collection, and the challenge of producing defect-free single crystals hinders the growth of larger crystal sizes. Furthermore, the crystalline structure of the material can exhibit inhomogeneous quality.

When charges drift in the CZT detector material, the resulting generated pulse shapes are directly related to the electrode geometry, as explained by the Shockley-Ramo theorem [24, 25] (see Section 2.3.4). Additionally, material properties such as carrier mobility and lifetime (see Section 2.3.2.2) have an impact on the shapes of the generated pulses.

Conventional methods for evaluating the $\mu\tau$-product of a detector material involve assessing one value for the entire bulk of the detector. However, this approach overlooks the non-uniformity which can be present within the detector material, especially for compound semiconductors. The motivation for this work was to get an improved model for the detector, and at the same time demonstrate the possibility of mapping the material in 3D for correction purposes. Furthermore, this work would demonstrate how the sub-millimeter resolution of the detector can be utilized.

5.1.2   Experimental setup and data analysis

In the paper (Appendix A), the overall flow of the study is described. The experimental setup and methods for estimating the mobility and lifetime of the electrons is described in Section II, titled "MATERIALS AND METHOD". The data preparation for the analysis is described in Section III, titled "DATA PREPARATION". The final 3D analysis of the detector bulk is described in Section IV, titled "DATA ANALYSIS". A summary of these aspects of the paper will be given in this section.

5.1.2.1   Measurement procedure

For the analysis, the 3D CZT drift strip detector prototype (see Section 4.4.1) was used. The radioactive source used for the analysis was a ^{137}Cs source, to ensure photon interactions in

the entire detector bulk. The source was placed at a distance of 20cm from the anode plane of the detector. It was necessary to acquire large amounts of data, since the material properties were evaluated in several small volumes inside the detector. Therefore, we acquired 20 hours of measurements for each bias setting. In Figure 5.1, the experimental setup for the detector is shown. The source was aligned at the center of the detector anode plane using a laser. This setup remained stationary throughout the data acquisition period. Only the operating bias was changed between measurements. This varies the electric field strength in the detector, resulting in a variation in the electron drift time and charge trapping. Six different bias settings were used varying the cathode bias from -150 V to -400 V in steps of -50 V. The drift bias was set to a third of the cathode bias, however, with a maximum value of -120 V. Every measurement was taken at a high threshold setting, such that only the photopeak and edge of the Compton continuum were sampled. In TABLE I in the paper (Appendix A) the cathode and drift voltage bias settings for each measurement are summarized.

5.1.2.2   Data preparation and analysis

To determine the mobility and lifetime of the electrons in the detector bulk, it was necessary to acquire information about anode pulse height, electron drift time, electron drift distance, and electric field strength. Furthermore, the sub-division of data into smaller volumes also requires 3D intrinsic position information. For each data set the following data preparation procedure was used:

- Read raw data, calculate anode pulse heights, and sort the data using the procedures described in Sections 4.5.1 and 4.5.3. From the sorted data, only single interaction event data was further considered.

- With gain calibrated data, the 3D position of each interaction using the method described in Section 4.5.4 was calculated.

- Determine electron drift time for each interaction using the method described in Section 4.5.6.

This resulted in a data set for each bias setting containing the necessary information to continue the analysis. The position information was used for the sub-division of the data, which enabled

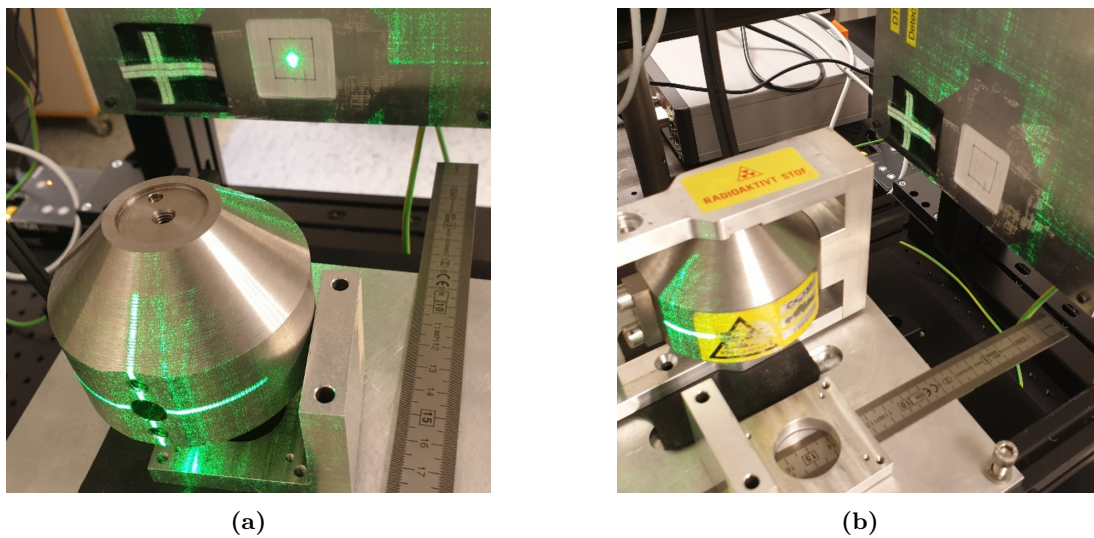(a)   (b)

Figure 5.1: Experimental setup for the electron mobility and lifetime study. (a) The source housing was aligned to the center of the 3D CZT drift strip detector using a laser. (b) Full illumination measurements were performed at varying operating biases.

the mapping of the material properties in the detector. In the study, a subsection of the detector volume was chosen for the analysis. The volume is defined in Figure 5 in the paper (Appendix A). Utilizing the 3D position information of each data point, the subsection was partitioned into virtual sub-volumes. All data inside a sub-volume was used to extract the charge carrier properties within the given volume.

Initially during the study, the electric field strength was evaluated assuming it to be equal to that of a planar detector. However, as the final look-up table and modelled pulse shapes were compared to real data, it indicated that the planar field assumption resulted in a slight underestimation of the mobility and lifetime. Instead, the electric field strength was calculated using the 3D CZT drift strip detector model in COMSOL. The electric field strength is governed by the applied bias of the measurement, therefore six values for the electric field strength was extracted, one for each bias setting.

5.1.2.3 Determining the electron mobility and lifetime

In the study, first the $\mu_e \tau_e$-product is calculated, and then τ_e. Using the relationship between these parameters, μ_e can be determined. The equations used to determine the electron mobility lifetime product and electron lifetime is summarized in this thesis in Section 2.3.2.2 in Eq. (2.22), and Eq. (2.23).

The detector volume was divided into small sub-volumes of sizes 0.4 mm along the x-direction, 0.2 mm along the y-direction, and 1 mm along the z-direction. TABLE II in the paper (Appendix A) summarizes the data division boundaries for the 3D map. Data within each sub-volume was extracted from the position information of the interactions, and for each sub-volume the electron drift distance, electron drift time, and anode pulse height were determined. The electron drift time and anode pulse height were determined by fitting a Gaussian to a distribution of each. The peak position of the Gaussian was then used as the value for the given volume. Figure 6 in the paper (Appendix A) illustrates this process.

Furthermore, to determine $\mu_e \tau_e$ and τ_e with the aforementioned methods, it was necessary to know the electron drift distance. However, due to the non-planar nature of the detector, the electron drift distance varies, especially along the x-direction of the detector. The shape of the electric field lines in Figure 4.1 illustrates this. For a planar detector, the drift distance and interaction depth will be equal. For the 3D CZT drift strip detector, this is only true for events occurring directly above the anode. Therefore, for events above the anode the drift velocity could be calculated, and then used to calculate the remaining drift distances by knowing the electron drift times. The calculated electron drift velocity is given in Eq. (12) in the paper and an illustration of the difference in drift distances in a single drift cell is given in Figure 7 in the paper (Appendix A). The electron drift distance for the volume was then extracted by multiplying the electron drift time with the calculated electron velocity.

Knowing the electron drift distance, anode pulse height, and electron drift time for each sub-volume of data in the detector now allowed for determining $\mu_e \tau_e$ and τ_e. For a set of six bias measurements, where i indicate measurements 1 to 5, the relation in Eq. (2.22) (see Section 2.3.2.2) was used to assess the $\mu_e \tau_e$-product. Measurement number 6 indicates the measurement taken at the highest bias voltage. A plot of $\ln\left(\frac{N_i}{N_6}\right)$ as a function of $\left(\frac{1}{E_6} - \frac{1}{E_i}\right)$ was fitted with a linear regression model, where the slope of the fit corresponds to $\frac{y_d}{\mu_e \tau_e}$. Knowing the drift distance of the given sub-volume, $\mu_e \tau_e$ for that given sub-volume could be extracted. A similar process was applied using Eq. (2.23) (see Section 2.3.2.2) to extract τ_e for each sub-volume. After the extraction of $\mu_e \tau_e$ and τ_e, the mobility was extracted by $\mu_e = \frac{\mu_e \tau_e}{\tau_e}$.

Lastly, the resulting maps of the electron mobility and lifetime were evaluated using the 3D CZT drift strip detector model.

5.1.2.4   The 3D CZT drift strip detector model

The 3D CZT drift strip detector model is a combination between COMSOL and Python. In COMSOL, the geometry of the 3D CZT drift strip detector is defined. This includes detector bulk size, and electrode specifications. The electrostatic conditions of the detector is then calculated, and the resulting electric field strength and weighting potentials extracted. The weighting potentials in the detector are used to calculate the pulse shape formation in the detector. An example of weighting potentials, calculated using COMSOL was illustrated in Figure 4.2. The Python part of the model handles the charge transport properties and calculation of the induced signal.

The model calculates the induced signal and trapping of electrons and holes, for each step between the moment the charges start to move until sample length is reached. The model extracts the electric field strength and weighting potential for the charge position and saves it for the induced signal calculation at the end. For each step, the charge movement and trapping is updated, until collection or until sample length is reached. After the iterative calculation, the induced signal is calculated for each of the contributing charges, and the cumulative sum of the induced signal is calculated to get the fully generated pulse shapes. It then returns the pulse shapes, together with charge carrier drift paths. The current state of the model assumes the charges to be a single point, and does not take into account the volume of the charge clouds. The flow of the 3D CZT drift strip detector model is summarized in Algorithm 2.

Algorithm 2 The 3D CZT drift strip detector model

Require: COMSOL input: electric field distribution and weighting potentials.
Require: User input: sample time T_s (def. 4ns), sample length (def. 1000), start sample time, initial position (x, y, z), μ_e, τ_e.

    Initialize arrays for e^-/h^+ trapping and drift path, and 26 pulse shapes.
    for i'th step in sample start time to sample length **do**
        if e^- are not collected **then**
            Determine electric field strength and weighting potential at i'th e^- position.
            Update signal: Save the interpolated weighting potential at position for each 26 channels.
            Update i'th e^- drift path with: $de_i^- = \mu_e E_i T_s$ (Eq. (2.17))
            Update i'th e^- trapping with: $q_i = q_{i-1} \cdot \exp(-de_i^-/\lambda_e)$ (Eq. (2.18)), where $\lambda_e = \mu_e \tau_e E$ (Eq. (2.20)).
        end if
        The above if-statement is repeated for h^+.
    end for
    For each step calculate e^- and h^+ contribution to the signal, $Q = q\Delta\varphi$ (Eq. (2.29)).
    Induced signals: Calculate the cumulative sum of the two contributors to the induced signals to get the fully generated pulse shapes.
    return Induced signals, electron drift path, hole drift path.

5.1.3   Results and discussion

In this paper, we demonstrate the feasibility of utilizing the 3D spatial-sensitive nature of the 3D CZT drift strip detector to map μ_e and τ_e within the detector. A lookup table of material properties allows us to enhance the response of the 3D CZT drift strip detector model. Furthermore, it underlines the possibility of creating a correction table for the detector response.

The results are presented in Section V, titled RESULTS in the paper (Appendix A). Three lookup tables were generated; the $\mu_e\tau_e$-product, the electron lifetime τ_e, and lastly the electron mobility μ_e, presented in Figures 8, 9, and 10 in the paper (Appendix A). All uncertainties were determined using error propagation. The $\mu_e\tau_e$-product displayed a clear non-uniformity along the sub-volume of the detector with a factor of three. Especially along the x-direction, the variation was large. The variation along the z-direction could not be assessed in a similar fashion, since the step-size was large, and only a small part of the z-direction was included in the study. A variation similar to that of the $\mu_e\tau_e$-product was observed for the map of τ_e,

with variations larger than the calculated error. For μ_e the error was larger than the observed variation, and therefore we did not draw any conclusions on the non-uniformity of μ_e. However, we did extract a mean value almost a factor of two larger than the nominal value provided by the crystal manufacturer. The determined electron mobility and lifetime were compared to the manufacturer values in Table III in the paper (Appendix A). The 3D maps of the material non-uniformity were included in the 3D CZT detector model, resulting in a clear improvement in the model performance, an example of this is given in Figure 12 in the paper (Appendix A).

The study showed us that the 3D nature of the detector allows for a 3D mapping of the charge carrier properties. Not only can this be used for model improvement, but also as a look-up table for data correction to further improve detector performance. Knowledge of the detector material is essential for thorough understanding and characterization of the detector. Areas of severe charge trapping or poor charge transport can be mapped out and included in the models as well. Furthermore, a reliable model depicting the pulse shape formation in the detector can be used as training data for future artificial neural network models, which can be a crucial for data size reduction.

Further work on this project could be to extract maps of the material properties for an entire detector bulk, also with a smaller slicing along the z-direction. Extracting μ_e on its own, by applying the TOF method could deem interesting, if the uncertainty could be reduced. Furthermore, the study did highlight that the current values for the hole material properties do not align with the experimental data. The holes display better mobility/lifetime than assumed. Therefore an investigation of the hole properties can further improve the model. Moreover, the current state of the model only takes into account a single point charge. An expansion of the model to take into account the charge cloud size generated by the photon interaction would further improve model response. Lastly, diffusion (Section 2.3.2.3) must be added to the model as well.

5.2 Paper 2: Evaluation of CZT Drift Strip Detectors for use in 3-D Molecular Breast Imaging

Evaluation of CZT Drift Strip Detectors for Use in 3-D Molecular Breast Imaging

S. R. H. Owe, I. Kuvvetli, A. Cherlin, B. Harris, H. Tomita, I. Baistow,
D. Tcherniak, and C. Budtz-Jørgensen

The second paper published during this thesis work is a characterization study of the 10 3D MBI test modules (see Section 4.4.2). The initial results were presented as a poster at the IEEE NSS MIC RTSD 2021 conference. This was early in the characterization process, and the work continued after the conference. The final results were presented in an oral presentation at the Annual Danish Astronomy Meeting in Fredericia, Denmark in 2022. In June 2022, the final results were submitted to IEEE Transactions on Radiation and Plasma Medical Sciences, and after minor revisions accepted in November 2022 [5]. The paper is attached in Appendix B, or can be found using the link https://doi.org/10.1109/TRPMS.2022.3220807.

5.2.1 Introduction and motivation

The 3D CZT drift strip detectors were initially designed for application within X- and gamma-ray astronomy. As the detector has displayed excellent intrinsic spatial and spectral resolution, it was evident that the detector also can benefit other areas of application. A collaboration between Kromek and DTU Space commenced, since Kromek are working on an innovative concept for a stationary tomographic low-dose MBI (LD-MBI) system, which requires high resolution 3D position sensitive CZT detectors, such as the DTU developed 3D CZT drift strip detector. The collaboration resulted in the development of the 10 3D MBI test modules (see Section 4.4.2). The modules vary slightly from the 3D CZT drift strip detector prototype (see Section 4.4.1) in electrode width, and the electrode deposition did not include the oxide layer between the drift strips and the detector crystal. This study is a comprehensive characterization study, evaluating the performance of the 10 3D MBI test modules. It relates the results to the application within new emerging LD-MBI systems, and as a stepping stone towards a space-ready module.

The paper (Appendix B) introduces the LD-MBI technique in section I, titled INTRODUCTION, together with a description of the 3D MBI test module design, which was also summarized in Section 4.4.2 of this thesis. In section II of the paper, titled MATERIALS AND METHOD, the different measurement techniques and setup configurations used for the characterization work are described. The data analysis procedure used in the paper, is described in section III, titled ANALYSIS PROCEDURE. In section IV of the paper, titled RESULTS, the findings are presented. This includes an overall module performance overview, electronic noise and IV-curve measurement results, and spectral and intrinsic spatial resolution evaluated at two energies. Finally, the results are summarized in section V of the paper, titled CONCLUSIONS.

In the following sections, the experimental setup, data analysis, results, and conclusions will be summarized. Some plots which were not included in the paper will also be presented in the following sections.

5.2.2 Experimental setup and data analysis

In this section, the experimental setup used for this characterization study is summarized. This includes the IV-curve measurement setup, the electronic noise measurement setup, and the setup

used to evaluate the spectral and intrinsic spatial resolution of the detector.

All measurements were carried out in the DTU Space detector laboratory. During the project, the measurement time exceeded the initially projected time frame. Instabilities in the setup resulted in measurements to be repeated due to unstable signals and loose connections. Thus, whenever signals were unstable, it was necessary to remount detectors, and make sure every measurement was repeatable. In the end, measurements of all modules were successfully carried out.

5.2.2.1 Electronic noise measurements

The electronic noise measurements are essential to evaluate the detector performance. It will have an impact on the pulse shapes, and the spectral resolution of the detector, as described in Section 2.2.1.3. While the task of determining the electronic noise is essential, it is also rather simple. A test pulse input is integrated in the readout electronics for the detector. A test pulse is connected to the readout electronics, and data is measured using the normal procedure. Analyzing the data set, a pulse height histogram can be generated for all channels. Fitting a Gaussian to the resulting distribution makes it possible to determine the FWHM of the pulse height distribution, where the only contributor to the spread is the electronic noise. In an attempt to reduce the electronic noise in the system, a special box for the electronic readout was manufactured, screening each charge sensitive pre-amplifier from each other. This attempt was unsuccessful since the electronic noise persisted.

The electronic noise measurements were taken with and without the HV bias applied to the detector. This allowed for investigating the electronic noise contribution for the detector in its idle mode and operational mode. In the idle mode, the cathode bias was $V_c = 0$ V and drift bias $V_d = 0$ V. In the operational mode with HV applied, the biases were set to $V_c = -450$ V and $V_d = -150$ V.

5.2.2.2 IV-curve measurement

Current-voltage (IV) curve measurements are used to electrically characterize the detectors by assessing resistivity and electrode-material contact. The 10 3D MBI test modules were all characterized in an IV-curve measurement setup [5]. In Figure 5.2 images of the IV-curve setup are shown. The setup consist of a PCB connected to an array of mechanical relays, which configure the electrode bias setup. On top, the 3D MBI test modules can be easily swapped

Figure 5.2: The IV-curve measurement setup for the 3D MBI test modules. Modules can be easily swapped, and a light shield is placed on top. A PCB connects the detector to a mechanical relay system. A Keysight B2085A electrometer is connected to the system for both voltage and current measurements.

between measurements. A light shield is mounted over the detector during measurements. A Keysight B2085A electrometer is connected to the setup and performs both voltage and current measurements. Both surface and bulk leakage current measurements are possible, and are carried out using a Python script.

A schematic of the two configurations is given in Figure 4 in the paper (Appendix B). For the bulk leakage current measurements, all anodes and drift strips are grounded, whilst a voltage is applied to the cathode. The current flowing through the bulk is then measured for the given voltage step. The surface leakage current is measured by grounding all electrodes except for a single anode, where the voltage is applied. The current flowing from the given anode to the nearest drift strips are then measured [5]. Measurement are taken for a range of voltages, and between each measurement a settle time of 3 minutes is implemented for the system to stabilize.

The bulk IV-curve measurements were taken in a range from -450 V to 50 V, since -450 V is the largest bias applied for the cathodes in normal operational mode. The surface leakage current measurements were taken from -50 V to 50 V, since -50 V is the bias applied to the nearest drift strip to the anode.

5.2.2.3   Flood/full illumination measurements

Flood/full illumination measurements indicate that the source is uncollimated and illuminate the entire detector. The 3D MBI test modules were all illuminated at the cathode plane. For the energy/gain calibration measurements, three sources were included, see Table 4.2. For detector characterization purposes, only ^{57}Co and ^{137}Cs were used. Characterization using ^{57}Co was used to evaluate the detector performance close to the energy used for MBI (140 keV). Characterization using ^{137}Cs was used to allow comparability to previous versions of the detector, which were only evaluated at this energy.

5.2.2.4   Slit beam measurements

To determine the intrinsic spatial resolution of the 3D MBI test modules, is to evaluate how well the detector can measure the interaction position of photons in the detector bulk. To do so, a collimated beam is used. This can either be a pencil beam (small spot size) or a slit beam (long thin illumination). In the detector laboratory at DTU Space, a slit beam collimator is constructed. It is a rather simple configuration, consisting of two tungsten bricks, which are fixated close together with an opening of 0.2 mm. The beam is thereby only collimated in one direction. In the other direction the opening is 80 mm, ensuring the slit to illuminate the entire detector. In Figure 5.3, the measurement setup for the spatial scan (left) and the slit beam collimator (right) is shown. The setup consists of a source placed behind the slit beam
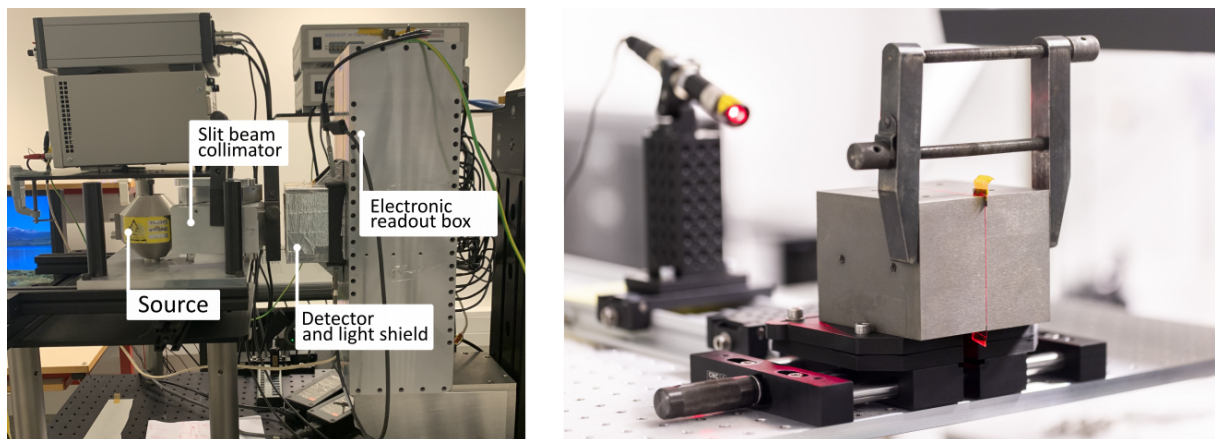

Figure 5.3: (Left) Experimental setup for slit beam measurements for spatial resolution determination. (Right) Tungsten slit beam collimator and laser for alignment.
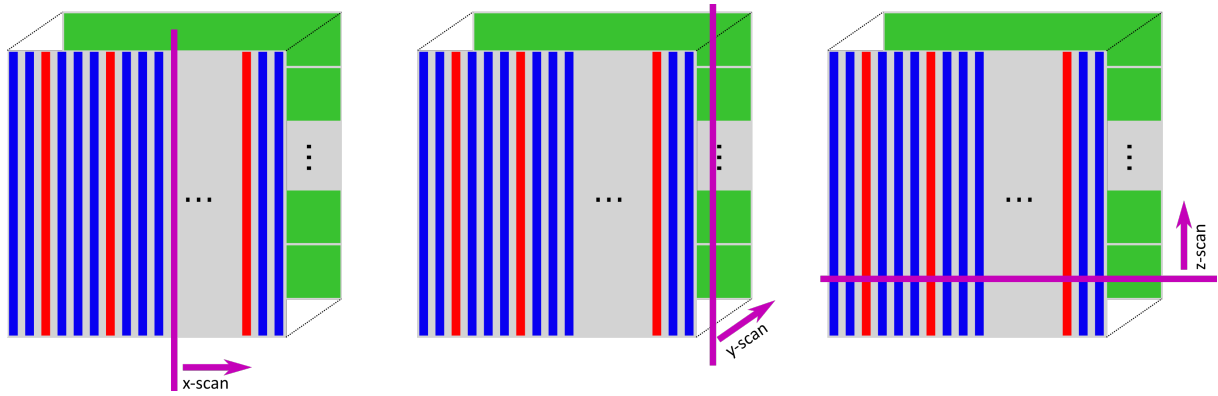
Figure 5.4: Illustration of the slit beam scan directions for spatial resolution determination.

collimator. This ensures that the beam is collimated, resulting in a thin line illuminating the detector surface. The small distance between the collimator opening and the detector surface results in a slight divergence in the beam. The consequence of this is a broader line illuminating the detector, than the slit beam opening. This is not an issue, as long as the beam illuminating the detector is smaller than the intrinsic spatial resolution of the detector. The detector and its electronic readout is mounted on a three-axis stepper motor, allowing for movement of the detector relative to the slit beam opening. A LabVIEW program for scan measurements allows for defining a scan procedure. General measurement settings are defined, as well as number of measurements, and the stepper motor step size movement between. In this setup, a step size of 0.5 mm was used. In Figure 5.4, an illustration of the beam illumination direction for the three dimensions of the detector is shown. When evaluating the position resolution of a given dimension of the detector, the detector is moved in small steps along the given direction. Due to the setup design for the 3D MBI test modules, it was unfortunately not possible to scan the detector along the y-direction. Therefore, only scans along the x- and z-directions were conducted. Further information of the DTU Space detector laboratory setup is given in Section 4.3.

5.2.2.5   Data analysis
The characterization of any 3D CZT drift strip detector, depends strongly on the data analysis tools, described in Section 4.5. In Figure 8 in the paper (Appendix B), an overview of the data analysis procedure is shown. The raw data is read as described in Section 4.5.1 and sorted using the sorting algorithm described in Section 4.5.3. Only single interaction events are then considered for the further analysis. The data is energy/gain calibrated, as described in Section 4.5.2. The 3D position of each interaction is then calculated, as described in Section 4.5.4, followed by a 3D correction of the energy, as described in Section 4.5.5.

5.2.3   Results and discussion
In this section, the findings of the paper will be summarized, together with presentation of additional data, which were not included in the paper. The results are presented in the paper in section IV, titled RESULTS (Appendix B).

The overall performance of each 3D MBI test module is described in Section IV-A of the paper, titled *Overall Module Performance.* An overview of the performance of the 10 detector modules are given in TABLE II in the paper (Appendix B). When assessing the overall module performance of the detectors, data from flood illumination measurements were used. The resulting pulse height histograms of anodes and cathodes were investigated to identify any missing or attenuated signals. Additionally, 2D-histograms of the spatial event distribution were investigated to identify any odd detector behavior or grain boundaries. An example of pulse height

histograms for anodes and cathodes together with 2D-histograms of the spatial event distribution is given in Figure 5.5 for module B2D4 and in Figure 5.6 for module B2D6. For the case of module B2D4, no issues were detected. All pulse height histograms show clear photopeaks for the anodes and edges for the cathodes. The spatial distribution is also even throughout the entire detector volume, only known artifacts from the position algorithms are evident. For module B2D6, clear issues could be identified. Anode 9 showed no signal in the pulse height histograms, and cathodes 3, 5, and 6 also showed missing signals, resulting in an unusual distribution in the 2D-histogram showing the spatial distribution of events.

Figure 5.5: Example of a flood illumination measurement of the module "B2D4" with ^{137}Cs. (Left) Pulse height histograms of anodes and cathodes, and (right) a 2D plot of the spatial hit distribution to the right.
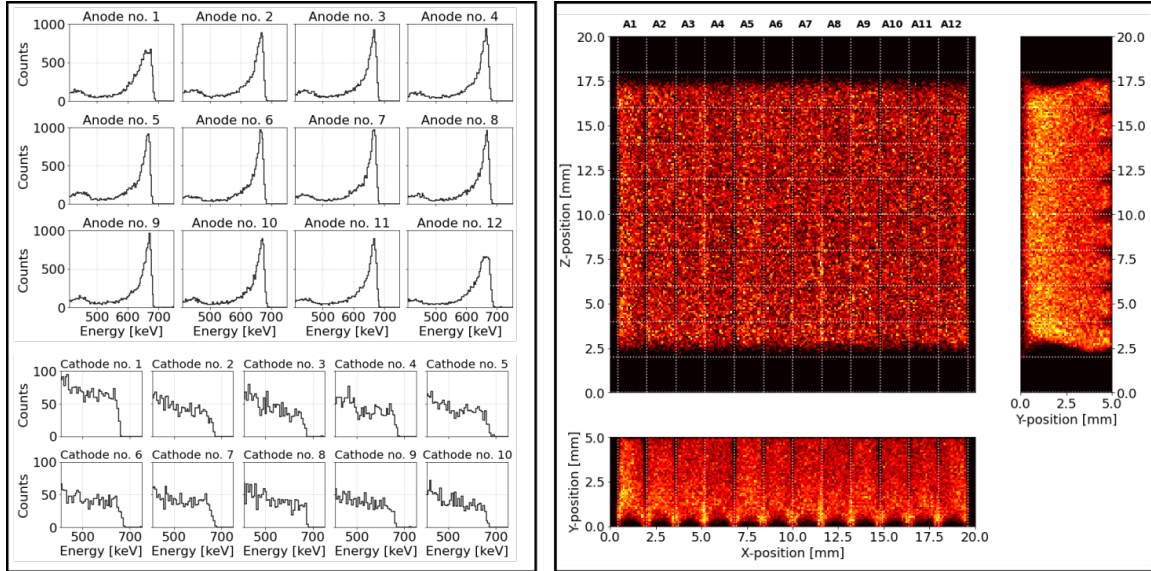

Figure 5.6: Example of a flood illumination measurement of the module "B2D6" with ^{137}Cs. (Left) Pulse height histograms of anodes and cathodes, and (right) a 2D plot of the spatial hit distribution to the right.
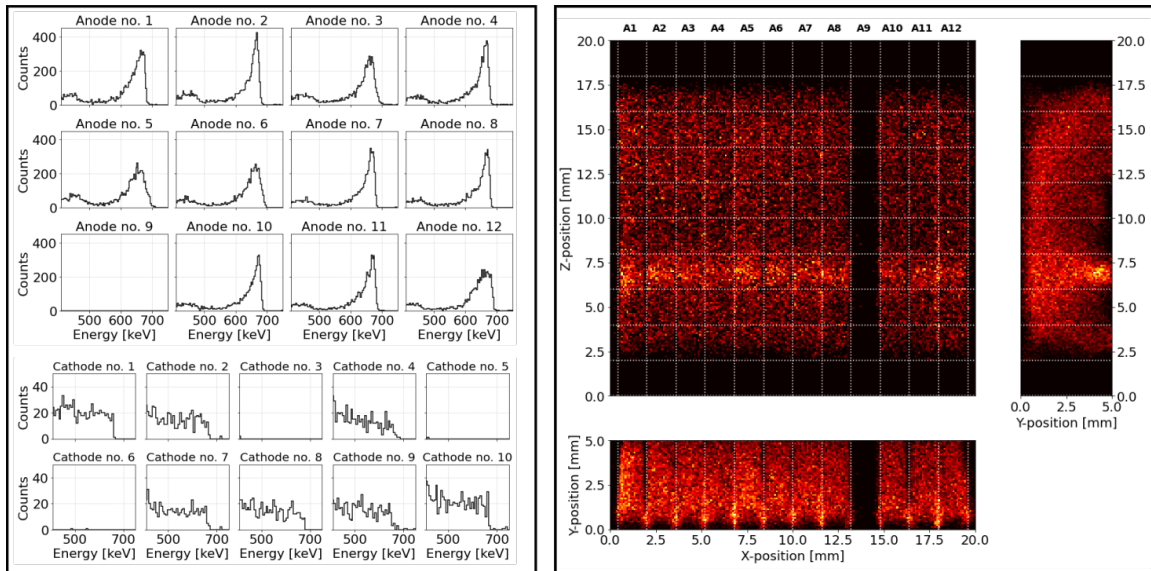
In other cases, an attenuated signal can be caused for example by a grain boundary in the material. This was the case for the detector named B1D1. A clear boundary was evident along the extent of anode number 9. Figure 9 in the paper (Appendix B) illustrates this for a measurement at 122 keV. In Figure 5.7, the same plot is given, but for the measurement at 661.6 keV.

Inspecting the 2D-histograms of detector module B1D2 showed an odd behavior in an area around anode 8 and 9. An analysis of the signal response in this area of the detector showed missing signal for drift strip 1, which resulted in the x-position algorithm not working. The resulting image is shown in Figure 10 of the paper (Appendix B).

The overall performance of the detector modules showed that five detectors had no detected issue from pulse height and spatial distribution inspection. The other five modules had different issues, some just a grain boundary, others missing, attenuated, or noisy signals. The worst case was that of module B2D6.
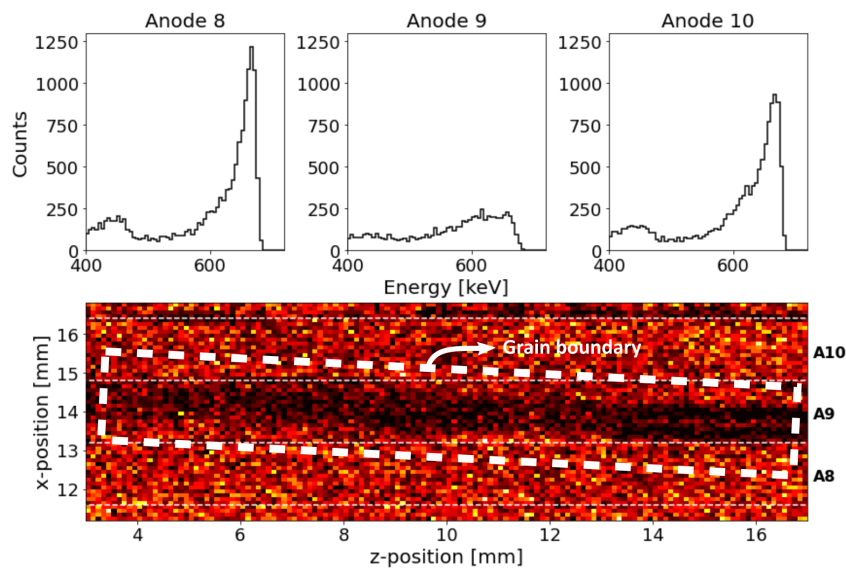

Figure 5.7: Pulse height histograms of anodes 8, 9, and 10 together with the 2D-histogram of the interaction positions in the detector, for data acquired with at 661.6 keV. A clear grain boundary is seen in the area where anode number 9 collects the electrons for module "B1D1".

The electronic noise was measured for each module with and without HV applied. Figure 11 in the paper (Appendix B) illustrates the FWHM of the electronic noise measured with a test pulse for each channel connected to the detector. For some electrodes a clear connection between electronic noise and spectral performance or leakage current could be detected. For others, no direct connection was evident.

The bulk and surface leakage current is presented in Figure 12 and 13 in the paper (Appendix B). However, the surface leakage current presented in the paper, only included measurements taken at -50 V. The measurements were taken in a range from -50 V to 50 V, and all measurements are illustrated in Figure 5.8. The substantial increase in surface leakage current in anode 11 for module B1D2 was directly connected to the electronic noise of the same electrode. A clear difference between the first detector batch (B1D1-B1D4) and the second detector batch (B2D1-B2D6) was evident. Surface leakage current for batch two was in the order of nanoampere, where larger leakage current existed for batch 1. This was an important finding, since a surface leakage current in the order of nanoampere was a goal in terms of using a more simple electrode deposition method, than that of the prototype detector.

For the case of the bulk leakage current, there were some differences between the first and second batch. This could be connected to the fact that it is not possible to control the crystal orientation when dicing the crystals in the manufacturing process. However, module B2D6 did show a large leakage current, which was noticeable since the detector itself in general displayed a bad performance.
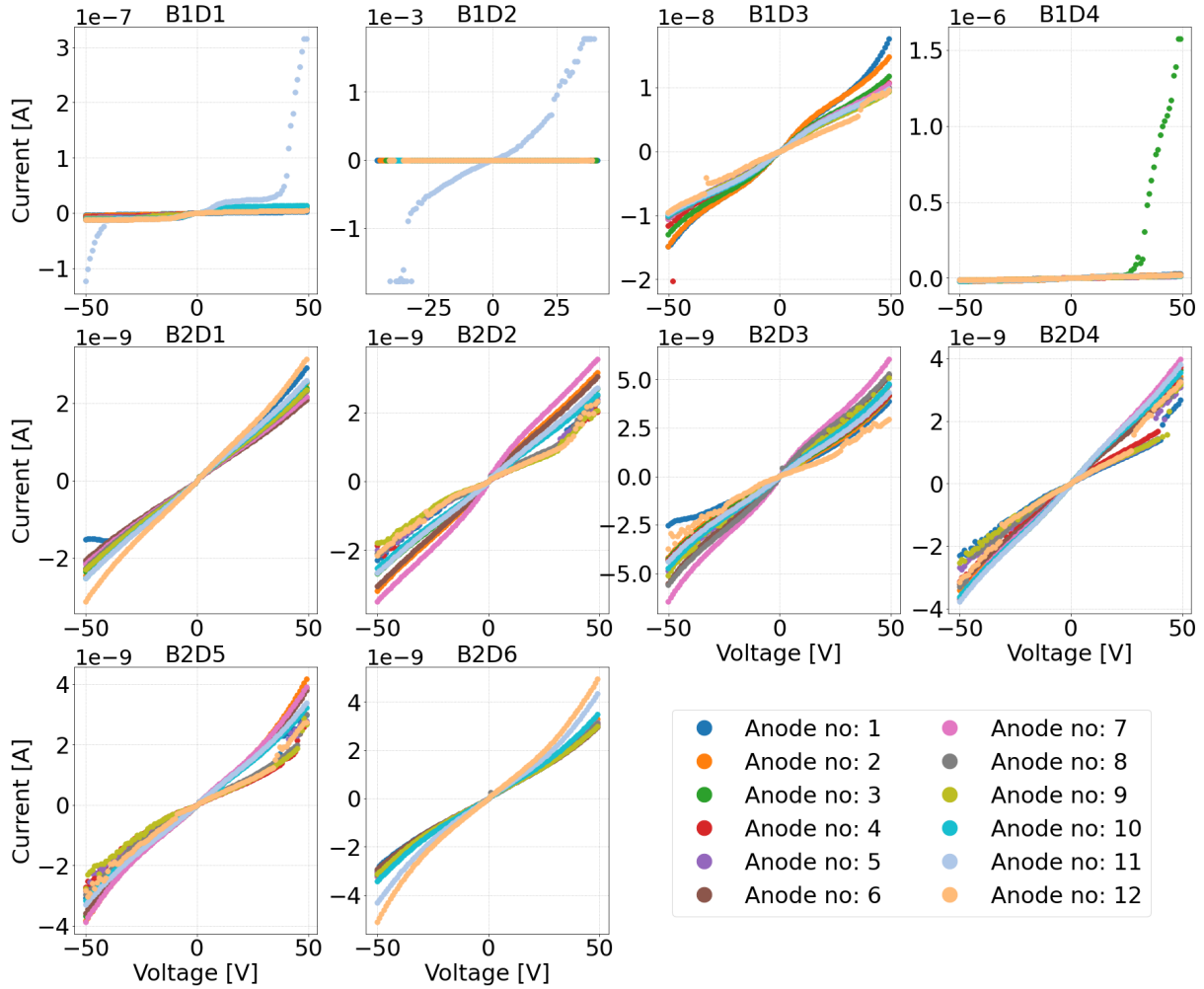

Figure 5.8: Surface leakage current measurements of the anodes for all 3D MBI test modules

The spectral resolution of the modules were evaluated using the sources ^{57}Co and ^{137}Cs, and the results are given in Figure 14 in the paper (Appendix B). The energy resolutions presented, are after energy correction in terms of spatial distribution, as described in Section 4.5.5. The energy resolution for each anode is plotted, and at the same time the total energy resolution is given. For a majority of the modules, the anode energy resolutions are comparable to each other. For other modules, some anodes displayed worse energy resolution, either related to the electronic noise or attenuated signals. The overall results were that at 661.6 keV the energy resolution was ranging between 1.3% and 1.9%. At 122 keV the energy resolution was ranging between 6.7% and 9.3%. Module B2D6 clearly displayed the worst resolution, which was not surprising due to the many issues associated with the module. For module B1D1, anode 9 suffered a poor resolution, due to the grain boundary. For module B1D2, anode 11 suffered a poor resolution, due to the significant electronic noise issues associated with the given anode, as is evident in Figure 5.8.

Through these results, it was clearly underlined that an improvement in the electronic noise is

absolutely essential if the detector is to be used for low-energy applications, requiring a good spectral resolution.

The spatial resolution of the modules were evaluated in the x- and z-directions using slit beam measurements with ^{57}Co and ^{137}Cs. An example of five scan data sets along the z-direction at 661.6 keV is plotted in Figure 5.9. Here, the five locations of the slit beam illuminations are clear. To the right, the 1D-histogram distribution of the calculated z-positions is shown. For the entire set of scans, these were fitted with a Gaussian to evaluate the FWHM of each scan distribution. The mean value of all FWHM for a set of scans is then referred to as the z-position resolution for the given detector. The intrinsic spatial resolution was evaluated within some boundaries, such that only the areas currently covered by the 3D CZT drift strip detector algorithm were included. The boundary conditions were as follows: 0 mm $< x <$ 20 mm, 1 mm $< y <$ 5 mm, and 2 mm $< z <$ 18 mm.
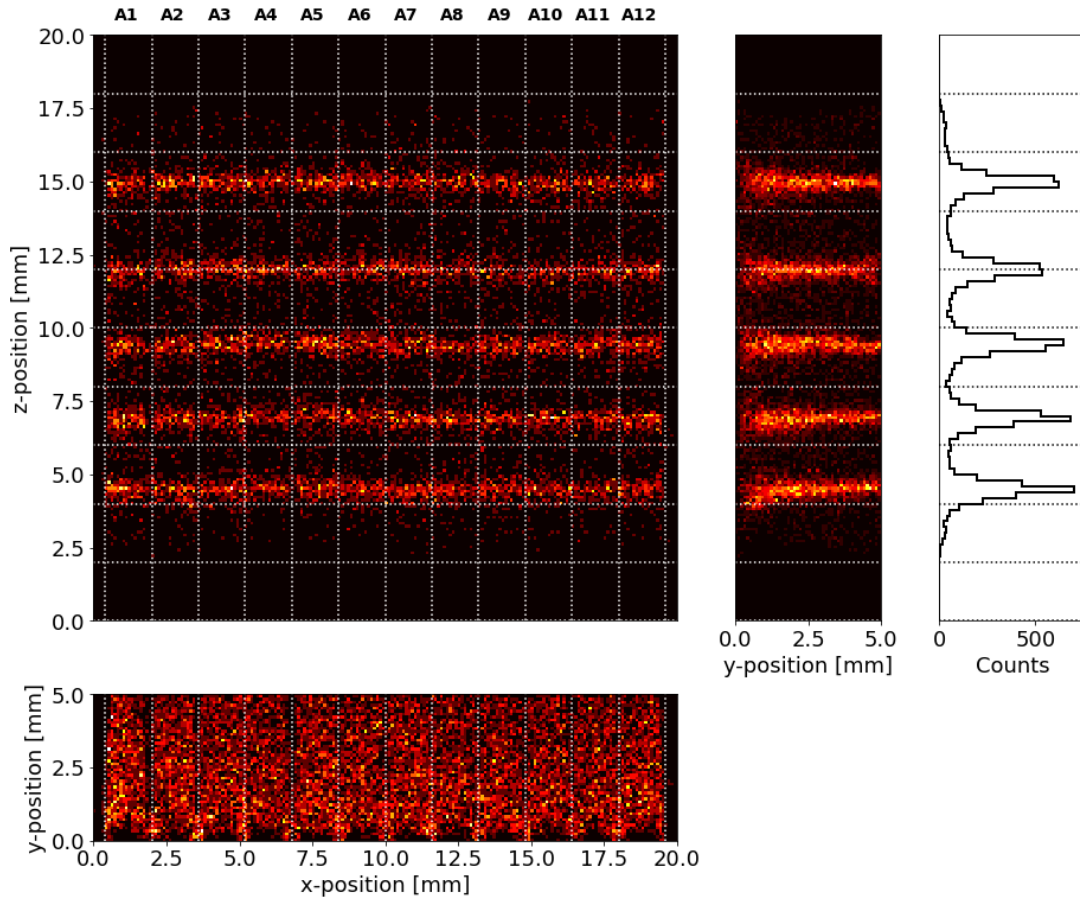

Figure 5.9: 2D histograms illustrating the position information for five slit beam measurements in the z-direction. In the 1D-histogram to the right, the spatial distribution of the z-position can be fitted with a Gaussian, to determine the FWHM of the z-position.

The intrinsic spatial resolution of the detector is illustrated in Figure 15 in the paper (Appendix B). Excluding module B2D6, the overall intrinsic spatial performance of the detector was as required. Along the x-direction of the detector, the FWHM position resolution was below 0.5 mm at 661.6 keV, and below 0.7 mm at 122 keV. Along the z-direction, the resolutions were centered around 0.55 mm at 661.6 keV and around 0.65 mm at 122 keV. The worse intrinsic spatial resolution at the lower energy can be directly attributed to the electronic noise. The S/N ratio is smaller for the pulse shapes measured at 122 keV, resulting in the algorithms performing worse. Module B2D6 performed fine in the x-direction, but in the case of the z-direction, the

three missing cathode signals consequently resulted in a very bad intrinsic spatial resolution.

Even though the resolutions could be better, especially at the lower energy, the modules displayed a sub-millimeter position resolution in the x- and z-directions. Reducing the electronic noise of the system could improve the intrinsic spatial resolution at lower energies, however, the sub-millimeter resolution still complies with the requirements of the LD-MBI system.

In summary, a full characterization work of the 10 MBI test modules was carried out with positive results. A key finding of this paper, was that the leakage current and overall performance of the modules were within the desired range, even though the 10 modules were fabricated with a simpler electrode deposition process compared to the 3D CZT drift strip detector prototype. This allows for simpler manufacturing of future modules. Additionally, five of the modules performed as expected with no severe grain boundaries, and no missing, noisy, or attenuated signals. Four detectors displayed minor issues, such as grain boundaries or missing, noisy, or attenuated signals, however, the detectors still displayed sub-millimeter position resolution and acceptable energy resolution. Only one module, B2D6, suffered significantly worse than the rest, displaying considerably worse spectral and z-position resolution.

The study elevated the 3D CZT drift strip detector technology to a more modular design with a simpler electrode geometry while still displaying sub-millimeter intrinsic spatial resolution, moderate spectral resolution at 122 keV, and good spectral resolution at 661.6 keV. Advances in the overall setup and a dedicated ASIC (application-specific integrated circuit) can reduce the dominant electronic noise and help further improve the spectral resolution of the detector. Lastly, it concluded that the 3D CZT drift strip detector technology can be a great choice of detector for future emerging MBI technologies.

5.3 Paper 3: Feasibility of Using 3D CZT Drift Strip Detectors for Small Compton Camera Space Missions

5 Feasibility of Using 3D CZT Drift Strip Detectors for
6 Small Compton Camera Space Missions

7 S. R. H. Owe[a,1] I. Kuvvetli[a] A. Zoglauer[b] C. Budtz-Jørgensen[a]

8 [a]DTU Space, Technical University of Denmark
9 Elektrovej building 327, 2800 Kgs. Lyngby, Denmark
10 [b]University of California, Berkeley,
11 Space Sciences Laboratory, 7 Gauss Way, Berkeley, CA 94720, USA

12 E-mail: shoowe@space.dtu.dk

The third and final paper produced in this thesis work was submitted to the Journal of Instrumentation (JINST) on September 28, 2023 for the proceedings section for the 24th International Workshop on Radiation Imaging Detectors (iWoRiD23). The paper presents a simulation study of a Compton camera concept using the 3D CZT drift strip detectors. The project was initially planned to be done at University of California, Berkeley under the supervision of Associate Researcher Andreas Zoglauer in the fall of 2021. However, due to implications of covid-19 on the visa application processes, the external stay was canceled. However, supervision on video-calls and e-mail continued. The work was presented with a poster at the iWoRiD23 conference in Oslo, Norway, in June 2023. The paper, which was submitted for review, is attached in Appendix C.

5.3.1 Introduction and motivation

As presented in Section 1, there exists a gap in instrument sensitivity in the MeV domain (0.1 to 100 MeV), see Figure 1.1. This is not due to a lack of scientific interest within this range. Many interesting astrophysical phenomena emit radiation in this energy band, examples span from supernova explosions to gamma-ray bursts from colliding neutron stars, accreting black holes, and pulsars. The gap in sensitivity exists due to the inherent difficulty in observing this energy range. The sources have a low flux, while the radiation background in this range is rich. The detector material poses low interaction probability with the radiation emitted in this domain, and when the radiation interacts, it can do so by three different energy loss processes, as described in Section 2.1. It was described in Chapter 3 that the Compton camera instrument is deemed to be a good candidate to lower the sensitivity in the MeV domain. However, excellent detector technology with good spectral and spatial resolution is required for the Compton camera. It has previously been demonstrated that a single 3D CZT drift strip detector can be operated as a Compton camera [65], which makes it a good candidate to be included in future Compton camera instrumentation. Identification of several interactions within the same detector bulk is favorable when observing low flux sources.

This study investigates the feasibility of operating the 3D CZT drift strip detector on a small Compton camera payload, for example on a CubeSat to improve the detector TRL. The paper

(Appendix C) introduces the study and presents the 3D CZT drift strip detector in Section 1, titled "Introduction". The method and simulation pipeline is presented in Section 2, titled "Model setup". The results from the simulation study is presented in Section 3, titled "Payload performance". And finally Section 4, titled "Conclusion" wraps up the paper. In the following sections, the paper and its conclusion will be summarized.

5.3.2   Method and simulation pipeline

The simulation pipeline follows a range of different simulation runs and data analysis to assess the different points in the simulation pipeline. All parameters extracted from the simulation software were stored in a spread sheet. The simulation pipeline is specifically related to the simulation software MEGAlib (The Medium-Energy Gamma-ray Astronomy library) [70] in which the study was conducted.

The analysis procedure used in the paper (Appendix C) required a variation of different simulations. An overview of the procedure is given in Table 5.1. First, the basic telescope performance parameters were evaluated. This is done both for nuclear line and continuum emission sources. Next, the sensitivity of the telescope is calculated for nuclear line and continuum emission sources. This includes a simulation of the background environment, which is necessary for the sensitivity calculation. Lastly, in-orbit simulations of astronomical sources were performed, to evaluate the feasibility of such an instrument concept.

The overall simulation process for this study using MEGAlib is a as follows. The geometry is defined in `geomega`. Simulations with specified sources illuminating the geometry is run using `cosima`. Next the reconstruction of Compton events is done using `revan`, and lastly image reconstruction and other data analysis tools are done using `mimrec`.

Table 5.1: General overview of the simulation pipeline used in paper 3 in Appendix C. The background source is generated in MEGAlib with input from SPENVIS, corresponding to an orbit like that of the NuSTAR satellite. All other sources are defined as far-field point sources in MEGAlib.

Step 1:	Step 2:	Step 3:
Basic Performance Parameters	**Sensitivity Analysis**	**In-orbit Simulations**
• Energy resolution	• Narrow-line sensitivity	• Continuum: The Crab
• ARM	• Continuum sensitivity	• Transient: Bright GRBs
• Effective area		
Sources:		
• Nuclear lines (100-2000 keV)	• Nuclear lines (100-2000 keV)	• Continuum emission (Power-law: Crab)
• Continuum emission (Power-law: E^{-2} and Crab)	• Continuum emission (Power-law: E^{-2} and Crab)	• Transient (Selection of bright GRBs)
	• Background (excl. trapped components)	• Background (excl. trapped components)

The geometry defined in `geomega` includes specifications of passive materials and detector specifications. The geometry for the simulation is described in Section 2.2 of the paper (Appendix C) titled "Instrument model". The detector implemented in the simulation software was the 3D MBI final module, see Section 4.4.3. However, since this detector type has not been characterized

yet, the spectral and spatial resolution were based on the performance of previous detector modules. Furthermore, a 1 cm passive shielding using the scintillator CsI was included in the geometry. The geometry implemented in MEGAlib is illustrated in Figure 1 in the paper (Appendix C).

The sources are also defined in specific files for `cosima` to read. The background source is generated in MEGAlib with input from Spenvis [1], corresponding to a Low Earth Orbit (LEO) like that of the NuSTAR satellite. All other sources are defined as far-field point sources in MEGAlib. Four source types were included in the analysis: Nuclear lines, continuum emission, transients, and background. The orbit chosen for the simulation governed the background of the instrument. The resulting contributors to the background are illustrated in Figure 5.10. The trapped components were excluded from the analysis, since we assume the instrument to be off during South Atlantic Anomaly (SAA) passages. Nuclear line sources were defined as monochromatic far-field point sources, continuum emission sources were defined as a power-law, either for a E^{-2} power-law, or the Crab defined as in [71]. For simulation of observations of GRBs, the Band-function was used to describe the spectral properties of the GRB. A selection of GRBs present in both 'CGRO/BATSE Complete Spectral Catalog of Bright GRBs' [72] and the 'CGRO/BATSE 5B Gamma-Ray Burst Spectral Catalog' [73] were used.
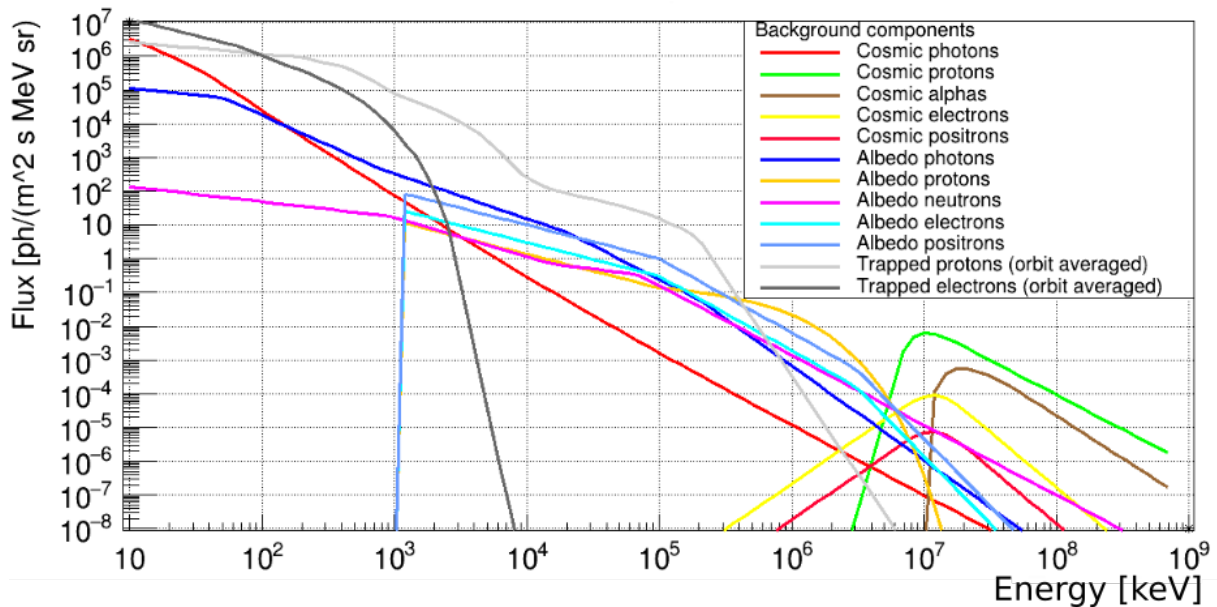

Figure 5.10: Contributors to the background environment in the simulation setup.

Simulation runs used to assess basic performance parameters must include the source alone without background. Simulations were run for each of the nuclear line sources, also at different incidence angles. Otherwise, zenith incidence angles were used for the continuum emission sources. To asses the sensitivity of the instrument, long background simulations were included. Lastly, combinations of background and astrophysical sources were run to see if it was possible to reconstruct images with visible sources.

5.3.3 Data analysis

The data analysis procedure of the paper (Appendix C) is described in Section 2.3 titled "Method", but is further described here. After all simulations are run, the Compton sequences are reconstructed using `revan`. From this, a set of reconstructed Compton sequences are defined for each simulation, and from this, data analysis can be performed. The data analysis procedure

---

[1]Spenvis: www.spenvis.oma.be/

is very similar for the nuclear line emission and the continuum emission sources, except for the energy window chosen for the analysis.

The event selection is a specification of which events are to be considered for the analysis. These specifications affect the performance of the instrument, and it is therefore essential to specify that the findings in the paper (Appendix C) account for an instrument with the following criteria:

- Trigger threshold of instrument: 20 keV.

- Only consider Compton interaction chains of 2-7 events.

- Compton scatter angles considered: 0°-180°.

- Minimum distance between any interaction: 1.6 mm.

The energy resolution is determined for each of the nuclear line emission sources. Figure 5.11a illustrates the photopeak of a simulation of a nuclear line emission source of 600 keV. Fitting the data, provides a σ-value describing the spread in the photopeak spectrum, as described in Figure 2.6 in this thesis. In the analysis, the energy window for nuclear line sources is $\Delta E = \pm 2\sigma$. For continuum emission sources it is $\Delta E = E$. This means that if the performance is evaluated at 600 keV, a window of 600 keV is chosen around (thus 300-900 keV).

The ARM is evaluated for data with the given energy window applied. An example of an ARM fit is given in Figure 5.11b. The source extraction region is then defined from the FWHM of this ARM by $\pm 3\sigma$.
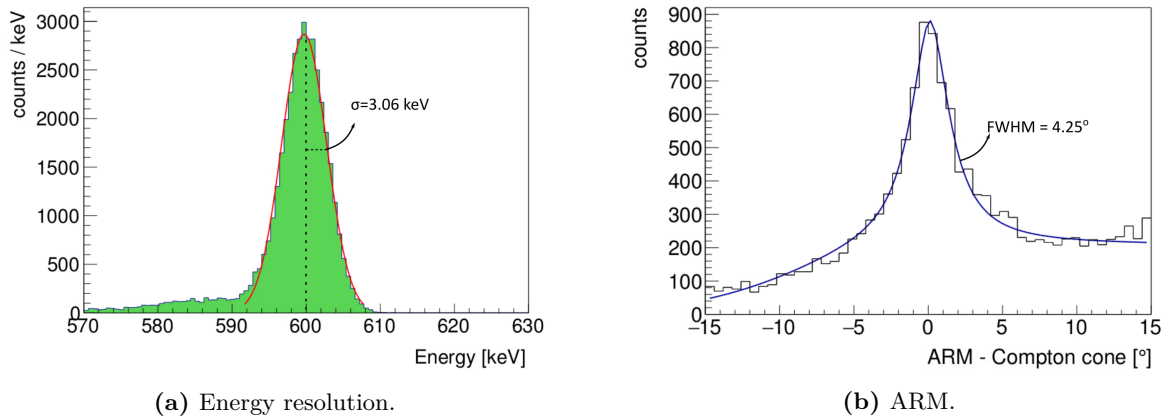

(a) Energy resolution.

(b) ARM.

Figure 5.11: Examples of determining the energy resolution and ARM for a nuclear line emission at 600 keV.

The effective area is calculated for a given energy window and source extraction region by the following equation [12]:

$$A_{eff} = A_{start} \frac{N_{measured}}{N_{started}} \tag{5.1}$$

where $N_{started}$ is the number of photons started in the simulation from an area A_{start} which is large enough to illuminate the entire geometry. $N_{measured}$ is the number of photons which pass all event selections, energy window, and source extraction region specifications.

The sensitivity is calculated using Eq. (2.2) in the paper (Appendix C), evaluated at a specific effective observation time. Here, a simulation of the background alone is included to provide the

number of background photons. The same event selection, energy window, and source extraction region are applied, as used for the effective area calculations.

5.3.4   Results and discussion

In the paper (Appendix C) we investigated the feasibility of operating the 3D CZT drift strip detector in a small Compton camera configuration for space observation. The idea is, that if it is possible to do some minor science with the detector on a small payload, it can prove the capabilities of the detector, and at the same time improve its TRL. In Section 3 of the paper, titled "Payload performance", the basic performance of the instrument is presented, together with the sensitivity and its in-orbit performance.

The effective area, ARM, and efficiency evaluated using simulations of nuclear line sources are presented in Figure 2 in the paper (Appendix C). The instrument ARM is limited by Doppler broadening. This is expected due to the detector material being CZT, as previously described in Section 2.1.2.1. The effective area of the instrument was small, which was not surprising due to the limited number of detectors included in the payload. This of course has a direct effect on the instrument sensitivity, which in general was rather low, in the order of 10^{-4} [ph/cm^2/s]. The small effective area limits the sensitivity of the instrument, however, better background suppression would also increase the sensitivity. Despite the poor sensitivity of the instrument, some limited science goals might still be probable. For in-orbit simulations, the Crab and a selection of six bright GRBs were selected. Section 3.3, titled "Continuum source: The Crab" and Section 3.4, titled "Transient source: Gamma-ray burst", in the paper (Appendix C) presents these results. The Crab could, especially at lower energies, be observed with a reasonable effective observation time. However, the required effective observation time for higher energies rapidly increases. Four out of the six GRBs could be seen in the reconstructed images. The two GRBs with the lowest fluence (flux × duration) were not detected.

In conclusion, the paper presents a feasibility study of using the 3D CZT drift strip detector in a Compton camera configuration together with an active shielding. The study is a pilot-study, and is based on many assumptions, and also some simplifications. First of all, it is assumed that the position and energy information of Compton events within the same detector module can be distinguished as long as they are 1.6 mm apart. In reality, the detector has been operated as a Compton camera [65], but there are still some cases where assigning the energies to the specific position interactions can cause issues. Furthermore, the study assumes a spatial sensitivity of the detector of 0.5 mm at all energies. In reality, this resolution will vary with photon energy. In the study, all passive materials related to the spacecraft are not included. Including passive materials will also have a negative impact on the performance. Furthermore, activation of the instrument has not been taken into account in the analysis. However, as a pilot-study, it does show that it might be feasible to operate the detector on a small Compton camera payload with some limited science goals. In terms of technology demonstration purposes, a small payload like this could be valuable, however, to close the MeV gap, a much larger effective area is necessary.

Future work in terms of this simulation study would be to prepare a more finished geometry, and elevate this study from a feasibility study to a more finished product. As the 3D CZT drift strip technology develops further, limitations related to event selection will become more clear. Furthermore, coupling the detector with other detector types in the Compton camera payload could be interesting. Considering activation background simulations, would also provide a more clear picture of the actual possibilities. Lastly, since the Compton camera includes the ability to measure polarization, as described in Section 2.4, a Minimum Detectable Polarization (MDP) analysis would deem interesting.

6 Conclusion

The sensitivity gap in the MeV domain conceals the answers to scientific questions of astrophysical phenomena within this energy range. What are the physical processes of the energetic environments around compact objects? What are the processes of element formation connected to supernovae and kilonovae? What is the source of the positrons resulting in the 511 keV gamma-ray positron annihilation signature from the Galactic Center region? And many more questions could be outlined here. Every region of light emitted in our Universe, contain a piece of the puzzle. Therefore, closing the gap in sensitivity in the MeV domain is a key factor in understanding our Universe. The inherent difficulty of observing the MeV domain results in strict criteria for future observatories and the detectors they will inhabit.

This thesis is devoted to the further development of the 3D CZT drift strip detector developed at DTU Space. The thesis has contributed to advances within the 3D CZT drift strip detector technology, including development of the detector laboratory setup, software tools and data analysis procedures, model development, characterization and evaluation, and an outlook on the future for the 3D CZT drift strip detector. It was shown that the unique 3D spatial sensitive nature of the detector enables a finer material study, which improves model performance and provides valuable insight in the bulk of the detector material. It was highlighted that the 3D CZT drift strip detector technology can not only benefit the future of space exploration, but a technology transfer can make it valuable on Earth, for example, it is applicable in future breast cancer diagnostic tools. Furthermore, the fine intrinsic spatial resolution and good energy resolution could be maintained, despite a simplification in the detector manufacturing. The detector would be a good candidate for future MeV observatories, for example embedded in a Compton camera payload.

With one of the primary objectives of this PhD study being development, manufacturing, and characterization of new 3D CZT drift strip detectors using advanced detector signal processing and event characterization algorithms, much work was put into laboratory setup, experimental work, and software development. Investigation of signal fluctuations due to material properties and characterization work was published in dedicated articles [4, 5], with successful industrial collaboration on the 3D MBI detector modules. And with an outlook on the future possibilities of the 3D CZT drift strip detector, an in-orbit technology demonstration simulation study was carried out, and the resulting article submitted for review.

Ultimately, technology is a main driver in space exploration enabling new scientific discoveries. This thesis work have brought us closer to a space-ready module. But before the detector can be taken into use on Earth or in space, some technological advances are crucial. A dedicated readout electronic must be realized, lowering the electronic noise and data size of the detector. In this process, the detector model, data analysis tools, and better understanding of the 3D CZT drift strip detector will deem valuable. The 3D CZT drift strip detector technology has shown exciting development throughout the duration of this thesis, and it is now more evident that this technology has a place in future space and Earth applications.

6.1   Future work

The detector TRL must be elevated further, and various aspects of the detector development has potential for future work. In the following, I suggest topics for further advancements of the detector technology.

- **Development of specific readout electronics** with a dedicated ASIC, designed specifically for the 3D CZT drift strip detector is crucial. The development should focus on lowering the electronic noise contribution, while containing the excellent sub-millimeter intrinsic spatial resolution, good spectral resolution, and event characterization and electron drift time determination abilities.

- **Expansion of the position algorithms** to handle the areas where the current position calculation algorithms fall short. This includes edge cases along the z-direction and drift cell boundaries between anodes together with events close to the anode for the x-position. This will increase the sensitive volume of the detector bulk.

- **Full characterization of the final 3D MBI module** will provide the final characterization work in the 3D MBI project. The final 3D MBI module provides a detector volume four times larger than the two previous versions of the 3D CZT drift strip detector. This also requires work on the detector laboratory setup and data analysis tools to include more channel readout.

- **Further detector model development** can take into account diffusion and the spatial volume of the charge clouds. Furthermore, multiple events can be simulated using the detector model. If the detector model is excellent at predicting the detector response, it can deem a valuable tool in future development for the 3D CZT drift strip detector. Using machine learning on synthetic data from the model might improve the data sorting algorithm, position algorithms, and electron drift time.

- **Technology demonstration in space** by including the detector in a Compton camera payload on a CubeSat would increase the detector TRL, and make it a valid detector option for future MeV observatories.

A   Paper 1

Carrier Lifetime and Mobility Characterization using the DTU 3D CZT Drift Strip Detector

S. Howalt Owe, I. Kuvvetli, and C. Budtz-Jørgensen

Abstract—At DTU Space a 3D CdZnTe (CZT) drift strip detector prototype of size 20mm x 4.7mm x 20mm has been developed. It has demonstrated excellent submillimeter position resolution (< 0.5mm), and energy resolution ($< 1.6\%$) at 661.6keV using pulse shape signal processing. Signal formation on each of the 26 electrode readouts uses bi-polar Charge Sensitive Pre-amplifiers. The output is sampled using high speed digitizers; providing us with the full pulse shapes generated by each interaction in the detector. In order to optimize and understand the detector performance, a model of the 3D CZT drift strip detector has been developed using COMSOL Multiphysics® and Python. It simulates the 26 pulse shapes generated by an interaction, and provides an output similar to that of the real detector setup. In order to create a trustworthy model, the material properties of the detector must be well understood. The generated pulse shapes are greatly affected by the electron mobility (μ_e) and lifetime (τ_e) of the detector material. Therefore, 3D maps of μ_e and τ_e have been calculated as look-up tables for the model, utilizing the high resolution 3D interaction position and energy information provided by the 3D CZT drift strip detector. In conclusion, the model performance is compared to real event data. We show that the model performance is greatly improved using the newly calculated 3D maps compared to the uniform material properties provided by the crystal manufacturer.

Index Terms—3D CZT detectors, CZT Drift Strip Detectors, Digitized pulse shape analysis, Carrier lifetime and mobility

I. INTRODUCTION

Pulse shape formation in a semiconductor detector is greatly affected by the electrode geometry (weighting potential effect), and the charge carrier mobility (μ) and lifetime (τ) of the detector material. To build a reliable model for simulation of the pulse shape formation within a semiconductor detector, the detector material properties must be well understood. A method for determining the electron mobility (μ_e) and lifetime (τ_e) has previously been described [1] [2], estimating uniform material properties of the detector. In this paper, we investigate how to use these methods to create a 3D map of μ_e and τ_e within the 3D CdZnTe (CZT) drift strip detector utilizing its 3D position and spectroscopic capabilities. The material non-uniformities will thereby be taken into account. The 3D maps are then implemented as look-up tables in the 3D CZT detector model, and its impact on the model performance investigated.

High resolution 3D CZT drift strip detectors are showing promising results within both medical and astrophysical applications [3] [4] [5]. The CZT drift strip detector principle,

S. Howalt Owe is a PhD student at the Technical University of Denmark, Kgs. Lyngby, DK-2800, Denmark (e-mail: shoowe@space.dtu.dk).

I. Kuvvetli is a senior scientist at the Technical University of Denmark, Kgs. Lyngby, DK-2800, Denmark (e-mail: irfan@space.dtu.dk).

C. Budtz-Jørgensen is a senior scientist emeritus at the Technical University of Denmark, Kgs. Lyngby, DK-2800, Denmark (e-mail: carl@space.dtu.dk).

[6] [7], screens the anodes from the poor hole movement in CZT, such that the detector performance mainly depend on the electron charge transport characteristics. The high-resolution, 3D position sensitive, CZT detector prototype developed at DTU Space, is of size 20mm $\times$ 4.7mm $\times$ 20mm. The CZT crystal was manufactured by REDLEN, and details on the detector prototype fabrication can be found in [8]. On one plane of the detector 10 cathodes are deposited, and on the other side 12 anodes and 37 drift strips are deposited perpendicular to the cathodes. The drift strips are sectioned into four readouts, resulting in four drift strip sections. At standard operation the anodes are grounded, the cathodes are biased at -350V, and the drift strips are biased at -120V (central drift strips are held at a bias of 2/3 of -120V and the two adjacent drift strips are held at 1/3 of -120V, such that electrons are drifted towards collection at the anode). See Fig. 1 for an electrical diagram of the 3D CZT detector.

The readout technique and the developed interaction position reconstruction algorithms have resulted in excellent 3D position, and energy resolution for high energy photon interactions [9]. The system has currently been tested at 661.6keV using a ^{137}Cs source. It demonstrated a position resolution of 0.5mm $\times$ 0.4mm $\times$ 0.5mm in the x-, y-, and z-direction respectively, and an energy resolution of $<1.6\%$ [5]; the current setup suffers from high electronic noise (5-7keV FWHM) and is therefore the limiting factor to this resolution. The high-speed digitizers enable sampling of the full pulse shape formation of the signal; see Fig. 2 for an example. The pulse shapes of the given interaction contain substantial information about the interaction, for example, 3D interaction position, energy deposition, electron drift time, and interaction type (e.g. photoelectric absorption event, or a Compton interaction event). 3D position information in the detector, in combination with the knowledge of interaction types, makes this detector an excellent candidate for future high energy Compton camera applications [5]. Understanding how the signals are generated within the detector is a key factor for further development and improvements.

To optimize and understand the detector performance, a model of the 3D CZT drift strip detector has been developed using COMSOL Multiphysics® and Python. The 3D CZT detector electrode geometry was implemented in COMSOL in order to calculate the electrostatic conditions of the detector, as input for the charge movement and transport Python script. The detector model can be configured by a set of input parameters, such as sample time, sample length, and start time and initial 3D position of the photon interaction. The detector model calculates the induced signals on all 26 electrodes, and
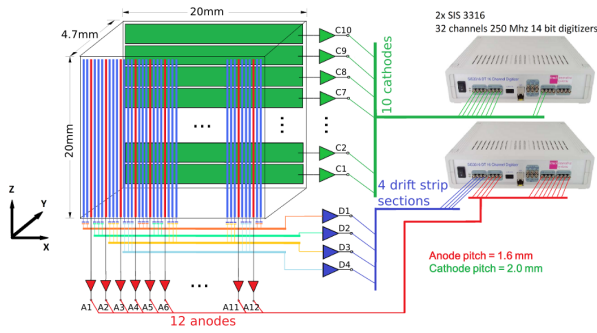
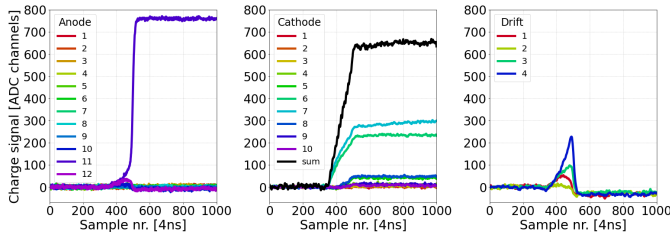Fig. 1. Electrical diagram of the 3D CZT drift strip detector.

Fig. 2. Example of 26 pulse shapes measured by the 3D CZT drift strip detector system. Left: 12 anode signals. Center: 10 cathode signals and the sum of the cathode signals. Right: Four drift strip signals.

returns the 26 generated pulse shapes for the given interaction position. For comparison purpose, the output is provided in a data format similar to the one for the real detector setup using digitizers.

The current model uses uniform material properties for the entire detector volume. Since the pulse shape formation is greatly affected by μ_e and τ_e of the detector material, it is imperative that the values used by the model resembles the ones from the true detector. If not, the simulated pulse shapes and the true pulse shapes are incomparable.

II. MATERIALS AND METHOD

To investigate the μ_e and τ_e parameters throughout the 3D CZT detector volume, three estimations are produced. First, we estimate the product $\mu_e\tau_e$, next we estimate the electron lifetime τ_e, and finally, we use the two estimations to isolate the electron mobility μ_e. For the analysis we utilize the 3D CZT detector data. All single event interactions are extracted, and for each of these events the following information is determined using pulse shape analysis:

1) 3D position of the event in the 3D CZT detector.
2) Deposited energy by the photon in the 3D CZT detector.
3) Drift time of the generated electron charge cloud.

The 3D position information is used to divide the detector volume into a virtual grid of data volumes (i.e. voxels), to each of which a pair of μ_e and τ_e values are associated, utilizing the events occurring within the voxel. In order to do this, the deposited energy and electron drift time is used, extracted from measurements taken at different voltage bias settings, resulting in a change in the electric field strength in between each measurement.

A. Experimental setup

To determine μ_e and τ_e of the detector material, sets of data collected at varying voltage bias (V) between the anodes and cathodes are used. The anodes are grounded and the drift strips and cathodes are biased in a total of six configurations varying the cathode bias from -150V to -400V. For each cathode bias the drift bias was chosen to be a 3rd of the cathode bias, with a maximum bias of -120V, due to electronic noise. See Table I for an overview of the measurement voltage settings. A ^{137}Cs (661.6keV) source was placed, illuminating the entire XZ-plane (anode plane) of the detector, at a distance of 20 cm. For each bias setting a set of 20 hour measurements were taken, resulting in a total of 120 hours of data collection.

TABLE I
CATHODE AND DRIFT VOLTAGE BIAS SETTINGS.

Measurement	Cathode bias [V]	Drift bias [V]
1	-150	-50
2	-200	-66
3	-250	-83
4	-300	-100
5	-350	-120
6	-400	-120

B. Estimating the electric field strength

The change in voltage bias between each measurement is done in order to vary the electric field strength (E) inside the detector. This affects the movement of the electron charge cloud, which will drift quicker towards collection and experience less electron charge trapping as the electric field strength increase. We know the bias voltage values exactly, but how do we then make a proper estimation of the electric field strength within the detector? When it comes to the electron drift path, the 3D CZT drift strip detector can be assumed as a planar detector for most of the detector volume. See Fig. 3, which illustrate the electric field path within one drift cell of the 3D CZT detector simulated using COMSOL. A uniform electric field path is seen throughout most of the detector medium, only close to the anode side ($y < 1$mm) we see this assumption will no longer hold. For this analysis we have chosen to model and estimate the electric field strength and shape by simulation using COMSOL.
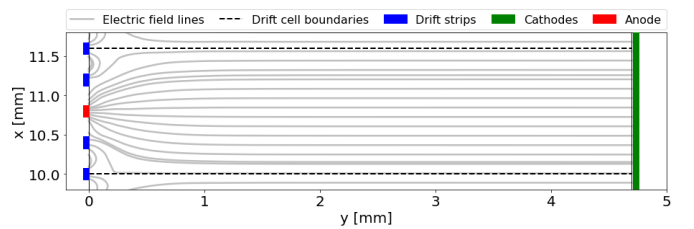

Fig. 3. COMSOL simulation and illustration of the electric field lines zoomed in on a single drift cell in the 3D CZT drift strip detector at a cathode bias voltage of -350V and a drift bias voltage of -120V.

C. Estimation of the $\mu_e\tau_e$-product

The $\mu_e\tau_e$-product is estimated utilizing the electric field strengths, electron drift distance, and photopeak position using the relation [1],

$$N = N_0 \exp\left(-\frac{y_d}{\mu_e\tau_e E}\right) \quad (1)$$

where N is the number of electrons collected after a drift distance of y_d, E is the electric field strength in the detector, and N_0 is the original number of electron-hole pairs. Consider the two cases where measurements are taken at two different bias voltages between anode and cathode (V_1 and V_2). This will result in two different electric field strengths (E_1 and E_2), and two different measured photopeak amplitudes (N_1 and N_2) as the photopeak amplitudes are proportional to the number of electrons collected at the anode surface. Using this, two expressions of (1) can be used to solve and get rid of N_0 such that [1]

$$\ln\left(\frac{N_1}{N_2}\right) = \frac{y_d}{\mu_e\tau_e}\left(\frac{1}{E_2} - \frac{1}{E_1}\right) \quad (2)$$

where y_d is the electron drift length for data with photopeak amplitudes N_1 and N_2 [1]. Both the measurement of N_1 and N_2 have the same non-linear weighting potential effect on the signals as a function of y_d; as previously described [9]. The ratio of the two signals given in (2) will cancel out this effect.

The six measurements (Table I) are then used to calculate five points. N_1 is described by the data measured at biases from measurement number 1 to 5, and N_2 is described by the data measured at the highest bias (measurement 6). Plotting $\ln(N_1/N_2)$ as a function of $(1/E_2 - 1/E_1)$ and fitting a linear regression model, results in the slope,

$$\alpha = \frac{y_d}{\mu_e\tau_e} \quad (3)$$

and knowing the electron drift length y_d, we can estimate the $\mu_e\tau_e$-product. For an estimation of the error in the calculated $\mu_e\tau_e$-product error propagation is applied to (2). The electric field strengths are assumed to be known accurately, which results in the uncertainty in N_1, N_2, and y_d contributing to the error.

D. Estimation of the electron lifetime τ_e

τ_e is estimated utilizing electron drift times together with photopeak positions measured at different voltage bias between anode and cathode. Given the decay of the free-carrier concentration as a function of time, and assuming that the collected charge is proportional to the amplitude of the photopeak position, we have for two measurements at different bias voltage settings [2]

$$N_1 = N_0 \exp\left(-\frac{t_{d1}}{\tau_e}\right) \quad (4)$$

$$N_2 = N_0 \exp\left(-\frac{t_{d2}}{\tau_e}\right) \quad (5)$$

where t_{d1} is the electron drift time from the initial interaction position at the first bias setting, and t_{d2} is the electron drift time from the initial interaction position at the second bias setting. Solving using (4) and (5), we can again cancel out the original number of electron-hole pairs N_0,

$$\ln\left(\frac{N_1}{N_2}\right) = \frac{1}{\tau_e}\left(t_{d2} - t_{d1}\right). \quad (6)$$

The six measurements (Table I) are then used to calculate five points. N_1 and t_{d1} is described by the data measured at biases from measurement number 1 to 5, and N_2 and t_{d2} is described by the data measured at the highest bias (measurement 6). Plotting $\ln(N_1/N_2)$ as a function of $(t_{d2} - t_{d1})$ and fitting a linear regression model, results in the slope,

$$\alpha = \frac{1}{\tau_e} \quad (7)$$

allowing us to estimate the electron lifetime τ_e. For an estimation of the error in the calculated τ_e, error propagation is applied to (6). The error calculation will be affected by the uncertainties of the estimated energies and electron drift times, N_1, N_2, t_{d1}, and t_{d2}. The uncertainty of the estimated energies are mostly affected by the energy resolution of the detector, where the uncertainties of the electron drift times are strongly affected by the voxel size. Especially close to drift cell boundaries, electron drift times will vary more, compared to directly above the anode.

E. Estimation of the electron mobility μ_e

μ_e is lastly estimated from the determined values of $\mu_e\tau_e$ and τ_e,

$$\mu_e = \frac{\mu_e\tau_e}{\tau_e}. \quad (8)$$

The error estimation is again done using error propagation applied to (8) with the estimated errors in $\mu_e\tau_e$ and τ_e contributing.

III. DATA PREPARATION

For each of the six bias setting measurements, the 26 pulse shapes for each photon interaction were processed, with only single trigger event data considered. This resulted in a dataset containing the following information for each photon interaction: 3D position, 26 ADC pulse heights, and electron drift time.

A. Position determination

The position determination algorithms will be briefly described in this section. Further information on the positioning algorithms can be found in [5] and [9].

1) x-position: The x-position in the 3D CZT detector is along the direction of the anodes; see Fig. 1. For the x-position determination we utilize the peak value of the two adjacent inverted drift strip current signals to the triggered anode, denoted A_{DL} and A_{DR}. Coupled with this information, the triggered anode number x_{trig} is used to determine the x-position,

$$x = 0.4 + \left[x_{trig} + F \cdot \frac{A_{DR} - A_{DL}}{A_{DR} + A_{DL}}\right] \cdot P_{an} - \frac{P_{an}}{2}, \quad (9)$$

where the constant 0.4 is the initial distance from the edge to the first electrode, F is an adjustable factor for calibration of the x-scale, currently set to 0.69, and P_{an} is the anode pitch of 1.6mm.

2) y-position: The y-position of the detector describes the depth of the interaction between the anode side, and cathode side of the detector, see Fig. 1. When determining the y-position, the cathode pulse heights, C_n, are summed and divided by the pulse height of the triggered anode A_m. This returns the depth parameter of the detector, which is then calculated in units of detector thickness, D,

$$y = \frac{\sum_{n=1}^{10} C_n}{A_m} \cdot D. \tag{10}$$

3) z-position: The z-position is determined utilizing the 10 cathode amplitudes in a center of gravity of cathode strip calculation. Utilizing the cathode pulse heights, C_n, and the cathode pitch, P_{ca}, of 2mm, the z-position is given by,

$$z = \frac{\sum_{n=1}^{10} n \cdot C_n}{\sum_{n=1}^{10} C_n} \cdot P_{ca}. \tag{11}$$

B. Pulse height determination

All 26 pulse shapes are adjusted to have the same baseline (see Fig. 2). The cathode and anode pulse heights are simply determined by subtracting the average value of the first 150 samples from the average value of the last 150 samples. The drift strip signals are bi-polar, and therefore the pulse heights are not extracted. However, the peak position of each derivative of the pulse shape (current profile) is extracted, and used when determining the x-position.

C. Drift time determination

The electron drift time of each event is determined by the sample time of the beginning, t_0, and the end, t_1, of the event. To determine these, the sum of the cathode signal pulse shapes is utilized. The cathode sum is obtained by summing the 10 cathode pulse shapes after readout. Fig. 4 shows an example of the summed cathode signal of an arbitrary event. The cathodes will see the electron cloud movement at the instant the charge cloud starts to drift. This results in an increase in the induced signal. The pulse shape will continue increasing until the electron charge cloud is collected, where the pulse shape once again will flatten. The beginning and end of the event can then be determined by applying a linear fit to the slope of the signal. The point where the linear fit intersects with the baseline, is chosen as the beginning of the event, t_0. The point where the linear fit intersects with the point where the cathode signal sum flattens is chosen as the end of the event t_1. The two time values, t_0 and t_1, can then be used to calculate the drift time, t_d. The unit of these values are the sample time 4ns. For events close to the anode side, the created cathode pulses will be characterized by small pulse heights. This can result in the determined drift time being distorted. Therefore, this method is not covering events close to the anode side.
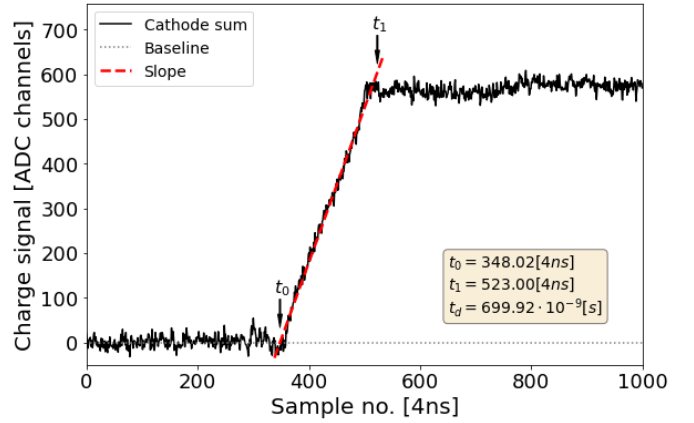

Fig. 4. Illustration of the procedure of utilizing the sum of cathode pulse shapes to determine the start time, t_0, and end time, t_1, of the event. The drift time in seconds can then be calculated by $t_d = 4 \cdot (t_1 - t_0) \cdot 10^{-9}$.

D. The dataset

For each measurement of all voltage bias settings, the pulse heights, 3D positions, and drift times, are extracted using the methods described in the previous sections. This resulted in six data sets; one for each voltage bias setting. Fig. 5 shows 2D-histograms of the XZ-plane and the XY-plane of the 3D position information for the measurement at cathode voltage bias -350V and drift voltage bias of -120V. The XZ-plane shows no events for $z < 2$mm and $z > 18$mm, due to more severe edge effect on the signals. Furthermore, we do see areas where there are fewer or no events around anodes 5 (A5), 6 (A6), 11 (A11), and 12 (A12) for $z < 5.0$mm, as encountered earlier [5]. Investigating the XY-plane we see the same artefacts as earlier encountered [5], [9], with anode 1 (A1) and 12 (A12) showing clear edge effects and the x-position algorithm not covering events with $y < 1$mm.

Investigating the 2D-histograms of the XY- and XZ-plane, a subset region was chosen for this analysis. The subset considered in this analysis is made only of anodes 2-11 with the y-position limits 2.0mm $\leq y \leq 4.0$mm, and the z-position limits 13.0mm $\leq z \leq 15.0$mm. Furthermore, along the x-direction, only data within 0.2mm from each drift cell boundary is considered. The white highlighted areas in Fig. 5 indicate the data subset used for this analysis. The subvolume is then divided into virtual volumes, each of size (dx, dy, dz) = (0.4mm, 0.2mm, 1.0mm). The size is mainly limited by statistics. If we wish to make the volumes even smaller, more data must be collected. However, for the aim of the current analysis this volume size is sufficient. We have chosen to minimize dy since we wish to determine the drift time as precisely as possible. Table II shows an overview of data division boundaries. The analysis can be expanded to include the entire detector volume at a later time.

IV. DATA ANALYSIS

A. Determination of pulse heights and drift time

Each data set (Table I), all followed the same data analysis procedure, described in Section III. Using the 3D position
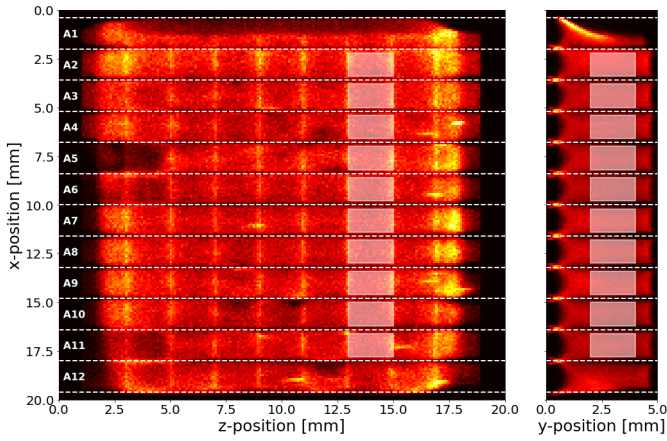
Fig. 5. 2D-histograms displaying the calculated 3D positions for the measurement taken with a cathode bias of -350V and a drift bias of -120V. White dashed lines indicates drift cell boundaries. Anode numbers are defined within each drift cell. The white highlighted areas indicate the chosen data subset of the detector volume.

TABLE II
OVERVIEW OF THE 3D DATA DIVISION BOUNDARIES

Direction	Number of slices	Slice thickness [mm]	Minimum value [mm]	Maximum value [mm]
x (anode 2)			2.2	3.4
x (anode 3)			3.8	5.0
x (anode 4)			5.4	6.6
x (anode 5)			7.0	8.2
x (anode 6)			8.6	9.8
x (anode 7)	3	0.4	10.2	11.4
x (anode 8)			11.8	13.0
x (anode 9)			13.4	14.6
x (anode 10)			15.0	16.2
x (anode 11)			16.6	17.8
y	10	0.2	2.0	4.0
z	2	1.0	13.0	15.0

information, each data set was divided into the virtual volumes described by Table II. To calculate μ_e and τ_e following the methods described in Section II, it is essential to determine a pulse height, drift time, and electron drift distance representing each volume element (or voxel). Therefore, for each voxel, a histogram of the photopeak and electron drift time distribution was plotted, and fitted with a Gaussian distribution. The peak position of the fit was chosen to represent the pulseheight position and electron drift time for the volume. Fig. 6 shows an example of this fitting procedure. Here we see data collected by anode number 2, for the cathode voltage bias of -350V, for y-slice number 4, z-slice number 1, and all three x-slices.

B. Estimation of the electron drift distance

The electron drift distance, y_d, is used to determine the $\mu_e\tau_e$-product as stated in (2). For a planar detector, the electron drift distance can be determined as the interaction depth (y-position) in the detector, since the drift path is perpendicular to the anode. However, the geometry of the 3D CZT drift strip detector results in the electron drift path bending towards the anodes close to collection; as illustrated in Fig. 3. Therefore, the electron drift distance is only comparable to the y-position for interactions occurring directly above the anode. An overall
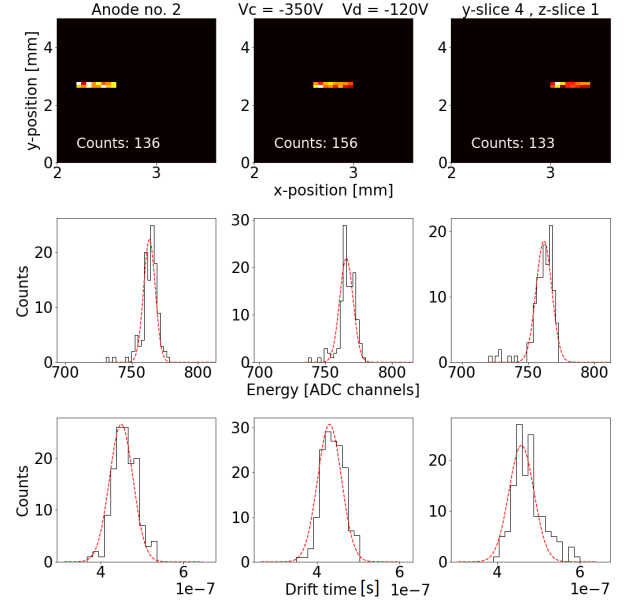

Fig. 6. 2D-position histograms, and Gaussian fit of photopeaks and drift times for three voxels in drift cell number 2, for the measurement settings: Cathode bias -350V and drift bias -120V.

estimation of the drift distance for each voxel must therefore be determined, since the volumes closer to the drift cell boundary will have a longer drift path. This was done by investigating data from anode number 8 at a cathode bias of -350V and drift bias of -120V. Data along the entire z-direction ($0\,\text{mm} < z < 20\,\text{mm}$) and a 0.2mm slice along the y-direction ($3.8\,\text{mm} < y < 4.0\,\text{mm}$) was used. Along the x-direction ($11.8\,\text{mm} < x < 13.0\,\text{mm}$) the data was divided into 11 voxels. For each voxel, the electron drift time was determined. This resulted in 11 values for the electron drift time, where the central value is that of the volume directly above the anode. The drift distance of this volume is assumed to be the central y-position of 3.9mm. Knowing both drift distance and time, using the central voxel, the electron drift velocity was determined to be

$$v_e = \frac{y_d}{t_d} = 5.94 \cdot 10^6\,\text{mm/s}. \qquad (12)$$

In conjunction with the electron drift velocity, the drift distance of the remaining 10 voxels was estimated using the electron drift time information. In Fig. 7, the resulting difference in drift distance, compared to the central data slice, is shown along with the x-slice boundaries of the material analysis; also defined in Table II. As expected, the interactions that occur closer to the drift cell boundary, will experience a longer drift distance. Values approaching the drift cell boundaries (0.6mm from the drift cell center along the x-direction), will drift a distance of around 0.4mm longer than that of the interactions directly above the anode. The central voxel do not have a big variability in electron drift distance. However, events within the boundary volumes vary close to 0.4mm in electron drift distance. Since we use the drift distance to determine the $\mu_e\tau_e$-product in (2), this does impose an uncertainty introduced from the drift distance, especially for the boundary volumes.

The drift distance representing the boundary volumes was then added a distance of 0.15mm (mean difference) compared to the central volume.
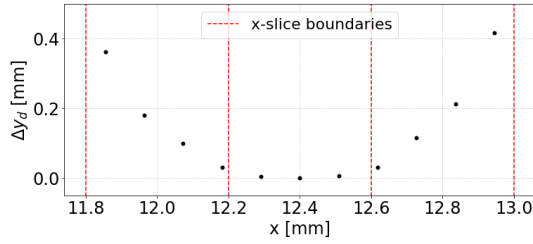

Fig. 7. Difference in drift distances between the an event directly above the anode ($x = 12.4$mm) and events closer to the drift cell boundaries. Red dashed lines: Boundaries for the voxels used for the analysis.

Fig. 8. $\mu_e\tau_e$-map of the chosen detector subvolume. The mean estimated error of the calculated $\mu_e\tau_e$-values is $\sim 10\%$. White dashed lines: Drift cell boundaries.

V. RESULTS

A total of three 3D maps was generated for the chosen detector volume. A map for the $\mu_e\tau_e$-product, τ_e, and μ_e. The calculated maps were compared to the original values provided by the manufacturer of the detector crystal given in Table III. In the following sections, the calculated 3D maps will be presented together with a comparison to the manufacturer values.

B. Estimation of the electron lifetime τ_e

The τ_e-map was calculated using the method described in Section II-D, also done for each of the voxels in our 3D map grid. In Fig. 9 the calculated τ_e-map of the chosen detector subvolume is shown. We identify similar tendencies as for what we observed in the $\mu_e\tau_e$-map. Using error propagation, the mean estimated error of the calculated τ_e-map was determined to be $\sim 5\%$. Compared to the manufacturer value given in Table III, we see that we are in the same order of magnitude, however with a non-uniformity in the detector material. We note that the variation in τ_e is similar to that of $\mu_e\tau_e$, and must therefore also be responsible for the variation in $\mu_e\tau_e$.

TABLE III
MATERIAL PROPERTIES OF THE DETECTOR CZT CRYSTAL.

	MANUFACTURER		
	$\mu\tau$[cm^2/V]	τ[s]	μ[cm^2/Vs]
Electron	1.5e-2	3.0e-5	500
Hole	0.0006e-2	3.0e-7	20
	3D MAP AVERAGE		
	$\mu\tau$[cm^2/V]	τ[s]	μ[cm^2/Vs]
Electron	2.9e-2 $\pm$ 0.3e-2	3.2e-5 $\pm$ 1.6e-6	909.7 $\pm$ 91
Hole	—	—	—

A. Estimation of the $\mu_e\tau_e$-product

The $\mu_e\tau_e$-map was calculated using the method described in Section II-C for each of the voxels in our 3D map grid. In Fig. 8 the resulting calculated $\mu_e\tau_e$-map of the chosen detector subvolume is shown. The 3D-map is illustrated in 2D by showing each of the two slices along the z-direction alone. The upper map is the first z-slice and the lower the second. Using error propagation the mean estimated error of the calculated $\mu_e\tau_e$-map was determined to be $\sim 10\%$. We do see a variation in the $\mu_e\tau_e$-product throughout the detector material, with almost a factor of 3, especially along the x-direction. Thus, we do see variation significantly larger than the estimated error. The variation is of course not provided by the manufacturer, since the manufacturer values assume uniform material properties. Moreover, the presented results are for large parts of the detector significantly larger than the nominal values given in Table III.
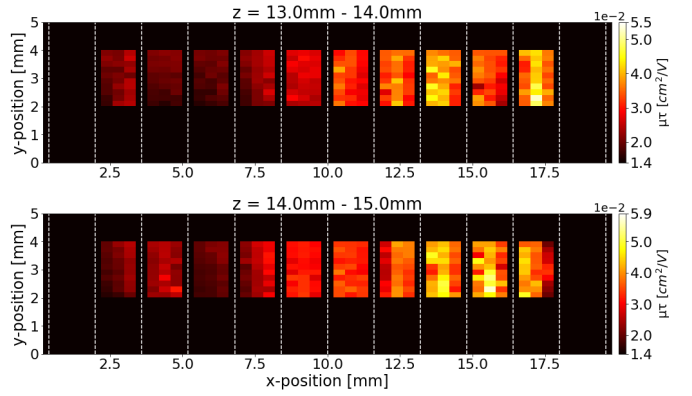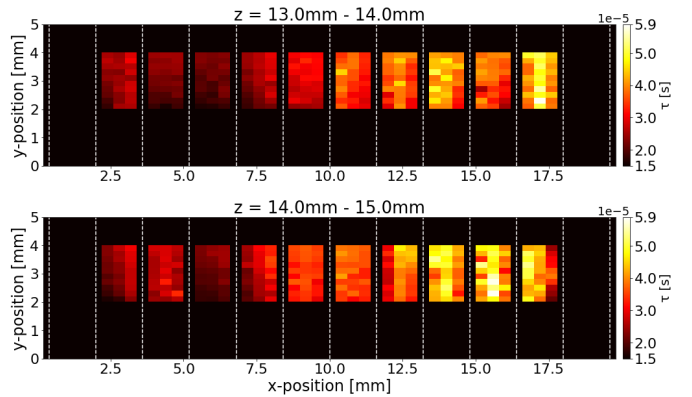

Fig. 9. τ_e-map of the chosen detector subvolume. The mean estimated error of the calculated τ_e-values is $\sim 5\%$. White dashed lines: Drift cell boundaries.

C. Estimation of the electron mobility μ_e

μ_e is estimated using the calculated values for $\mu_e\tau_e$ and τ_e, as described in Section II-E. In Fig. 10 the calculated μ_e-map of the chosen detector subvolume is shown. Using error propagation the mean estimated error of the calculated μ_e-map was determined to be $\sim 10\%$. This error is large compared to the variances we see in the map. Therefore, we cannot draw any conclusions on the material variability, however we can state that the average estimated electron mobility is almost a factor of two larger than the nominal value provided by

the manufacturer; see Table III. This method estimates the electrons to have a much better mobility than the uniform manufacturer estimation provides.
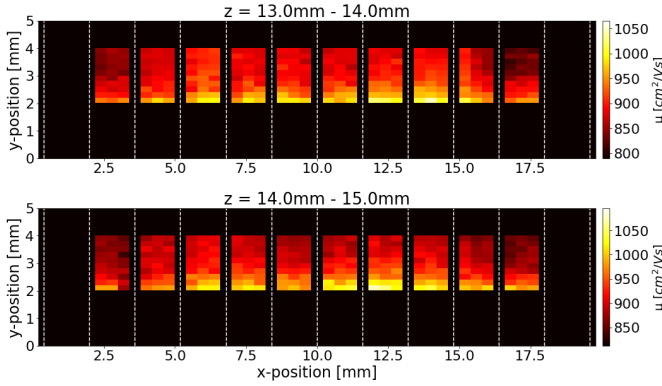

Fig. 10. μ_e-map of the chosen detector subvolume. The mean estimated error of the calculated μ_e-values is $\sim 10\%$. White dashed lines: Drift cell boundaries.

D. Implementation in the 3D CZT detector model

The next step is to investigate how the newly generated 3D maps affect the performance of the 3D CZT detector model. In this article, one example of the comparison between a real event and the detector model performance will be presented. Fig. 11 shows the measured pulse shapes for a real event in the 3D CZT detector. To simulate this event, we calculate the x-, y-, and z-position alongside the start time of the event. This is then used as input for the 3D CZT detector model. This will of course carry the error of the calculation in position and start time into the modelled data, however, this should only introduce small disagreements between model and data. The model then extracts the μ_e and τ_e values representing the voxel from which the position of the event originates, from the calculated 3D maps, subsequently, the model was run; simulating the event. The event was simulated using two sets of μ_e- and τ_e-values. The ones provided by the manufacturer, and the ones from the calculated 3D maps. For the hole material properties, the hole mobility (μ_h) and lifetime (τ_h) values used are the ones provided by the manufacturer in Table III, assuming uniform values. Fig. 12 shows a comparison of the real data and the two models, including the main triggered electrodes. Inspecting the three anode signals (Fig. 12(a-c)), we conclude that the model using the newly calculated 3D maps improves the modelled signal greatly, compared to the model using the uniform value provided by the manufacturer. Consequently, the modelled transient signals on the neighbouring anodes are improved. Investigating the cathode signals (Fig. 12(d-f)), we clearly observe that the model using the 3D maps, simulate the slope of the cathode signal much better than the manufacturer values. We do see however, that the real data have an increase in the cathode signal after electron collection, that does not occur in the model. This indicates that the hole mobility and lifetime is better than what was provided by the manufacturer. This invites for a future characterization of the hole mobility and lifetime in the 3D CZT drift strip detector.

Finally, comparing the drift signals (Fig. 12(g-j)), once again we see that the signals are represented much better by the model using the 3D maps than the one using the uniform manufacturer values.

We clearly see that the model demonstrates a great improvement in prediction when applying the calculated 3D maps compared to using a uniform assumption with manufacturer provided values. Currently the discrete values for a given voxel extracted from the 3D maps, are used as model input for all interaction positions within that voxel. However, in reality the $\mu_e\tau_e$, τ_e, and μ_e values should vary gradually throughout the material. Interpolation of the 3D maps could be implemented in the future.
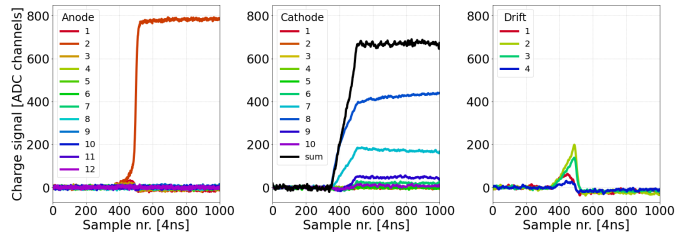

Fig. 11. Anode, cathode, and drift pulse shapes of a real event. $x = 2.66$mm, $y = 3.95$mm, $z = 14.52$mm, and $t_0 = 352.6$ samples.

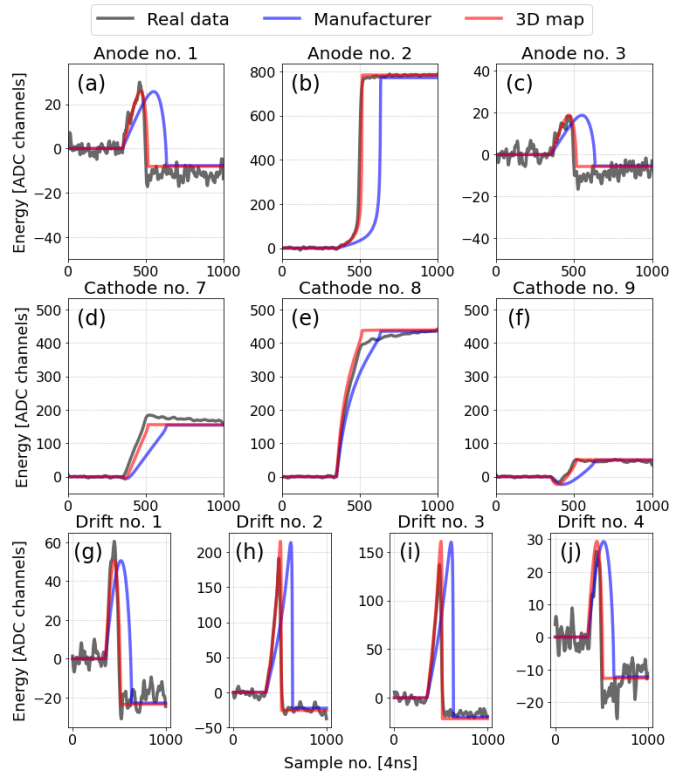Fig. 12. Comparison between pulse shapes of a real event, and pulse shapes simulated by the model using manufacturer provided values of μ_e and τ_e, and the model using the μ_e and τ_e values extracted from the calculated 3D maps.

VI. Conclusion

Utilizing the 3D position and spectroscopic capabilities of the 3D CZT drift strip detector, a material analysis was performed, to create 3D maps of the detector material electron mobility and lifetime. This resulted in three 3D maps for a subsection of the detector volume; a map of the $\mu_e\tau_e$-product, a map of τ_e, and finally a map of μ_e. The 3D maps were tested, simulating real data events, using the 3D CZT detector model first using the uniform μ_e and τ_e values provided by the manufacturer, and second simulating the event using the newly calculated 3D maps. Comparing modelled pulse shapes with the pulse shapes of the real event, the model demonstrated a great improvement when applying the calculated 3D maps. It also did show that the current assumptions of the hole-material properties (manufacturer provided) did not represent the detector material. We can therefore conclude that the newly calculated 3D maps have greatly improved the 3D CZT detector model performance, to produce more reliable predictions. Not only will these 3D maps provide better possibilities for data correction in the 3D CZT drift strip detector; a model that correctly simulates the pulse shapes makes it possible to generate training data for artificial neural networks.

References

[1] Z. He, F. Knoll and D. K. Wehe, "Direct measurement of product of the electron mobility and mean free drift time of CdZnTe semiconductors using position sensitive single plarity charge sensing detectors," Journal of Applied Physics 84, 5566, 1998.

[2] A. E. Bolotnikov, G. S. Camarda, E. Chen, R. Gul, V. Dedic, G. De Geronimo, , J. Fried, A. Hossain, J. M. MacKenzie, L. Ocampo, P. Sellin, S. Taherion, E. Vernon, G. Yang, U. El-Hanany, and R. B. James, "Use of the drift-time method to measure the electron lifetime in long-drift-length CdZnTe detectors," Journal of Applied Physics 120, 104507, 2016.

[3] L. Abbene, G. Gerardi, F. Principato, A. Buttacavoli, S. Altieri, N. Protti, E. Tomarchio, S. Del Sordo, N. Auricchio, M. Bettelli, N. Sarzi Amadé, S. Zanettini, A. Zappettinig, and E. Carolif, "Recent advances in the development of high-resolution 3D cadmium–zinc–telluride drift strip detectors," Journal of Synchrotron Radiation, 27, pp. 1564-1576, 2020.

[4] S. Abbaszadeh, Y. Gu, P. D. Reynolds, and C. S. Levin, "Characterization of a sub-assembly of 3D position sensitive cadmium zinc telluride detectors and electronics from a sub-millimeter resolution PET system," Phys. Med. Biol. 61, 6733–6753, 2016

[5] S. Howalt Owe, I. Kuvvetli and C. Budtz-Jørgensen, "Evaluation of a Compton camera concept using the 3D CdZnTe drift strip detectors," Journal of Instrumentation, 14(01) C01020, 2019.

[6] M. A. J. Van Pamelen and C. Budtz-Jørgensen, "Novel electrode geometry to improve performance of CdZnTe detectors," Nuclear Instruments and Methods in Physics Researchs Section A: Accelerators, Spectrometers, Detectors and Associated Equipment. Elsevier 403, 2-3, pp. 390-398, 1998.

[7] M. A. J. Van Pamelen and C. Budtz-Jørgensen, "CdZnTe drift detector with correction for hole trapping," Nuclear Instruments and Methods in Physics Research Section A: Accelerators, Spectrometers, Detectors and Associated Equipment 411.1 pp. 197-200, 1998.

[8] I. Kuvvetli et al., "A 3D CZT high resolution detector for x- and gamma-ray astronomy," High Energy, Optical, and Infrared Detectors for Astronomy VI. SPIE Astronomical Telescopes + Instrumentation, Montréal, Quebec, Canada. 2014, pp. 91540X.

[9] C. Budtz-Jørgensen and I. Kuvvetli, "New Position Algorithms for the 3-D CZT Drift Detector," IEEE Transactions on Nuclear Science, 64.6, pp. 1611-1618, April 2017.

B   Paper 2

Evaluation of CZT Drift Strip Detectors for use in 3D Molecular Breast Imaging

S. R. H. Owe, I. Kuvvetli, A. Cherlin, B. Harris, H. Tomita, I. Baistow, D. Tcherniak, and C. Budtz-Jørgensen.

Abstract—X-ray mammography is a widely used technique for breast cancer screening. However, the technique is imprecise when it comes to radiographically dense breast tissue, and therefore a supplemental screening technique, such as Molecular Breast Imaging (MBI), could increase the cancer detection rate. Emerging technologies within MBI require excellent detector performance, preferably with a sub-millimetre intrinsic spatial resolution. A collaboration between Kromek and DTU Space aims to advance the DTU Space developed 3D CdZnTe (CZT) drift strip technology, for application in new emerging MBI systems. This collaboration has resulted in 10 compact 3D MBI test modules with the goal of producing high-performance and high yield detectors. In this article, we present overall excellent detector performance, sub-millimetre position resolution at both 122 keV and 661.6 keV, and good energy resolution for the applied electrode deposition and contact optimisation. Although the current experimental setup and results suffers from high electronic noise (using discrete NIM standard charge sensitive pre-amplifiers), we conclude that the measured spatial and spectral performance fulfill the expected requirements for the modules, with room for improvement, especially within limiting electronic noise. The detector test modules indicate a promising future for the 3D CZT drift strip technology within future emerging MBI systems.

Index Terms—3D CZT detectors, CZT Drift Strip Detectors, Digitized pulse-shape analysis, High-energy astrophysics, Molecular breast imaging.

I. Introduction

MOLECULAR Breast Imaging (MBI) is a promising nuclear medicine technique for the detection of breast cancer, especially given the improvement in gamma-ray detector technology in the recent years. The most common modality currently used for breast imaging is mammography, which is a low-energy (typically around 30 keV) x-ray breast imaging technique. The breast is compressed between a support plate containing detectors or a film and a paddle, with the x-ray source located above it. A typical mammography scan is comprised of two images taken for each breast, one in head-to-foot direction and one in an angled side view. The low energy of the x-rays is necessary to produce enough contrast difference between the healthy tissue and the tumour.

However, sometimes the healthy breast tissue can contain denser fibroglandular tissue which has the radiographic density similar to that of a tumour, thus masking it and making the tumour detection very difficult especially at early stages [1]. There is a number of alternative imaging techniques which have been shown to provide better results for screening the breasts with dense tissue. A comprehensive overview of those techniques can be found for example in [2] or [3].

Molecular breast imaging is a type of nuclear imaging where the breast is slightly compressed between a pair of gamma cameras made of semiconductor or scintillator detectors. The breast positioning is similar to mammography. MBI utilises ^{99m}Tc sestamibi radioactive tracer which is injected intravenously. The tracer is taken up by metabolically active cells, such as in breast cancer tumours. It emits 140 keV photons which is high enough energy to make the MBI not sensitive to the variations in the breast tissue density thus making it a good candidate for supplemental screening [4]. Mayo clinic's clinical trials have shown that cancer detection rate in women with radiographically dense breast tissue for MBI combined with mammography is 12.0 per 1000 screened versus 3.2 for mammography alone. Furthermore, the sensitivity for the combination was 91% versus 24% for mammography only, and specificity was 83% versus 89% correspondingly [5]. The barriers for the widespread adoption of the MBI technique are its higher patient dose ($\sim$ 1-2.5 mSv versus $\sim$ 0.5 mSv in mammography), and longer imaging time of approximately 40 minutes [6] versus 10 minutes or less in mammography [2] for a typical 4-views' scan.

A collaboration between Kromek and University College London (UCL) has recently suggested an innovative concept for a stationary tomographic low-dose MBI (LD-MBI) system (patent pending), which makes use of high resolution 3D position sensitive CdZnTe (CZT) detectors. This has led to a collaboration between DTU Space and Kromek to develop novel 3D CZT drift strip detectors for future MBI systems.

In this paper, we will present the design and performance of the 10 3D MBI test modules, and relate the performance to future final 3D CZT drift strip detector modules for specific Kromek designed and optimised MBI systems.

A. A stationary tomographic system for MBI

Dedicated MBI cameras using a pair of planar detector arrays have been used for some time [7]. Current MBI systems are usually based on pixelated CZT detectors, as the older scintillator-based cameras were able to provide a moderate increase in sensitivity but at cost of a much higher patient

dose [8]. The 3D position sensitivity of CZT detectors is crucial for the full exploitation of their potential in the existing and emerging MBI technologies. For example, the stationary tomographic low-dose MBI system which is being developed by Kromek and UCL utilises densely packed multi-pinhole collimators to achieve a sufficient angular sampling necessary for tomographic image reconstruction without motion [9]. The large number of pinholes leads to significant multiplexing between the acquired projections through neighbouring pinholes, which creates artefacts in the reconstructed image. Proprietary image reconstruction algorithms performing de-multiplexing of the projections make use of the depth-of-interaction capabilities of CZT detectors to reduce the adverse effects of the artefacts [10], [11]. The current results suggest that the system can provide improved tumour detectability and 3D localisation at the patient dose comparable to an average mammogram scan at a reduced scan time.

The current simulations are based on a pixelated CZT detector with intrinsic spatial resolution of 1 mm in 3D. The intrinsic lateral position resolution of the detector affects the spatial resolution of the reconstructed image and thus the minimal detectable tumour size. The intrinsic depth position resolution of the detector is vital for the de-multiplexing method and will strongly affect the screening time and the patient dose, as the resolution determines the maximum degree of multiplexing which the new image reconstruction can cope with. Higher degree of multiplexing means using more pinholes with wider openings, which results in collecting more photons per unit of the injected dose. That allows decreasing the dose while maintaining a similar or better image quality and clinical outcome. Therefore, implementing the 3D CZT drift strip technology with sub-millimetre position resolution in 3D will provide significant improvements to the method by reducing the patient dose, screening time, and the minimum size of detectable tumours.

B. The 3D MBI Modules

The 3D CZT drift strip detector technology is developed by DTU Space [12]–[14][1,2], and was initially designed for high-energy X- and gamma-ray astronomy. The electromagnetic emission from astronomical sources in the MeV (X- and gamma-ray) energy band is exceedingly difficult to detect; both due to low fluxes, and the fact that photons may penetrate significant thicknesses of material without interacting. In an astrophysical context, photons in this energy band carry specific and valuable information about gamma-ray lines originating from radioactive nuclei from supernova explosions, or ejected from colliding neutron stars. Gamma-rays from matter-antimatter annihilation, and accreting black holes are further examples of sources exciting the interest in this energy band. To improve sensitivity of observations in this energy range, DTU Space introduced the 3D CZT drift strip detector.

---

[1]Patent – 1: "X-Ray and Gamma-Ray Radiation Detector", IPC No.: G01T1/24. Patent No.: WO2015078902. Jun 04, 2015.

[2]Patent – 2: "Z-position correction method for 3DCZT detectors", (PCT/DK2017/050333).

A number of previous prototypes of this specific drift strip detector technology has been manufactured and thereafter characterised at the DTU Space detector lab using a 661.6 keV (^{137}Cs) collimated beam. Similar for the prototypes were a special electrode deposition method, including growth of a 140 nm thick oxide layer between drift electrodes and the CZT material surface, intended to reduce the total surface leakage current [14]. The experimental result showed 3D position resolution of <0.5 mm FWHM and 1% FWHM energy resolution [15].

The excellent 3D spatial and spectral performance of the detector makes it an excellent candidate for future missions observing the MeV domain; as a focal plane detector, but also operating in a Compton camera [16]. The nature of the 3D CZT drift strip detector now indicates that it could also be a candidate for future MBI systems. A main drawback of the previous prototypes are the introduced oxide layer between drift electrodes and the CZT material [14], since this introduced a complexity to the specific electrode deposition technique. Therefore, one of the main research goals of this paper was to develop, implement, and replace this cumbersome oxide layer deposition with a simple, low cost, effective electrode deposition (using an ohmic contact process), keeping the surface leakage current in the order of nA at -50 V between drift strips and anodes.

The collaboration between Kromek and DTU Space resulted in the design and manufacturing of 10 3D MBI test modules, each based on a CZT crystal of size 2 cm × 2 cm × 0.5 cm, see Fig. 1. Each of the 10 modules can be mounted on a PCB stack, for swift change between detectors and easing the characterisation process. The modules were manufactured in two batches. The first batch contained four modules: Two manufactured with high temperature bonding and two with room temperature bonding. In the second batch, all six modules were manufactured using room temperature bonding. Table I summarises the module bonding options. The letter "B" in the module name identifier is followed by the batch number, and the letter "D" is followed by the detector number in the given batch. Each module consists of a detector crystal bonded to a PCB plugged into the stack of three additional PCBs. This multi-PCB structure was chosen to allow for more agile design adjustments. The upper PCB is the "CZT attachment board". This board acts as a mechanical attachment where the anodes and drift strips are connected to the PCB via bump-bonding, and the cathodes via wire bonding. The second PCB is the "anode biasing board" which configures the drift strips into four readout sections, grounds the anodes, and provides high voltage biasing to the drift strip electrodes. The third PCB is the "cathode biasing board" providing high voltage bias to the cathodes. The bottom PCB is the "digitizer interface board". From this PCB, the stack is connected to the high speed digitizer readout system.

The 3D CZT drift strip detector technology differentiates from the common CZT pixel design by its specific electrode strip design. The layout of the electrode geometry is summarised in Fig. 2. The specific electrode geometry is designed
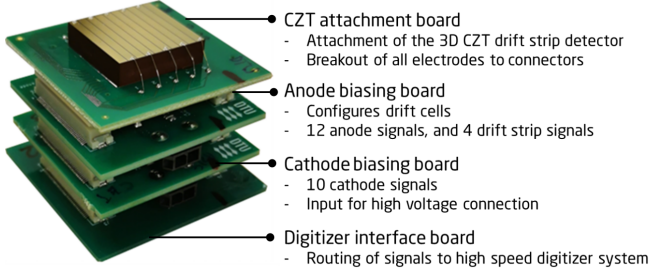
Fig. 1: The 3D MBI test module PCB stack.

TABLE I: The 3D MBI test module bonding options.

Bonding	Module ID
High temperature	B1D1, B1D2.
Room temperature	B1D3, B1D4, B2D1, B2D2, B2D3, B2D4, B2D5, B2D6.

Fig. 2: 3D CZT drift strip detector electrode design: left - the anode side; right - the cathode side of the detector.

Fig. 3: Electrical diagram of a single drift cell. Drift cell boundaries are marked by two vertical dashed lines. D indicates drift signal readout, and A indicates anode signal readout.

to make the detector anodes less sensitive to the movement of the holes in the CZT material thus providing the single polarity sensing and allowing use of advanced positioning algorithms. On one side of the detector crystal, 49 thin electrode strips of width 0.2 mm are deposited using an ohmic contact process. The strips are divided into 12 anodes separated by groups of 3 drift strips. The anodes are virtually grounded as they are connected to the pre-amplifier input, and the drift strips are negatively biased to direct the electrical field lines towards the anodes. On the opposite side of the detector, 10 strip electrodes with a width of 1.8 mm are deposited using the same ohmic contact process. These 10 electrodes are cathodes biased at -450 V. Fig. 3 illustrates the electrical diagram of a single drift cell in the 3D MBI detector. The drift cell constitutes a part of the detector volume, where electrons generated from a photon interaction drift towards the collecting anode in the centre of that drift cell. On the left and right of each collecting anode, there is a drift strip section consisting of three drift strips. A voltage divider distributes the high voltage to the groups of three drift strips. The central drift strip receives 2/3 of the input voltage and each of the two outer strips receive 1/3 of the input voltage. In the current system setup, -450 V is applied to the cathodes, 0 V to the anodes, and -150 V to the drift strip voltage divider. Therefore, the central drift strips are biased at -100 V and the outer drift strips at -50 V.

It is important to stress that the current 3D MBI test modules were designed with the purpose of characterisation of single detector crystals and their performance for the use in MBI. Therefore, the dead space of each module, namely the area with no CZT, has not yet been optimised for the MBI camera performance. Future work on the 3D CZT drift strip detectors will focus on the optimisation of crystal attachment, packaging, electrode arrangement, and readout electronics for use in MBI including the requirements for the emerging low-dose technique.
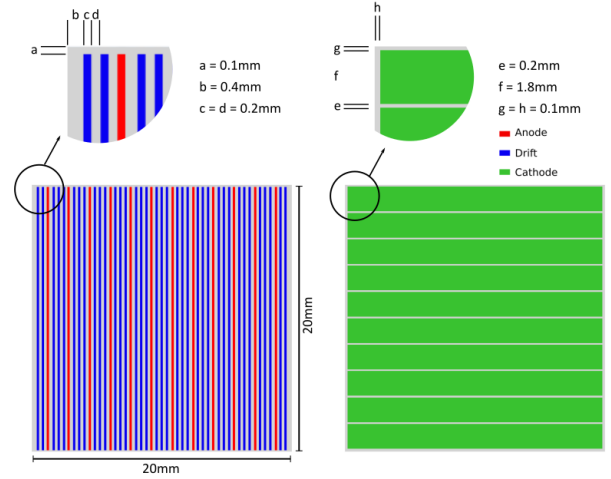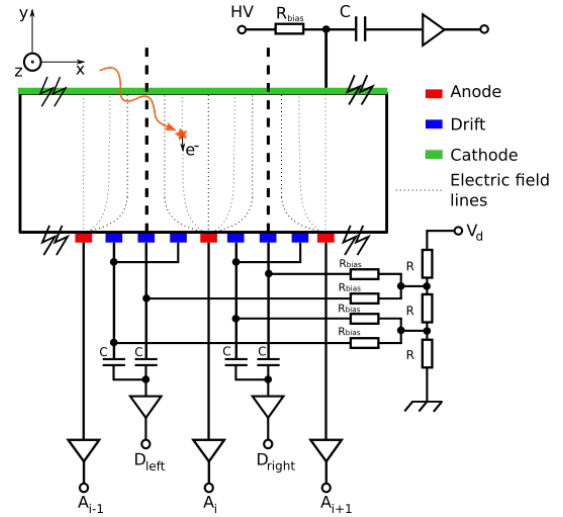
II. MATERIALS AND METHOD

The 3D MBI test modules are evaluated through a full characterisation of electronic noise measurements, I-V curve measurements, slit collimated beam measurements, and flood illumination measurements. In the following sections the experimental setup will be specified.

A. Electronic noise

The electronic noise measurements were conducted by applying a test pulse with no radioactive source illuminating the detector. The measured pulse heights were sampled into a spectrum, one per channel. The FWHM of each spectrum provides the measure of the contribution from the electronic noise for each given electrode. The measurements were taken with and without the high voltage bias, to investigate the

difference between the idle and operating detector electronic noise.

B. I-V curve

The I-V curve setup is mounted in a light-tight box, where the detector modules could be swapped easily. A Keysight B2985A electrometer is used for both voltage and current measurement. For the bulk leakage current measurement, all anodes and drift strips were grounded and a varying high voltage was applied to the cathodes, as shown in Fig. 4(left). The current flowing through the bulk was measured at a number of voltage steps. The surface leakage current was measured by grounding all electrodes except a single anode, where the bias is applied, as shown in Fig. 4(right). The current flowing from the anode to the nearest drift strips was measured. An array of mechanical relays were used to configure the electrodes for both measurements. In between each voltage step, a waiting period of 3 minutes was applied to allow the system to settle before the measurement.
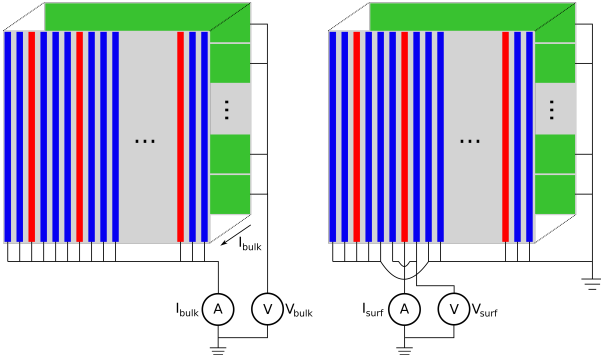

Fig. 4: Schematic of the I-V curve measurement setup for (left) bulk and (right) surface leakage current measurements.

C. Slit beam measurements

The slit beam setup is used to evaluate the position resolution of the detector modules. The detector together with its electronics is mounted on a stepper motor system able to move the detector along three axes with a high precision. The radioactive source is collimated through a slit beam collimator system (tungsten), as shown in Fig. 5. The detector is enclosed in a shielding, which is positioned close to the slit beam opening. In between each measurement, the detector is moved 0.5 mm, to avoid the overlap of the collimated beam projections from the neighbouring positions. The current setup does not allow scanning the depth of the detector, thus only the x- and z-direction have been measured. Fig. 6 illustrates the illumination direction of the collimated beam, together with the step movement direction. The detector coordinate system is specified in Fig. 3: x-direction is perpendicular to the anodes and drift strips, y-direction is along the detector depth, and z-direction is perpendicular to the cathodes.
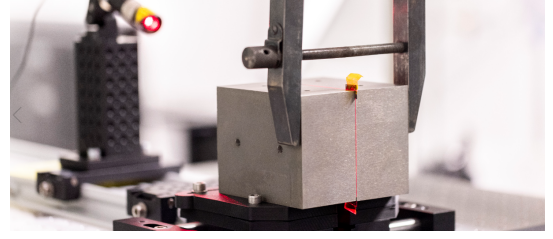

Fig. 5: Tungsten slit beam collimator, with an opening of 0.2 mm × 80 mm.
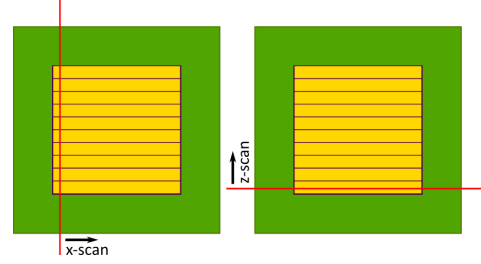

Fig. 6: Illustration of the slit beam illumination geometry for the x- and z-scan measurements of the modules. In the illustration the detector is shown from the cathode side.

D. Flood illumination

Flood illumination measurements of the detector modules are used for energy calibration, evaluation of energy resolution, identification of grain boundaries and trapping centres, and electrode performance evaluation. The measurement setup is simply a radioactive source illuminating the detector surface, without any collimation.

Energy calibration of the detector includes measurements with three sources: ^{241}Am, ^{57}Co, and ^{137}Cs. A Gaussian fit was applied to the photopeaks in the energy spectra to derive the relation between the source energy in keV and resulting pulse height in ADC. This was done for each anode, cathode, and drift strip. The energy resolution of the detectors was determined with two sources: ^{57}Co (122 keV), and ^{137}Cs (661.6 keV).

Illuminating the detector module with a high-energy source such as ^{137}Cs will result in interactions in the entire detector volume. By calculating the 3D position of each interaction, 2D histograms of the spatial distribution of interactions can be extracted. This allows to infer whether the material suffers from severe trapping centres or grain boundaries. Furthermore, the energy spectra of each electrode in the detector allow revealing electrodes suffering from loose connections, as it could result in attenuated or missing signal in the specific electrodes.

III. ANALYSIS PROCEDURE

The 3D CZT drift strip detector analysis procedure consists of a specific set of algorithms returning event type, position of interaction in 3D, electron drift time, and deposited energy as well as a correction thereof.

Each interaction in the detector is sampled with a high speed digitizer system, at a 4 ns sample rate, with a total of 1000 samples. Thus, the system samples the signal of each electrode output: 12 anodes, 10 cathodes, and 4 drift strip signals. Thereby, a total of 26 signals are sampled for any triggered event. The system is triggered by an anode signal exceeding the energy of the upper limit of the Compton continuum (in the area of the Compton edge) for a given source being used in the measurement [17]. This reduces the data size, since mainly the photo-peak data is included in the forthcoming analysis. For a triggered event, 500 samples before and after the trigger are included in the recorded signal. In Fig. 7, an example of the generated signals for a photoelectric absorption event is shown. The 26 distinct signals of any event is a unique fingerprint of the physics interactions in the detector. Analysis of these signals can return information on the event type, 3D position of the interaction, electron drift time, and deposited energy. The left plot in Fig. 7 shows 12 anode signals where the collecting anode signal displays a steep rise. Non-collecting anodes have little to no transient signal, due to compact weighting potentials of the anodes as a result of their small size. The 10 cathode strip signals in Fig. 7(middle) are shown as inverted as a matter of convenience. They display a linear increase as the electron charge cloud moves away from the cathode side towards its collection at the anode. The drift electrodes are read out in four sections, therefore every fourth drift strip signal is convoluted.

In the following sections, the data analysis procedure will be briefly described before presenting the performance of the 10 3D MBI modules. Each data set is initially sorted, so that only single interaction events are included. After that, the 3D interaction positions of each event is determined together with the energy in keV. In Fig. 8 the data analysis procedure is summarised.
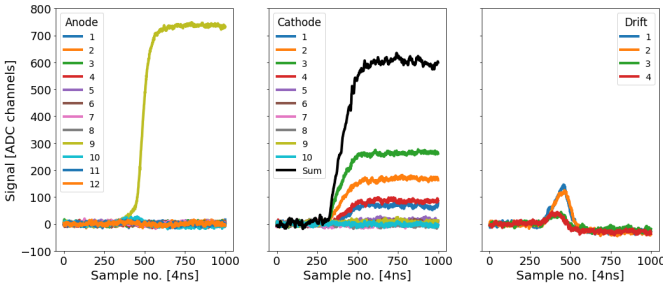

Fig. 7: An example of the spectral shapes of a 661.6 keV photoelectric absorption event.

A. Event characterisation

Initially the data is sorted in terms of the interaction type: single event (photoelectric absorption or Compton scattering followed by an escape of the scattered photon), multiple event (Compton scattering followed by a photoelectric absorption event or by Compton scattering), pair production (if the source energy is larger than 1.02 MeV), and cosmic ray events. The
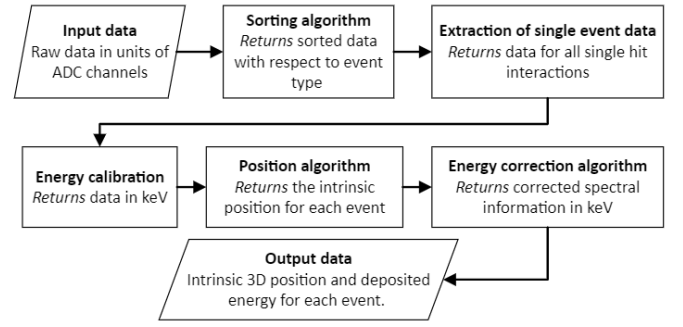

Fig. 8: Overview of the 3D CZT drift strip detector data analysis procedure.

sorting algorithm is interpreting the anode pulse shapes and defining the event type therefrom. The photoelectric absorption event will be similar to the one shown in Fig. 7, displaying a single steep rise in the anode signal. If a Compton scatter interaction occurred, two possible pulse shapes exist. First, two or more anodes display a rise in the pulse shape due to two or more interactions occurring in different drift cells. Second, a single pulse shape will display a staircase like signal due to collection of several electron charge clouds from several interactions within the same drift cell. A combination of the two is also possible. In the case of a cosmic ray event, a large amount of energy is deposited in the detector and all electrodes are displaying a signal. Further information on interaction types can be found in [16].

B. Intrinsic position determination

The intrinsic 3D position of each interaction is determined by signal analysis of the anodes, cathodes, and drift strip signals. The methods will be briefly described in this section, and a more complete description of the algorithms can be found in [15] and [16].

The x-position of an interaction is extracted using the anode and drift strip signals, more specifically the anode signal of the collecting anode together with the signal of the neighbouring drift strip sections. The equation for the x-position calculation is a combination of the raw geometrical position of the collecting anode strip, and the weighting of this position using the drift strips within the drift cell. The triggered anode gives the anode position, and the left and right drift strip signals provides the weighting information. The equation for calculating the x-position of a single interaction event in the detector is given by

$$x = 0.4 + \left[x_{\text{trig}} + F \cdot \frac{A_{\text{DR}} - A_{\text{DL}}}{A_{\text{DR}} + A_{\text{DL}}} \right] \cdot P_{\text{an}} - \frac{P_{\text{an}}}{2} \quad (1)$$

where the constant 0.4 is the offset in millimetre between the detector edge and the first electrode (see Fig. 2), x_{trig} is the number of the triggered anode ($x_{\text{trig}} = 1...12$), and A_{DL} and A_{DR} are the inverted peak values of the left and right drift strip current signals, respectively. Lastly, P_{an} is the

anode pitch equal to 1.6 mm, and F is an adjustable factor for calibrating the x-scale, which for the 3D MBI test modules is equal to 1.

The y-position is calculated using the relation between the anode and cathode pulse heights in the detector, applying the depth of interaction technique

$$y = \frac{\sum_{n=1}^{10} C_n}{A_m} \cdot d_{CZT} \qquad (2)$$

where A_m ($m = 1...12$) is the pulse height of the collecting anode, C_n ($c = 1...10$) is the sum of all cathode pulse heights, and d_{CZT} is the thickness of the detector.

The z-position of interactions in the detector is calculated using the cathode signals through a centre of gravity method

$$z = \frac{\sum_{n=1}^{10} n \cdot C_n}{\sum_{n=1}^{10} C_n} \cdot P_{\text{ca}} - \frac{P_{\text{ca}}}{2} \qquad (3)$$

where P_{ca} is the cathode pitch of 2 mm. For most of the detector volume, applying (3) provides a high resolution z-position. However, the algorithm falls short when the absorption takes place just below a cathode strip [15] and close to the edges. In the case of absorption close to a cathode strip, the electron charge cloud movement results in inducing a full signal in the cathode directly above the interaction, and vanishing signals in the neighbouring cathodes. However, the timing signals of the 3D CZT drift strip detector allow circumventing this issue and utilising negative transient signals in the neighbouring cathodes together with the drift time information in the detector. This is described in more details in [15]. For the edge events, the signal could not be weighted on both sides of the main cathode, resulting in the resolution getting a limited accuracy of $\pm P_{\text{ca}}/2$.

C. Spectral information

The energy deposited by an interaction in the detector is reflected by the pulse height of the collecting anode since the detector is single polarity sensing of negative charges, i.e. electrons. Determining the pulse heights of the signals is a simple procedure, achieved by subtracting the mean value of the first 250 samples from the mean value of the 300 last samples of the signal. The signals are converted from ADC to keV through the energy calibration procedure based on data measured with three sources: Am^{241}, Co^{57}, and Cs^{137}.

The anode reflects the deposited energy, however the electron trapping in the detector and the weighting potential distribution can affect the energy resolution. Therefore, the measured energy is corrected with a 3D look-up table utilising the 3D position capability of the detector. The correction table is built from the measurements of source of a known energy, where the photopeak is fitted along slices in the y-direction and pixels in the x/z-direction, and a correction factor calculated knowing the source energy. The low-energy tail on the left of the photopeak is a result of the charge trapping during the drift of the electron cloud. It is corrected using the 3D position of interaction information in the detector. Events occurring close to the anode contribute to the low-energy tail of the

photopeak as they will not drift thought the full range of the weighting potential. Further explanation on the energy correction technique can be found in [15].

IV. RESULTS

In this section, the overall performance of the 10 3D MBI test modules will be presented. The performance will be compared between the current 10 detectors and the previous 3D CZT drift strip detector prototypes, followed by the overall module performance with a discussion thereof. Next, we will present the electronic noise contribution together with I-V curve measurements. Lastly, we will present both spectral and spatial resolution, and compare this to the necessary performance in an MBI system.

It was decided to characterise the 10 modules using two sources; 122 keV (^{57}Co) and 661.6 keV (^{137}Cs). 122 keV is the gamma-ray energy closest to that of MBI (140keV (^{99m}Tc)) available in the current laboratory setup. Characterisation at 661.6 keV was included, since no characterisation at lower energies such as 122 keV exist for the previous prototypes. The new 3D MBI prototypes were developed applying a simpler electrode deposition technique, excluding the oxide layer. To ensure comparability between the new 3D MBI test modules and previous prototypes, characterisation at 661.6 keV is relevant for the study.

A. Overall module performance

The overall module performance is evaluated in terms of having grain boundaries in the bulk, attenuated signals in the electrodes, or completely missing signal. In Table, II the overall performance is summarised for each module. In the following sections, each module will be introduced and all existing issues will be discussed.

TABLE II: Summary of the overall module performance.

Module no.	Description
B1D1	Grain boundary along the extend of anode 9.
B1D2	Missing signal from drift strip 1 between anode 8 and 9. Noisy signal on anode 11.
B1D3	No detected issues.
B1D4	No detected issues.
B2D1	Signal attenuation on cathodes 1 and 6.
B2D2	No detected issues.
B2D3	Anode 3 and 7 - a combination of attenuated and missing signal.
B2D4	No detected issues.
B2D5	No detected issues.
B2D6	Signal attenuation on cathodes 3, 5, and 6. Missing signal on anode 9.

1) Module B1D1: Inspection of pulse height spectra for each electrode reveal expected performance and full signal in all electrodes. However, the pulse height spectra for the anodes indicate the presence of charge trapping in the detector volume due to a attenuated photopeak in anode number 9. Comparing this to the 2D histogram of interaction positions in the detector, revealed a clear grain boundary along the extend of drift cell number 9. This could be seen in Fig. 9, where the pulse height spectra for anodes 8, 9, and 10, together with a 2D position

histogram of a section of the XZ-plane of the detector are shown. We can see that the photopeak of anode number 9 is attenuated, comparing to the neighbouring anodes, which display clear photopeaks around 122 keV. Thus, the extreme charge trapping occurs in this area, resulting in the attenuated photopeak and a clear boundary in the 2D histogram. This feature is not associated with the electrode deposition or signal in the detector, but the CZT material itself.
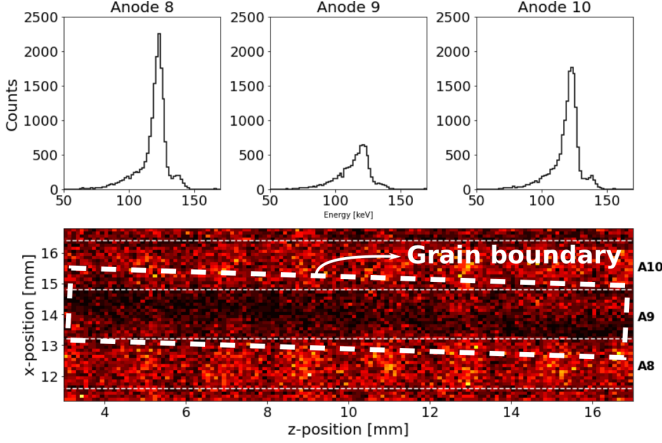

Fig. 9: Pulse height histograms of anode 8, 9, and 10 together with a 2D position histogram of the XZ-plane of the B1D1 detector module of a 122 keV flood-illumination measurement. The white dashed lines in the 2D histogram show drift cell boundaries between anode sections 8, 9, and 10. A clear grain boundary is seen in anode section 9.

2) Module B1D2: Inspection of the pulse height spectra of the electrodes for module B1D2 revealed an expected performance in all cathodes, but a number of issues in some anodes and drift strips. Anode number 11 displayed an excessive broadening of the spectrum, indicating considerable electronic noise in the signal. The remaining anodes displayed expected performance. The drift strip issue was recognised while inspecting the 2D histogram of interaction positions in the detector, where a peculiar feature was observed, as one can see in Fig. 10. In the area between the anodes 8 and 9, or z-positions between 0 mm and 16 mm, all events are collected in the neighbouring drift cell of the collecting anode. Thus, the events collected by anode 9 were assigned to drift cell 10 where anode 10 is collecting, and events collected by anode 8 were assigned to drift cell 7 where anode 7 is collecting. This feature was closely investigated to determine the root cause of the problem. What is common for anode 8 and 9 is that they share drift strip section 1, which separates the two. Drift strip 1 is to the left of anode 9 and to the right of anode 8. Investigating the signals in this area for z-positions below 16 mm, we can see that there is little to no signal in drift strip 1. The x-position algorithm will therefore not have the weighting term contribution between the left and right drift strip around the anode in this area, resulting in the events being assigned only to the left in the case of anode 8, and only to the right in

the case of anode 9. This indicates a connection issue of drift strip 1 in this area of the detector. The issue is more evident in the 661.6 keV data compared to 122 keV, since the electronic noise contribution is less dominant.
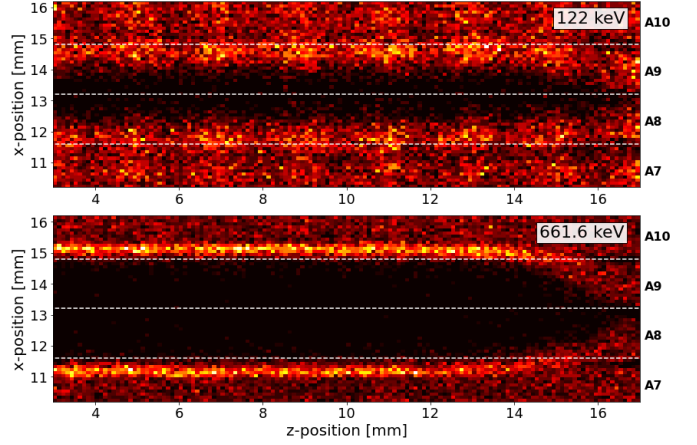

Fig. 10: 2D position histogram (122 keV (top) and 661.6 keV (bottom) flood-illumination measurement) of the XZ-plane for module B1D2 around anode number 7-10 .

3) Modules B2D1, B2D3, and B2D6: Modules B2D1, B2D3, and B2D6 displayed common issues with attenuated or missing signals in either cathodes or anodes.

Module B2D1 has an overall expected performance, however, it does display attenuated signals for cathodes number 1 and 6. This affects the z-positioning ability of the detector, especially in the areas around these cathodes, together with the y-position in the area below the same cathodes.

Module B2D3 has an overall expected performance as well, and has no issues with the cathode signals. However, the detector has attenuated or missing signal in anodes number 3 and 7. For high energy (661.6 keV) and thus high trigger data, no events are registered in the two anodes, resulting in two dead zones. At lower energies (122 keV), and thus low trigger data, signal occurs in anode number 3, indicating a strong attenuation in the signals of these anodes, thus offsetting data to lower energies due to connection issues. Signal for anode 7 is missing entirely.

Module B2D6 has issues with both anode and cathode signals. First of all, anode number 9 experiences a strongly attenuated signal. Furthermore, signal attenuation exist on several cathodes; 3, 5, and 6.

4) Modules B1D3, B1D4, B2D2, B2D4, and B2D5: The remaining test modules; B1D3, B1D4, B2D2, B2D4, and B2D5, performed as expected. The modules showed full signal on all electrodes, with no exaggerated noise, together with even distribution of interactions in the 2D histograms of interaction positions.

B. Electronic noise

Each detector module has 26 readout channels comprising 12 anodes, 10 cathodes, and 4 drift strip sections. The electronic noise was investigated for each channel using a test

pulse, with and without high voltage applied. The pulse height spectra for each test pulse measurement were fitted with a Gaussian, and the FWHM was extracted. Fig. 11 summarises the measured electronic noise, with one plot for each detector module. The grey solid lines indicates the fitted FWHM for the electronic noise without the high voltage applied, and the black solid line indicates the fitted FWHM with high voltage applied. Dotted lines indicate the boundaries between the anode channels (channels 1-12), cathode channels (channels 13-22), and drift strip channels (channels 23-26), which is also indicated through the background colours red (anodes), green (cathodes), and blue (drift strips).

Inspecting the electronic noise measurements for all modules, show the general tendency of a higher electronic noise for drift strips, comparing to the anodes and cathodes. This is due to the fact that the drift strips are read out in groups of 3-4 per one channel, resulting in an increased electronic noise. Inspecting the electronic noise measurements, some parallels can be drawn to the issues detected in the previous section. First of all, modules B1D3, B1D4, B2D2, B2D4, and B2D5 performed as expected if inspecting electrode pulse height spectra. The electronic noise measurements showed consistent electronic noise performance among all electrodes. We do see that the modules from batch 1: B1D3, and B1D4 have a larger electronic noise in the drift strip signal once the high voltage is applied.

Module B1D1 is also displaying a consistency in the electronic noise measurements, which is to be expected since the module did not indicate any electrode issues but suffered from a grain boundary in the CZT material.

Module B2D1 shows a general consistency in the electronic noise signal, however anode 1 has an increase in electronic noise as the high voltage is turned on, but nothing that could be connected to an issue in the electrode signal. And even though this module showed attenuated signals in the cathodes number 1 and 6, this is not connected to the electronic noise in the detector.

Module B2D3 shows overall consistent electronic noise performance, and there is no relation between the electronic noise and the attenuated or missing anode signals.

Module B1D2 has a high electronic noise in anode number 11 and high electronic noise in drift strips number 1 and 4. As previously mentioned, anode number 11 for B1D2 displayed huge noise when inspecting its pulse height spectrum, which is explained by this outlier in electronic noise compared to neighbouring channels.

Module B2D6 suffers from the high electronic noise for anodes 3, 5, and 6, and cathodes 3, 4, and 5. The electronic noise is not directly related to the attenuated signals for the cathodes, since attenuated signals were seen for cathodes 3, 5, and 6.

C. Bulk and surface leakage current

The bulk and surface leakage currents of the detector modules were characterised through the common I-V curve measurements. In the following sections, we will present the
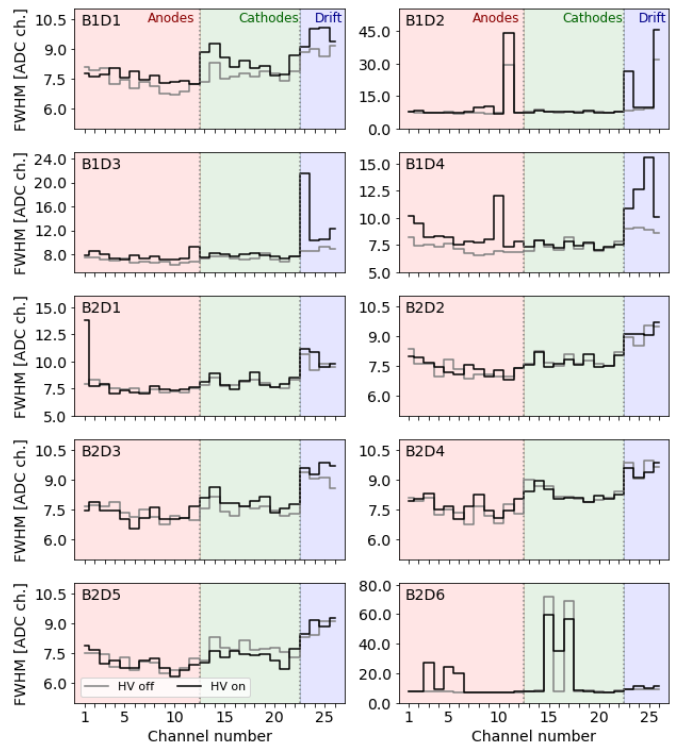

Fig. 11: Electronic noise for the 26 readout channels in all 10 detector modules, with applied high voltage bias (black solid lines), and without applied high voltage bias (grey solid lines). Coloured sections indicate channels comprising anodes (red), cathodes (green), and drift strips (blue).

resulting characteristics of the bulk and surface leakage current measurements.

1) Bulk leakage current: The bulk leakage current was measured for each of the 10 detector modules in the range from -450 V to 50 V. In Fig. 12, the 10 IV-curves are displayed with a zoom-in around the origin. For the positive voltage values, a big difference between batch 1 and batch 2 is observed. Batch 1 experiences an increase in the current comparing to the batch 2 where modules are very stable and streamlined. For the negative voltages, modules B1D1 and B1D2 are streamlined with the five first modules of batch 2, excluding B2D6. Modules B1D3, B1D4, and B2D6 experience a larger bulk leakage current. The observed differences can first of all be explained by crystal orientation when the detector dicing cannot be controlled. Secondly, it is conspicuous that B2D6 experiences a high leakage current, as the module has several electrodes with bad connection and large electronic noise.

2) Surface leakage current: The surface leakage between the anodes and the neighboring drift strip was measured for each detector module. The measurements was taken at -50 V, since this represents the operational voltage difference between the anode and first neighboring drift strip. The results are summarized for each module and for each anode in Fig. 13.
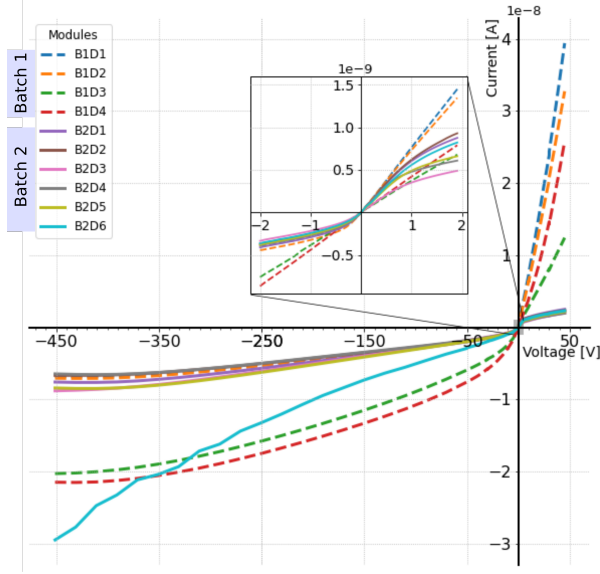
Fig. 12: IV-curve bulk leakage current measurements for the 10 3D MBI test modules.

Fig. 13: Surface leakage current measurements at -50V.

Overall, we see that the modules from batch 1 have a general tendency of larger leakage current than those of batch 2. B1D1 has an increase in surface leakage current for anode 11 comparing to the other anodes, but we do not see this reflected in any other results in the module. Module B1D2 shows a substantial increase in the surface leakage current for anode 11, which might explain the increase in the electronic noise for that electrode. The remaining modules have no significant fluctuations comparing to the neighbouring anodes.

Common for batch 2 is that all anodes show surface leakage current of the order of a few nA, indicating that the more simple electrode deposition method is acceptable comparing to the previous more complicated method with a specific oxide layer below drift strips [14].

D. Spectral performance

The energy resolution was determined for all detector modules at 122 keV (^{57}Co) and 661.6 keV (^{137}Cs). Fig. 14 summarises the spectral performances at 122 keV at 661.6 keV. We see similar energy resolution FWHM at both energies, indicating the major contributor to the energy resolution is the electronic noise. At 661.6 keV the energy resolution FWHM is lower than 1.6% ($\sim$10 keV), where at 122 keV it is in lower than 9% ($\sim$10 keV). For both energies we see that module B2D6 has the worst energy resolution, due to the high electronic noise of 3 out of 12 anodes. We also see that poor energy resolution is especially contributed by anodes 3, 5, and 6, which also was indicated in the electronic noise measurements (Fig. 11). For module B1D1, the worst energy resolution among the anodes is in anode 9 due to the grain boundary trapping centre. For module B1D2, the main contribution comes from anode 11, which was the anode with high electronic noise and surface leakage current. The electronic
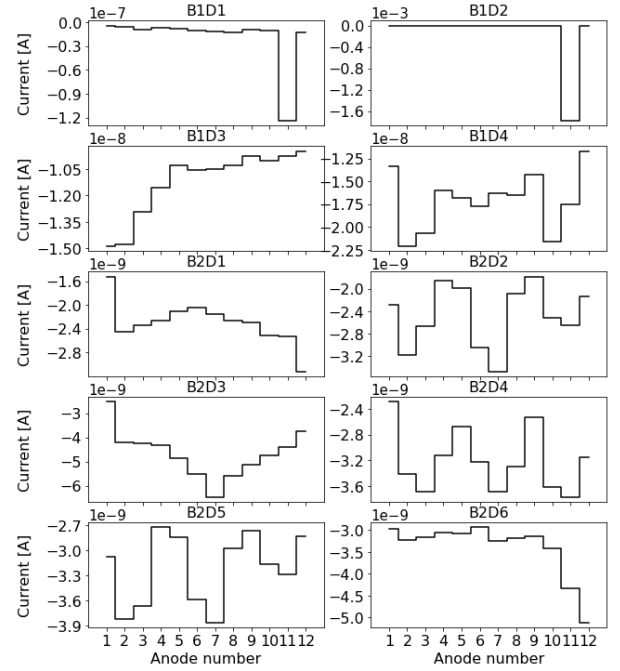
noise measurements together with the energy resolution determination at 122 keV and 661.6 keV, shows that the electronic noise is the limiting factor in the module energy resolution. The 122 keV measurements are completely dominated by the electronic noise limiting the performance. It is a known fact that the current prototype setup suffers from electronic noise [18], therefore achieving a better energy resolution will require improving the future experimental setup. Furthermore, some modules (such as B2D6) suffer from extra electronic noise in a number of anodes, which also limits the performance. This underlines the fact that for low energy applications using this detector technology, the limiting factor is the electronic noise. The main impact on energy resolution by improving the experimental setup is a reduction of the electronic noise contribution. Short term plans for the next iteration of the 3D MBI modules are implementing shorter traces (and thus less parasitic capacitance) together with a better shielding of the electronic box. Long term plans include moving the amplifiers into an integrated circuit as close as possible to the crystal.

E. Intrinsic spatial resolution

The intrinsic spatial resolution was determined at the energy of 122 keV (^{57}Co) and 661.6 keV (^{137}Cs). The setup used for positional scans for the two energies is the same, as the detectors were scanned along the x- and z-direction.

The intrinsic spatial resolution was evaluated within the following boundaries; 0mm $< x <$ 20mm, 1mm $< y <$ 5mm, 2mm $< z <$ 18mm. Furthermore, when the detector was scanned directly at a drift cell boundary along the x-direction, this scan was excluded from the analysis. This is due to the fact that the electron charge cloud generated by an interaction
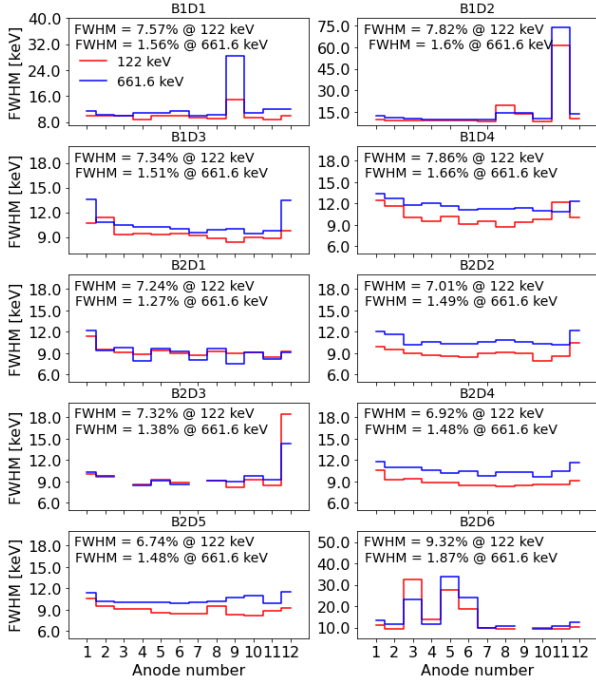
Fig. 14: Energy resolution at 122 keV and 661.6 keV for each anode in the 10 modules. Energy resolution for a combined anode signal is given in percentage.

directly at the drift cell boundary will drift towards and be collected at two neighbouring anodes, and the x-position algorithm in its current state does not treat those events properly resulting in the under-estimation of the resolution.

For each scan measurement, the positions were calculated for each (photoelectric absorption) event. A Gaussian was then fitted to a position histogram of each scan measurement, and the FWHM of the scan represents the position resolution at a given energy and scan direction. Fig. 15 shows the resulting position resolutions for x- and z-scan data at 122 keV and 661.6 keV. We can see that the sub-mm position resolution has been achieved for all modules, except for the z-scan of module B2D6, which suffers from several bad cathodes. The x-position resolution at 661.6 keV is smaller than 0.5 mm, and smaller than 0.7 mm at 122 keV. The z-scan shows sly larger values comparing to the x-scan, but for 661.6 keV around 0.55 mm, and for 122 keV they are centred around 0.65 mm. One would expect that the position resolution for ^{57}Co would be better than that of 661.6 keV, due to the electron charge cloud being smaller. However, as previously mentioned, the current prototype-setup electronics suffer from high electronic noise, which is the limiting factor for these positional resolutions. The signal to noise ratio for the ^{57}Co data is worse than that of the ^{137}Cs data, which therefore contributes to the position resolution determination. However, even though the current setup struggles from a large electronic noise component, it achieves sub-mm position resolution along both x- and z-directions, also at low energies. B2D6 does show that having

several cathodes with attenuated signal strongly affects the spatial performance along the z-direction, however, module B2D1 does not show a big effect from this, since only two well separated cathodes suffered from attenuated signal. In terms of the depth resolution of the detector, a scan has not been carried out due to experimental limitations of the current setup. However, the previous prototypes of the 3D CZT drift strip detector have shown sub-mm position resolution along the depth at 661.6 keV [15], [16]. We do expect the same performance from the current 3D CZT drift strip technology, especially when the electronic noise is limited. Since the new modules show acceptable leakage current performance with the simpler electrode deposition process, we do expect a similar or better performance when compared to the previous prototypes.
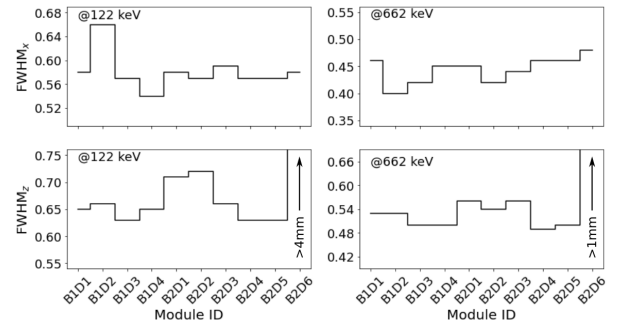

Fig. 15: Spatial resolution of the 10 3D MBI test modules along the x- and z-direction for energies 122 keV and 661.6 keV.

V. CONCLUSIONS

In this work, 10 3D MBI test modules have been developed, based on the 3D CZT drift strip detector. A detector initially intended for observing the high energy universe, was now investigated for the potential use in medical application for breast cancer diagnostics in future MBI systems.

The work resulted in the fabrication of 10 detector modules, each thoroughly characterised using the same procedure. Four modules had minor issues, and only one module (B2D6) suffered from significantly worse than the rest in terms of spectral and z-position resolution. The main limiting factor in both spectral and spatial performance was shown to be the electronic noise. It was carefully evaluated and clearly connected to the current prototype setup, which was not optimised for reducing the electronic noise. This is not expected to be a limiting factor once a dedicated ASIC is developed for the detector in future iterations.

The spectral resolution of the modules was evaluated to be less than 1.6% FWHM at 661.6 keV, and less than 9% FWHM at 122 keV. The spectral resolution was clearly limited by the electronic noise. We do expect the resolution at 661.6 keV to be closer to 1% with a lower electronic noise, thereby also expecting approximately 5% or less for the 122 keV measurements. Especially with the future development of a

dedicated ASIC electronic readout system for the specific 3D CZT drift strip technology, electronic noise can be minimised.

The spatial resolution was evaluated in the lateral direction for all modules at 122 keV and 661.6 keV. The x-position resolution at 661.6 keV was less than 0.5 mm FWHM, and less than 0.7 mm FWHM at 122 keV. The z-position resolution (excluding module B2D6) was evaluated to be less than 0.6 mm FWHM at 661.6 keV, and less than 0.75 mm FWHM at 122 keV. This work allows us to conclude that the 3D MBI test modules perform with a sub-mm intrinsic spatial resolution in the lateral direction of the detector, also at low energies (122 keV) which is sufficient to satisfy the MBI requirements. Improving the spatial resolution in the lateral direction to below 1 mm will affect the spatial resolution of the MBI image, including the minimal detectable tumour size, which indeed will be an improvement of the system. If the depth resolution (as is strongly expected) is sub-mm, this will allow stronger reduction of the patient dose and screening time, as it is vital for the de-multiplexing method [9]. Future 3D MBI modules are being designed to allow performing the scan along the depth of the detector, thus enabling the full 3D spatial resolution.

The 10 3D MBI detector modules were developed with a simpler electrode deposition process, excluding the previous oxide layer between the drift strips and CZT crystal [14]. Even though this oxide layer was excluded from the process, the surface leakage current was within the acceptable order of magnitude, and the detector spectral and spatial performance was as expected. Thus, future iterations of the 3D CZT drift strip detector can be produced with less complexity.

In conclusion, the 3D CZT drift strip technology could be an excellent candidate for the future emerging MBI technologies, assisting in reducing the patient dose, screening time, and detectable tumour size. Furthermore, comparing to the pixellated detectors, the 3D CZT drift strip detector technology performs with a sub-mm position resolution and with vastly fewer readout channels.

ACKNOWLEDGEMENTS

REFERENCES

[1] W. A. Berg and A. Vourtsis, "Breast density implications and supplemental screening," European Radiology, vol. 29, pp. 1762–1777, 2019.

[2] C. L. Vaughan, "Novel imaging approaches to screen for breast cancer: Recent advances and future prospects," Medical Engineering and Physics, vol. 72, pp. 27–37, 2019.

[3] A. J. González, F. Sánchez, and J. M. Benlloch, "Organ-dedicated molecular imaging systems," IEEE Transactions on Radiation and Plasma Medical Sciences, vol. 2, no. 5, pp. 388–403, 2018.

[4] M. K. O'Connor, "Molecular breast imaging: an emerging modality for breast cancer screening," Breast cancer management, vol. 4, no. 1, pp. 33–40, 2015.

[5] D. J. Rhodes, C. B. Hruska, A. L. Conners, C. L. Tortorelli, R. W. Maxwell, K. N. Jones, A. Y. Toledano, and M. K. O'Connor, "Molecular breast imaging at reduced radiation dose for supplemental screening in mammographically dense breasts," AJR. American journal of roentgenology, vol. 204, no. 2, p. 241, 2015.

[6] C. B. Hruska, S. W. Phillips, D. Whaley, D. J. Rhodes, and M. K. O'Connor, "Molecular breast imaging: use of a dual-head dedicated gamma camera to detect small breast tumors," American Journal of Roentgenology, vol. 191, no. 6, pp. 1805–1815, 2008.

[7] C. B. Hruska, A. L. Weinmann, and M. K. O'Connor, "Proof of concept for low-dose molecular breast imaging with a dual-head czt gamma camera. part i. evaluation in phantoms," Medical physics, vol. 39, no. 6, pp. 3466–3475, 2012.

[8] C. B. Hruska and M. K. O'Connor, "Nuclear imaging of the breast: translating achievements in instrumentation into clinical use," Medical physics, vol. 40, no. 5, p. 050901, 2013.

[9] A. Cherlin, A. Wirth, I. Baistow, K. Erlandsson, K. Thielemans, and B. F. Hutton, "A new concept for a low-dose stationary tomographic molecular breast imaging camera using 3d position sensitive czt detectors." IEEE NSS MIC (RTSD), 2021.

[10] K. Erlandsson, A. Wirth, I. Baistow, K. Thielemans, A. Cherlin, and B. F. Hutton, "Novel approaches to reconstruction of highly multiplexed data for use in stationary low-dose molecular breast tomosynthesis." 16th International Meeting on Fully 3D Image Reconstruction in Radiology and Nuclear Medicine., 2021.

[11] B. F. Hutton, K. Erlandsson, A. Wirth, I. Baistow, K. Thielemans, and A. Cherlin, "Design of an ultra-low-dose, stationary, tomographic molecular breast imaging system." IEEE NSS MIC, 2021.

[12] M. Van Pamelen and C. Budtz-Jørgensen, "Novel electrode geometry to improve performance of cdznte detectors," Nuclear Instruments and Methods in Physics Research Section A: Accelerators, Spectrometers, Detectors and Associated Equipment, vol. 403, no. 2-3, pp. 390–398, 1998.

[13] M. Van Pamelen and C. Budtz-Jørgensen, "Cdznte drift detector with correction for hole trapping," Nuclear Instruments and Methods in Physics Research Section A: Accelerators, Spectrometers, Detectors and Associated Equipment, vol. 411, no. 1, pp. 197–200, 1998.

[14] I. Kuvvetli, C. Budtz-Jørgensen, A. Zappettini, N. Zambelli, G. Benassi, E. Kalemci, E. Caroli, J. B. Stephen, and N. Auricchio, "A 3d czt high resolution detector for x-and gamma-ray astronomy," High energy, optical, and infrared detectors for astronomy VI, vol. 9154, p. 91540X, 2014.

[15] C. Budtz-Jørgensen and I. Kuvvetli, "New position algorithms for the 3-d czt drift detector," IEEE Transactions on Nuclear Science, vol. 64, no. 6, pp. 1611–1618, 2017.

[16] S. H. Owe, I. Kuvvetli, C. Budtz-Jørgensen, and A. Zoglauer, "Evaluation of a compton camera concept using the 3d cdznte drift strip detectors," Journal of Instrumentation, vol. 14, no. 01, p. C01020, 2019.

[17] G. F. Knoll, Radiation detection and measurement. John Wiley & Sons, 2010.

[18] S. H. Owe, I. Kuvvetli, and C. Budtz-Jørgensen, "Carrier lifetime and mobility characterization using the dtu 3-d czt drift strip detector," IEEE Transactions on Nuclear Science, vol. 68, no. 9, pp. 2440–2446, 2021.

C   Paper 3

Preprint version submitted for review to The Journal of Instrumentation (JINST) on September 28, 2023.

Feasibility of Using 3D CZT Drift Strip Detectors for Small Compton Camera Space Missions

S. R. H. Owe[a,1] **I. Kuvvetli**[a] **A. Zoglauer**[b] **C. Budtz-Jørgensen**[a]

[a]*DTU Space, Technical University of Denmark*
 Elektrovej building 327, 2800 Kgs. Lyngby, Denmark

[b]*University of California, Berkeley,*
 Space Sciences Laboratory, 7 Gauss Way, Berkeley, CA 94720, USA

E-mail: shoowe@space.dtu.dk

ABSTRACT: This feasibility study explores the possibility of using 3D CZT drift strip detectors developed by DTU Space in a small Compton camera payload, with the primary objective of technology demonstration. We have defined a scalable mass model for the payload, comprising eight 3D CZT drift strip detectors surrounded by CsI scintillator detectors for active shielding. The payload's angular resolution, effective area, and efficiency are evaluated through simulations of far-field monochromatic point sources. The instrument's sensitivity is assessed in a low Earth orbit background environment for narrow-line and continuum sources. With a 3σ point source sensitivity on the order of 10^{-4} [ph/cm^2/s], it is evident that such an instrument only allows for limited scientific goals. In-orbit simulations of bright sources are conducted, resulting in reasonable observation times for the Crab Nebula at a 5σ significance level. Furthermore, in-orbit simulations of a selection of bright gamma-ray bursts indicate the potential for observing bright transient events. The study underscores the potential of using 3D CZT drift strip detectors in Compton camera configurations but also highlights the need for a larger effective area to improve sensitivity. However, for a technology demonstration aimed at increasing the Technology Readiness Level of the 3D CZT drift strip detector, a small Compton camera configuration like the one presented in this study could be a viable solution.

KEYWORDS: Gamma detectors, X-ray detectors and telescopes, Instrument optimisation, Space instrumentation.

---

[1]Corresponding author.

Contents

1 Introduction

The low-to-medium-energy gamma-ray range (0.1 to 100 MeV) is one of the least explored in the electromagnetic spectrum. It is inherently difficult to observe due to low flux, low interaction probability, three energy loss processes, and a high background radiation rate. Nevertheless, a wide range of interesting astrophysical processes can be studied in this energy band. Examples include nuclear lines from radioactive nuclei generated by supernova explosions, short gamma-ray bursts from colliding neutron stars, 511 keV gamma-rays from electron-positron annihilation, and gamma-ray emissions from the most energetic environments in our universe, such as those around pulsars or accreting black holes. Only the next generation of space telescopes will be capable of making meaningful advances in this field. To enhance the sensitivity of future observatories, new state-of-the-art sensor technology will be a key contributor. For a detector to be selected to fly on any future large observatory, it must undergo thorough testing and have a high technology readiness level (TRL). This simulation study investigates the feasibility of operating a small spaceborne Compton camera payload utilizing the 3D CdZnTe (CZT) drift strip detector technology.

1.1 The 3D CZT drift strip detector

The detector group at DTU Space initiated a development program aimed at improving the spectral performance of CZT detectors. This effort resulted in the creation of the 3D CZT drift strip detector [1–3]. This detector incorporates a unique electrode geometry and a distinctive spatial position algorithm, as described in previous research [4]. These innovations have led to a significant enhancement in the achievable position and energy resolution for CZT detectors, even those with

crystals of limited quality. In contrast to the common pixelated electrode geometry (where the required number of readout channels increases with cubic power with the sensitive detector volume) the 3D CZT drift strip detector allows for a reduction in the required readout channels. Recent prototypes, measuring 2cm × 2cm × 0.5cm, have achieved sub-millimeter position resolution (<0.5 mm @ 662 keV) in 3D and demonstrated excellent energy resolution (at best <1% @ 662 keV)[4–7]. It was demonstrated that the spatial positioning algorithm could be extended to identify multiple gamma-ray interactions within a single detector, allowing for the identification of Compton interactions within the same detector volume. At its current state, some issues can occur when assigning the photon interaction coordinates, and the algorithms do not currently include interactions collected by the same anode in the detector. However, despite the shortcomings, the single detector crystal can be operated as a Compton camera [5]. This is especially favorable for space applications where low source fluxes require the identification of as many gamma-ray interactions as possible. In recent years, the technology has matured significantly, and state-of-the-art 3D CZT drift strip detector modules can now achieve sizes of 4cm × 4cm × 0.5cm. Characterization results of these modules are ongoing and will be published elsewhere.

The 3D CZT drift strip detector technology is applicable in various fields, such as medical applications [7] and space [5]. The TRL of the 3D CZT drift strip detector technology has increased since its invention, advancing from a TRL of 1 to 4. Proof of concept studies and relevant tests have been conducted in a laboratory environment. To further elevate the TRL, the technology must be assessed in a relevant environment, namely, in space. One viable approach is to deploy the detector technology in a small Compton camera, either on a CubeSat or another small satellite payload. In this study, we investigate the feasibility of conducting astronomical observations in a low Earth orbit (LEO) environment using a CubeSat-sized payload of 3D CZT drift strip detectors operated as a Compton camera.

2 Model setup

To evaluate the detection capabilities of a simple Compton camera concept utilizing 3D CZT drift strip detectors in a space radiation environment such as LEO, we make use of Monte Carlo simulations using the Medium-Energy Gamma-ray Astronomy library (MEGAlib) [8]. In this section we introduce the simulation framework, together with the instrument model, and simulation method for this study.

2.1 Simulation framework

The software package MEGAlib[1], incorporates ROOT and Geant4 and specializes in simulating Compton telescopes. It comprise all necessary steps, including simulation, event reconstruction, image reconstruction, and data analysis. The instrument mass model is defined using the MEGAlib tools, along with explicit detector specifications that allow the application of realistic detector effects such as energy and positions resolution, thresholds, etc. The sources (both astrophysical and background) used for the Monte Carlo simulations are also defined using the framework. In addition, all necessary data analysis tools for the study are provided with MEGAlib.

---

[1]MEGAlib: https://github.com/zoglauer/megalib.

2.2 Instrument model

Compton cameras typically operate in the 0.1-10 MeV range and utilize one or more Compton scatter interactions in the detectors to identify the origin of the photon. By measuring the position and energy deposited by several Compton interactions within the camera, it is possible to reconstruct the source position to a cone in the sky. Several interactions, and overlapping cones can then with image reconstruction reveal the source location [9].

A mass model of a compact Compton camera based on 3D CZT drift strip detectors was developed with MEGAlib. Figure 1 shows a schematic of the payload geometry and detector specifications. Final characterization work of the latest detector module (4cm × 4cm × 0.5cm) is ongoing, therefore specifications of the detector in MEGAlib is based on previous detector version performances. The energy resolution is extracted from [10] and set to twice the FWHM for a conservative value. In reality, with good electronics, these values could improve further. We chose to restrict the number of CZT detectors in the camera to eight. This resulted in four layers with two detectors each, and a distance of 1.1cm between the layers. The eight CZT detectors are surrounded by 1cm-thick CsI scintillators, used as active shielding. Active shielding and background rejection is a crucial element when building a Compton camera for LEO, due to high background in the Compton-regime. The mass model of the instrument is kept as simple as possible for this feasibility study. That excludes photomultipliers connected to the scintillator shields, other passive material in the instrument, and spacecraft specific materials. Thus, we only include the most basic parts of the payload.

Since we wish to measure Compton sequences from astrophysical sources occurring in the CZT detector payload, we define two trigger criteria. The first one states that two (or more hits) in any CZT detector trigger the system and the event is stored. This includes two or more interactions in a single CZT detector or two or more interactions in different detectors. The second trigger criteria states that if an interaction occurs in the scintillator shield at the same time as in the CZT, the event is vetoed. In LEO, these are predominantly upward moving Earth-albedo photons, i.e., background. The shield also vetoes a significant fraction of charged particle events. As consequence, only Compton sequences exclusively occurring in the 3D CZT drift strip detectors are kept.
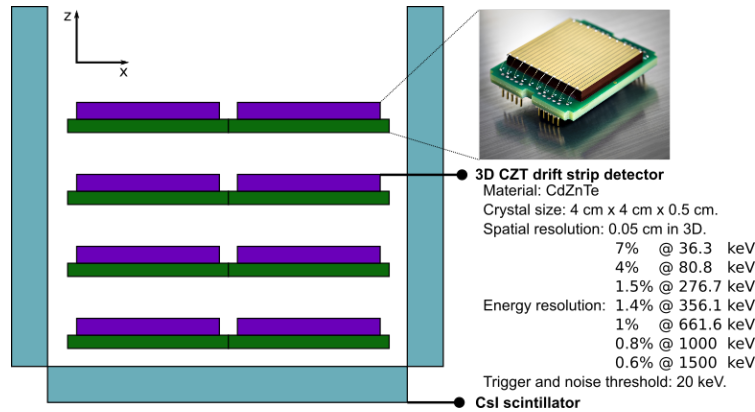

Figure 1. Illustration of the instrument mass model consisting of eight 3D CZT drift strip detectors surrounded by 1cm thick CsI scintillator active shielding. Zenith axis is defined by the z-axis.

2.3 Method

The chronology of the simulation is as follows: First, the geometry and detector characteristics are specified in MEGAlib. This includes the previously defined mass model, along with detector type, material, resolutions, and trigger criteria for the system. Next, simulations are conducted with the instrument payload observing a specific source. Finally, the MEGAlib tools are employed to reconstruct the Compton sequences, generate images, and analyze the simulated data. Since the chronological order of the interactions is unknown, Compton sequence reconstruction is required to determine the path in the detector. We only consider Compton sequences with 2-7 interactions, and with a minimum distance of 1.6mm (in 3D) in between any interaction. The minimum distance of 1.6mm was chosen, since it corresponds to the anode pitch in the 3D CZT drift strip detector.

Four source types are defined for this study: Nuclear lines, continuum emission, transients, as well as the associated background. Sources are specified in MEGAlib with location, flux, energy range, and spectral type. Simulations for a range of monoenergetic far-field point sources (200 keV - 2000 keV) are used to evaluate the overall instrument performance, and to assess basic payload performance parameters such as effective area, Angular Resolution Measure (ARM), and efficiency for a range of monochromatic energies. To evaluate the sensitivity (minimum detectable flux) of the instrument, the background environment is an essential factor. The background in-orbit simulation is based on data retrieved from Spenvis[2], for an orbit like that of the NuSTAR satellite (altitude: 575 km, inclination: 6 degrees). The background source files are generated using MEGAlib and include, photonic, leptonic, and hadronic components. We assume the instrument to be off during South Atlantic Anomaly (SAA) passages, and therefore we do not include the trapped hadronic contribution. The simulation does not yet take into account the activation build-up in the instrument, thus the background simulation reflects the beginning of the observation period.

To assess payload sensitivity, S, for a given significance, z, for a point source, the following expression is used [9]

$$S = \frac{z\sqrt{N_S + N_B}}{A_{eff}T_{eff}}, \tag{2.1}$$

where N_S is the measured source counts in the source extraction region (3σ ARM), N_B is the measured background counts in the source extraction region, A_{eff} is the effective area of the instrument, and T_{eff} is the effective observation time. The minimum detectable flux can be expressed (given the number of source photons at the sensitivity limit $N_S = ST_{eff}A_{eff}$, and solving Eq. (2.1) for S) by

$$S = \frac{z^2 + z\sqrt{z^2 + 4N_B}}{2T_{eff}A_{eff}}. \tag{2.2}$$

This equation can be used to evaluate the payload sensitivity (narrow-line and continuum) in a given background environment.

To finally evaluate the feasibility of operating the 3D CZT drift strip detectors in a payload in space, we conclude the study with simulations of known astronomical sources. We investigate a continuum source (the Crab), and transient sources, with a selection of bright Gamma Ray Bursts (GRBs).

---

[2]Spenvis: www.spenvis.oma.be/

– 4 –

3 Payload performance

In the following sections, we present the simulation results of this study. First, we present the basic payload performance parameters. Next, through a long background environment simulation, we extract the background components to assess payload sensitivity. Finally, we assess the instrument's performance when observing known astronomical sources (both continuum and transient) in a LEO space radiation environment.

3.1 Basic performance

Simulations of far-field point sources with monoenergetic beams are used to evaluate the ARM, effective area, and efficiency of the instrument. An energy window of $\Delta E = \pm 2\sigma$ is used, and a 3σ ARM window is additionally employed to evaluate effective area and efficiency. Thus, we exclusively consider data within the photopeak domain of the source resolution element.

In Figure 2(left) the simulated effective area as a function of energy is shown. The effective area was evaluated at a selection of energies at different polar angles (θ, ϕ), varying θ from 0° to 80°, with $\phi = 0$. Zenith is defined along the z-axis in Figure 1, where θ starts from the positive z-axis (zenith), and ϕ from the positive x-axis. The effective area peaks at 300 keV and experiences a steady drop hereafter. This is expected due to the small number of detectors. Including more detector material will increase the stopping power, and by that increase effective area at higher energies. We see the effective area, especially for the lower energies, being strongly affected by the zenith angle of the source, and it peaks around $\theta = 10°$. As the zenith angle increases, the exposed geometrical surface initially increases, resulting in a increase in effective area. Later on, the effective area will decrease once again as the angle further increases, due to increased probability of absorption in the CsI shields. The effects are not as visible at higher energies, where the stopping power limits the effective area.

Figure 2(middle) shows the ARM as a function of energy at zenith incidence angle. The instrument consist of CZT detectors, and Doppler broadening therefore imposes a limiting factor on the ARM [12]. In addition, the lower the energy, the closer the interactions are, and therefore, the relative position uncertainty between detector position resolution of 0.5mm and a minimum distance of 1.6mm between interactions also limits the ARM.
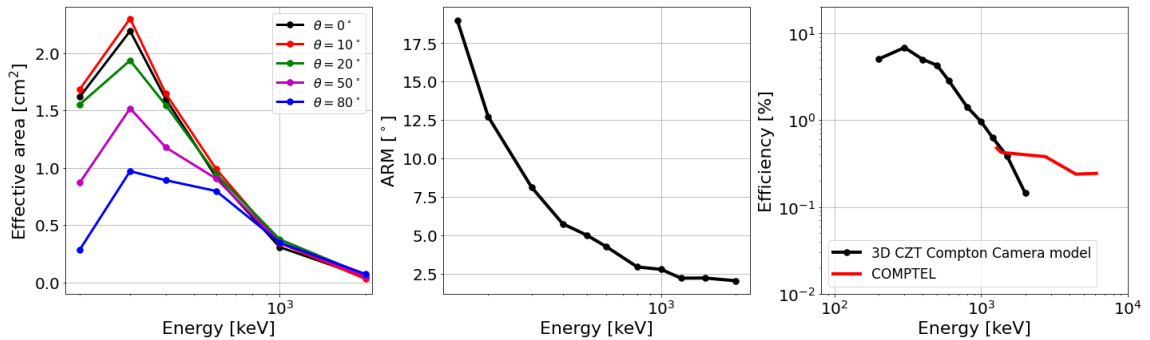

Figure 2. Basic performance parameters of the 3D CZT drift strip detector Compton camera. (Left) Effective area as a function of source energy. (Middle) ARM as a function of energy. (Right) Efficiency at zenith as a function of energy. COMPTEL efficiency is taken from [11] .

Figure 2(right) shows the efficiency of the instrument at zenith and compared to that of COMPTEL [11]. The efficiency was was calculated as the ratio between effective area and geometrical area. The efficiency of the instrument is comparable to that of COMPTEL around 1200 keV, but is less than that of COMPTEL at higher energies. Adjusting number of layers, event selection, and layer distance indicates the instrument could achieve larger efficiency.

3.2 Sensitivity

The calculated narrow-line and continuum sensitivity of the instrument is given in Table 1. Both are evaluated for 3σ significance, with an effective observation time of 10^6 s, using Eq. (2.2).

For the narrow-line sensitivity of the payload model, we applied the effective area presented in Figure 2 (left) at zenith. An energy window of $\Delta E = \pm 2\sigma$ was used. The continuum sensitivity of the payload model was evaluated with a power-law spectrum (E^{-2}), and the energy window for continuum sensitivity calculations was set to $\Delta E = E$. In both cases, we utilized simulations of the background environment to extract the background radiation rate measured by the payload for the specified energy and source extraction region. The calculated sensitivities are in the order of 10^{-4} ph/cm^2/s. This is not a good sensitivity, and in reality, we expect the numbers to be at least a factor of 2-3 worse when passive material and activations are included in the analysis. However, some limited science goals could be possible, especially just for the case of technology demonstration in space. The sensitivity is especially limited by the small effective area. Increasing the effective area of the payload, together with better background suppression, can result in an improvement of sensitivity.

Table 1. The instrument model sensitivity (3σ) is calculated for an effective observation time of 10^6 s. The source extraction region is a 3σ ARM window. The narrow-line sensitivity energy window is $\Delta E = \pm 2\sigma$, and the continuum sensitivity energy window: $\Delta E = E$

	Energy [keV]	3σ point source sensitivity [10^{-4}ph/cm^2/s]
Narrow-line	200	2.4
	400	1.3
	600	1.0
	1000	1.6
	2000	4.7
Continuum	150-450	9.1
	300-900	6.6
	450-1350	7.0
	750-2250	9.2
	1500-4500	20.0

3.3 Continuum source: The Crab

The sensitivity analysis of the instrument suggests that limited scientific objectives should be attainable. Therefore, it is valuable to investigate the payload's performance in an astronomical context, particularly when considering bright sources.

To assess the instrument's performance in observing a known continuum source, we chose the Crab Nebula. It is a bright source and serves as a standard candle within the gamma-ray community.

The Crab is modeled using a power-law and was defined in MEGAlib in the energy range of 50-10000 keV, with spectral definition and flux as documented in [13]. With a simulation only including the Crab source, the ARM and effective area was determined in energy windows of $E = \Delta E$, and the source extraction region defined as 3σ ARM. Next, the required effective observation time for a 5σ observation was calculated using Eq. (2.2). The background rate was extracted from a background-only simulation for the given energy and source extraction window. The resulting ARM, effective area, and effective observation time are summarized in Table 2. We observe the shortest required observation time at 300 keV, where the Crab flux is higher, and the payload has a larger effective area. The observation times, ranging from approximately 1 to 8 hours, are reasonable for a small satellite mission like a technology demonstration. A simulation combining the Crab and in-orbit background sources ran for an observation time of 12 ks. The reconstructed images are displayed in Figure 3. The background at 300 keV is notably more suppressed compared to 600 keV, thanks to the shorter observation times required at 300 keV to achieve a significant Crab signal.

Table 2. Payload ARM, effective area, and effective observation time of the Crab in-orbit with the energy window $E = \Delta E$.

Energy [keV]	ARM [°]	A_{eff} [cm^2]	T_{eff} [s] (5σ)
300	10.3	1.9	4103.8
600	5.7	1.6	10556.4
900	3.7	0.8	30285.3
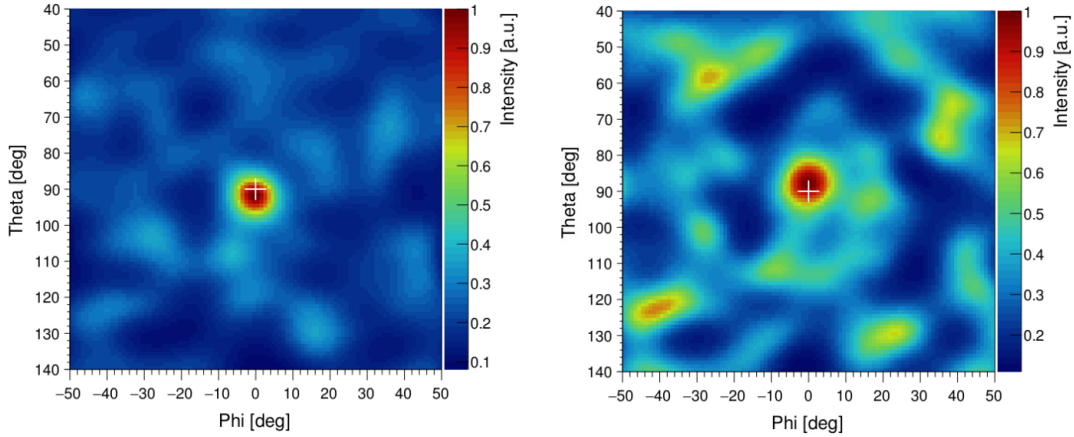
Figure 3. Simulation of an in-orbit observation of the Crab (12 ks at zenith) was conducted at 300 keV (left) and 600 keV (right). Both images display data in energy windows $\Delta E = E$. White crosses indicate the true source position.

3.4 Transient source: Gamma-ray burst

GRBs are transient events in the sky. Short GRBs (< 2 s) are associated with compact binary system mergers, while long GRBs (> 2 s) are associated with core-collapse supernovae. These events can occur anywhere in the sky; therefore, instruments with large fields of view are preferred for detecting GRBs. Observing GRBs in coincidence with a gravitational wave signal is a key factor in multi-messenger astronomy. Several groups are exploring the development of CubeSats for GRB

detection and localization to improve the chances of observation. Examples of current and future missions include Glowbug [16], BurstCube [17], and MoonBEAM [18].

The spectral and fluence characteristics of GRBs vary greatly. GRBs with a small fluence will be impossible to detect given our low effective area. Therefore, we have selected a sample of six bright GRBs that are present in both the 'CGRO/BATSE Complete Spectral Catalog of Bright GRBs' [14] and the 'CGRO/BATSE 5B Gamma-Ray Burst Spectral Catalog' [15]. All GRBs were simulated in the previously mentioned background environment, with the GRB at zenith. In Figure 4 the reconstructed images of the six simulated GRBs are shown. The spectral characteristics of the GRBs are summarized in Table 3. Four out of the six GRBs are visible in the image, with three distinctly visible above the background: GRB 990411, GRB 980923, and GRB 991127. GRB 980208 is also visible, albeit slightly off-axis from the true source position. The remaining two GRBs, 4B 940902 and 4B 930425, were not visible, primarily due to their lower fluence. This indicates that the instrument, designed for space qualification of the detector technology, could possibly detect bright GRBs if they occur within its field of view during operation.
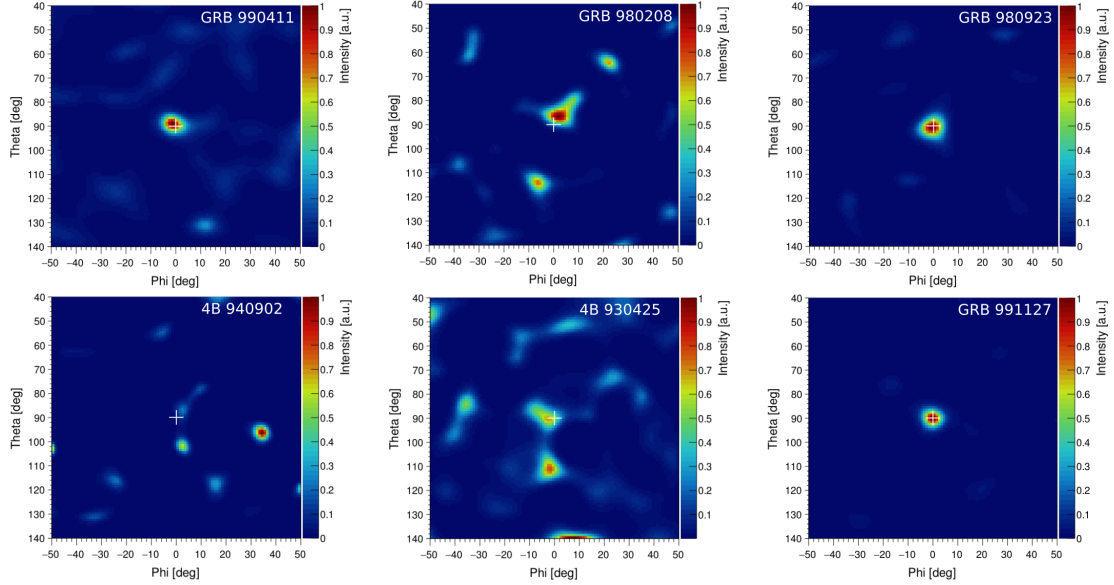
Figure 4. Simulation of six on-axis GRBs. The white cross indicate the true source position, and the GRB name is indicated in the upper right of each image.

Table 3. Selection of GRBs from the CGRO/BATSE Complete Spectral Catalog of Bright GRBs[14, 15].

Name	t_{90} [s]	α	β	E_{peak} [keV]	Flux [ph/cm^2/s]	Fluence [ph/cm^2]	Detected
GRB 990411	328.448	-1.50	-2.27	283	0.82	269.3	Yes
GRB 980208	31.232	-0.96	-2.38	229	3.91	122.1	Yes
GRB 980923	33.024	-0.76	-2.52	388	7.25	239.4	Yes
4B 940902	32.032	-2.10	-2.68	529	0.62	19.9	No
4B 930425	29.184	-1.60	-2.31	163	2.60	75.9	No*
GRB 991127	52.672	-1.15	-2.25	393	1.93	101.7	Yes

* Only vaguely visible slightly off axis of the true source position.

4 Conclusion

One key advantage of the 3D CZT drift strip detector in a Compton camera is its ability to distinguish multiple Compton interactions within the same detector [5]. However, to use the detector on future Space missions, its TRL must be elevated. In this study, we investigate the in-orbit performance of a small Compton camera payload based on the 3D CZT drift strip detector, aiming to assess its feasibility for operation in a small Compton camera configuration as a technology demonstration in space.

The chosen payload consisted of eight 3D CZT drift strip detectors surrounded by a 1cm CsI scintillator detector for active shielding. Simulations were conducted to assess the instrument's performance in terms of effective area, ARM, efficiency, and sensitivity. The small geometrical area and high background rate resulted in limited sensitivities, constraining the scientific goals possible for such an instrument. Nevertheless, observing bright sources should be feasible. The instrument's performance was evaluated using bright astronomical sources such as the Crab Nebula and bright GRBs. Relatively short observation times were required for detecting sources like the Crab Nebula, and it was also possible to observe bright GRBs. This study has established a baseline for the potential achievements of an instrument utilizing eight 3D CZT drift strip detectors and an active shielding system. The scalability of the geometry allows for optimization tailored to specific scenarios and the goals of a technology demonstration instrument. However, it's important to note that these simulations represent a best-case scenario. The inclusion of passive materials and activation is expected to lead to a decrease in sensitivity. These constraints will inevitably impact the range of achievable scientific goals. However, optimizing the position algorithm for Compton events in the 3D CZT drift strip detector could lead to shorter event distances than 1.6 mm, negatively impacting ARM but improving the effective area.

In conclusion, this study demonstrates that a small technology demonstration mission, operating 3D CZT drift strip detectors as a simple Compton camera, could achieve some limited science goals.

References

[1] M. Van Pamelen and C. Budtz-Jørgensen, *Novel electrode geometry to improve performance of cdznte detectors*, *Nuclear Instruments and Methods in Physics Research Section A: Accelerators, Spectrometers, Detectors and Associated Equipment* **403** (1998) 390.

[2] M. Van Pamelen and C. Budtz-Jørgensen, *Cdznte drift detector with correction for hole trapping*, *Nuclear Instruments and Methods in Physics Research Section A: Accelerators, Spectrometers, Detectors and Associated Equipment* **411** (1998) 197.

[3] İ. Kuvvetli, C. Budtz-Jørgensen, A. Zappettini, N. Zambelli, G. Benassi, E. Kalemci et al., *A 3d czt high resolution detector for x-and gamma-ray astronomy*, in *High energy, optical, and infrared detectors for astronomy VI*, vol. 9154, pp. 272–281, SPIE, 2014.

[4] C. Budtz-Jørgensen and I. Kuvvetli, *New position algorithms for the 3-d czt drift detector*, *IEEE Transactions on Nuclear Science* **64** (2017) 1611.

[5] S. Owe, I. Kuvvetli, C. Budtz-Jørgensen and A. Zoglauer, *Evaluation of a compton camera concept using the 3d cdznte drift strip detectors*, vol. 14, IOP Publishing, 2019, DOI.

[6] S. Owe, I. Kuvvetli and C. Budtz-Jorgensen, *Carrier lifetime and mobility characterization using the dtu 3d czt drift strip detector*, *IEEE Transactions on Nuclear Science* **68** (2021) 2440.

[7] S. Owe, I. Kuvvetli, A. Cherlin, B. Harris, H. Tomita, I. Baistow et al., *Evaluation of czt drift strip detectors for use in 3d molecular breast imaging*, *IEEE Transactions on Radiation and Plasma Medical Sciences* **7** (2023) 113 .

[8] A. Zoglauer, R. Andritschke and F. Schopper, *Megalib–the medium energy gamma-ray astronomy library*, *New Astronomy Reviews* **50** (2006) 629.

[9] A.C. Zoglauer, *First Light for the next Generation of Compton and Pair telescopes*, Ph.D. thesis, Technische Universität München, 2005.

[10] I. Kuvvetli and C. Budtz-Jørgensen, *Pixelated cdznte drift detectors*, *IEEE Nuclear Science Symposium Conference Record* **7** (2004) 4360.

[11] V. Schonfelder, H. Aarts, K. Bennett, H. Deboer, J. Clear, W. Collmar et al., *Instrument description and performance of the imaging gamma-ray telescope comptel aboard the compton gamma-ray observatory*, *Astrophysical Journal Supplement Series* (1993) .

[12] A. Zoglauer and G. Kanbach, *Doppler broadening as a lower limit to the angular resolution of next-generation compton telescopes*, in *X-Ray and Gamma-Ray Telescopes and Instruments for Astronomy*, vol. 4851, pp. 1302–1309, SPIE, 2003.

[13] P. Sizun, C. Shrader, D. Attié, P. Dubath, S. Schanne, B. Cordier et al., *The integral/spi response and the crab observations*, *arXiv preprint astro-ph/0406058* (2004) .

[14] Y. Kaneko, R.D. Preece, M.S. Briggs, W.S. Paciesas, C.A. Meegan and D.L. Band, *The complete spectral catalog of bright batse gamma-ray bursts*, *The Astrophysical Journal Supplement Series* **166** (2006) 298.

[15] A. Goldstein, R.D. Preece, R.S. Mallozzi, M.S. Briggs, G.J. Fishman, C. Kouveliotou et al., *The batse 5b gamma-ray burst spectral catalog*, *The Astrophysical Journal Supplement Series* **208** (2013) 21.

[16] J.E. Grove, C.C. Cheung, M. Kerr, L.J. Mitchell, B.F. Phlips, R.S. Woolf et al., *Glowbug, a gamma-ray telescope for bursts and other transients*, in *Proc. Yamada Conf. LXXI*, pp. 1–11, 2019.

[17] J. Racusin, J.S. Perkins, M.S. Briggs, G. de Nolfo, J. Krizmanic, R. Caputo et al., *Burstcube: a cubesat for gravitational wave counterparts*, *arXiv preprint arXiv:1708.09292* (2017) .

[18] M.S. Briggs, *The moon burst energetics all-sky monitor (moonbeam) cubesat, a gamma-ray burst detector for cislunar orbit*, in *AGU Fall Meeting Abstracts*, vol. 2020, pp. SH040–06, 2020.

Bibliography

[1] B. P. Abbott et al. "GW170817: Observation of Gravitational Waves from a Binary Neutron Star Inspiral". In: *Phys. Rev. Lett.* 119 (16 Oct. 2017), p. 161101. DOI: 10.1103/PhysRevLett.119.161101.

[2] P. Mészáros et al. "Multi-messenger astrophysics". In: *Nature Reviews Physics* 1.10 (2019), pp. 585–599. DOI: 10.1117/12.2562352.

[3] C. Kierans, T. Takahashi, and G. Kanbach. "Compton Telescopes for Gamma-Ray Astrophysics". In: *Handbook of X-ray and Gamma-ray Astrophysics*. Ed. by C. Bambi and A. Santangelo. Springer Nature Singapore, 2022, pp. 1–72. DOI: 10.1007/978-981-16-4544-0_46-1.

[4] S. H. Owe, I. Kuvvetli, and C. Budtz-Jorgensen. "Carrier Lifetime and Mobility Characterization using the DTU 3D CZT Drift Strip Detector". In: *IEEE Transactions on Nuclear Science* 68.9 (2021), pp. 2440–2446. DOI: 10.1109/TNS.2021.3068001.

[5] S. R. H. Owe et al. "Evaluation of CZT Drift Strip Detectors for use in 3D Molecular Breast Imaging". In: *IEEE Transactions on Radiation and Plasma Medical Sciences* 7.2 (2023), pp. 113–123. DOI: 10.1109/TRPMS.2022.3220807.

[6] *Nuclear Power*. Oct. 2021. URL: https://www.nuclear-power.com/nuclear-power/reactor-physics/interaction-radiation-matter/interaction-gamma-radiation-matter/.

[7] G. F Knoll. *Radiation detection and measurement*. John Wiley & Sons, 2010.

[8] A. H. Compton. "A Quantum Theory of the Scattering of X-rays by Light Elements". In: *Phys. Rev.* 21 (5 May 1923), pp. 483–502. DOI: 10.1103/PhysRev.21.483.

[9] O. Klein and Y. Nishina. "Über die Streuung von Strahlung durch freie Elektronen nach der neuen relativistischen Quantendynamik von Dirac". In: *Zeitschrift für Physik* 52.11-12 (1929), pp. 853–868. DOI: 10.1007/BF01366453.

[10] J. W. M. Du Mond. "Compton Modified Line Structure and its Relation to the Electron Theory of Solid Bodies". In: *Phys. Rev.* 33 (5 May 1929), pp. 643–658. DOI: 10.1103/PhysRev.33.643.

[11] A. Zoglauer and G. Kanbach. "Doppler broadening as a lower limit to the angular resolution of next-generation Compton telescopes". In: *X-Ray and Gamma-Ray Telescopes and Instruments for Astronomy*. Vol. 4851. SPIE. 2003, pp. 1302–1309. DOI: 10.1117/12.461177.

[12] A. C. Zoglauer. "First Light for the next Generation of Compton and Pair telescopes". PhD thesis. Technische Universität München, 2005.

[13] R. Ribberfors. "Relationship of the relativistic Compton cross section to the momentum distribution of bound electron states. II. Effects of anisotropy and polarization". In: *Physical Review B* 12.8 (1975), p. 3136. DOI: 10.1103/PhysRevB.12.3136.

[14] S. H. Owe. "Characterization of New Generation 3D CZT High Resolution X- and Gamma-ray Detector for High Energy Space Mission Concept (MSc thesis)". 2018.

[15] U. Fano. "Ionization Yield of Radiations. II. The Fluctuations of the Number of Ions". In: *Phys. Rev.* 72 (1 July 1947), pp. 26–29. DOI: 10.1103/PhysRev.72.26.

[16] A. Owens. *Compound semiconductor radiation detectors*. Taylor & Francis, 2016.

[17] *NIST - National Institute of Standards and Technology*. Aug. 2023. URL: https://physics.nist.gov/PhysRefData/Xcom/html/xcom1.html.

[18] K. Hecht. "Zum Mechanismus des lichtelektrischen Primärstromes in isolierenden Kristallen". In: *Zeitschrift für Physik* 77.3-4 (1932), pp. 235–245. DOI: 10.1007/BF01338917.

[19] S. R. H. Owe, I. Kuvvetli, and C. Budtz-Jørgensen. "Three-Dimensional Mapping of Carrier Lifetime and Mobility". In: *High-Z Materials for X-ray Detection*. Ed. by L. Abbene and K. Iniewski. Springer, 2023, pp. 87–110. DOI: 10.1007/978-3-031-20955-0_5.

[20] T. E. Schlesinger and R. B. James. "Semiconductors for Room Temperature Nuclear Detector Applications". In: *Semiconductors and Semimetals* 43 (1995).

[21] A. E. Bolotnikov et al. "Use of the drift-time method to measure the electron lifetime in long-drift-length CdZnTe detectors". In: *Journal of Applied Physics* 120.10 (2016). DOI: 10.1063/1.4962540.

[22] Z. He, G. F. Knoll, and D. K. Wehe. "Direct measurement of product of the electron mobility and mean free drift time of CdZnTe semiconductors using position sensitive single polarity charge sensing detectors". In: *Journal of Applied Physics* 84.10 (1998), pp. 5566–5569. DOI: 10.1063/1.368601.

[23] Z. He. "Review of the Shockley–Ramo theorem and its application in semiconductor gamma-ray detectors". In: *Nuclear Instruments and Methods in Physics Research Section A: Accelerators, Spectrometers, Detectors and Associated Equipment* 463.1-2 (2001), pp. 250–267.

[24] W. Shockley. "Currents to conductors induced by a moving point charge". In: *Journal of applied physics* 9.10 (1938), pp. 635–636. DOI: 10.1063/1.1710367.

[25] S. Ramo. "Currents induced by electron motion". In: *Proceedings of the IRE* 27.9 (1939), pp. 584–585. DOI: 10.1109/JRPROC.1939.228757.

[26] A. Goldwurm and A. Gros. "Coded Mask Instruments for Gamma-Ray Astronomy". In: *Handbook of X-ray and Gamma-ray Astrophysics*. Ed. by C. Bambi and A. Santangelo. Singapore: Springer Nature Singapore, 2022, pp. 1–57. DOI: 10.1007/978-981-16-4544-0_44-1. URL: https://doi.org/10.1007/978-981-16-4544-0_44-1.

[27] *ASIM Atmosphere-Space Interactions Monitor*. Sept. 2023. URL: https://www.asim.dk/.

[28] C. Budtz-Jorgensen et al. "Characterization of CZT Detectors for the ASIM Mission". In: *IEEE Transactions on Nuclear Science* 56.4 (2009), pp. 1842–1847. DOI: 10.1109/TNS.2009.2021423.

[29] T. Neubert et al. "A terrestrial gamma-ray flash and ionospheric ultraviolet emissions powered by lightning". In: *Science* 367.6474 (2020), pp. 183–186. DOI: 10.1126/science.aax3872.

[30] T. Neubert et al. "Observation of the onset of a blue jet into the stratosphere". In: *Nature* 589.7842 (2021), pp. 371–375. DOI: 10.1038/s41586-020-03122-6.

[31] A. J. Castro-Tirado et al. "Very-high-frequency oscillations in the main peak of a magnetar giant flare". In: *Nature* 600.7890 (2021), pp. 621–624. DOI: 10.1038/s41586-021-04101-1.

[32] H. W. Schnopper et al. "Joint European x-ray monitor (JEM-X): x-ray monitor for ESA's INTEGRAL mission". In: *Gamma-Ray and Cosmic-Ray Detectors, Techniques, and Missions*. Ed. by Brian D. Ramsey and Thomas A. Parnell. Vol. 2806. International Society for Optics and Photonics. SPIE, 1996, pp. 297–307. DOI: 10.1117/12.253989.

[33] N. Lund et al. "JEM–X: The X-ray monitor aboard INTEGRAL". In: *Astronomy & Astrophysics* 411.1 (2003), pp. L231–L238. DOI: 10.1051/0004-6361:20031358.

[34] V. Savchenko et al. "INTEGRAL detection of the first prompt gamma-ray signal coincident with the gravitational-wave event GW170817". In: *The Astrophysical Journal Letters* 848.2 (2017), p. L15. DOI: 10.3847/2041-8213/aa8f94.

[35] R. A. Krivonos et al. "INTEGRAL/IBIS 17-yr hard X-ray all-sky survey". In: *Monthly Notices of the Royal Astronomical Society* 510.4 (2022), pp. 4796–4807. DOI: 10.1093/mnras/stab3751.

[36] S. D. Barthelmy et al. "The burst alert telescope (BAT) on the SWIFT midex mission". In: *Space Science Reviews* 120 (2005), pp. 143–164. DOI: 10.1007/s11214-005-5096-3.

[37] E. Virgilli, H. Halloin, and G. Skinner. "Laue and Fresnel Lenses". In: *Handbook of X-ray and Gamma-ray Astrophysics*. Ed. by C. Bambi and A. Santangelo. Springer Nature Singapore, 2022, pp. 1–39. DOI: 10.1007/978-981-16-4544-0_45-1.

[38] F. E. Christensen and B. D. Ramsey. "X-Ray Optics for Astrophysics: A Historical Review". In: *Handbook of X-ray and Gamma-ray Astrophysics*. Ed. by C. Bambi and A. Santangelo. Springer Nature Singapore, 2022, pp. 1–42. DOI: 10.1007/978-981-16-4544-0_1-1.

[39] F. A. Harrison et al. "The nuclear spectroscopic telescope array (NuSTAR) high-energy X-ray mission". In: *The Astrophysical Journal* 770.2 (2013), p. 103. DOI: 10.1088/0004-637X/770/2/103.

[40] *HEX-P: High Energy X-ray Probe*. Sept. 2023. URL: https://hexp.org/.

[41] M. C. Weisskopf et al. "Chandra X-ray Observatory (CXO): overview". In: *X-Ray Optics, Instruments, and Missions III* 4012 (2000), pp. 2–16. DOI: 10.1117/12.391545.

[42] F. Jansen et al. "XMM-Newton observatory-I. The spacecraft and operations". In: *Astronomy & Astrophysics* 365.1 (2001), pp. L1–L6. DOI: 10.1051/0004-6361:20000036.

[43] D. N. Burrows et al. "The Swift X-ray telescope". In: *Space science reviews* 120 (2005), pp. 165–195. DOI: 10.1007/s11214-005-5097-2.

[44] V. Schönfelder et al. "Instrument description and performance of the imaging gamma-ray telescope COMPTEL aboard the Compton Gamma-Ray Observatory". In: *Astrophysical Journal Supplement Series* (1993). DOI: 10.1086/191794.

[45] V. Schönfelder. "Lessons learnt from COMPTEL for future telescopes". In: *New Astronomy Reviews* 48.1-4 (2004), pp. 193–198. DOI: 10.1016/j.newar.2003.11.027.

[46] J. A. Tomsick et al. "The Compton spectrometer and imager project for MeV astronomy". In: *arXiv preprint arXiv:2109.10403* (2021). DOI: 10.48550/arXiv.2109.10403.

[47] T. Siegert, D. Horan, and G. Kanbach. "Telescope Concepts in Gamma-Ray Astronomy". In: *Handbook of X-ray and Gamma-ray Astrophysics*. Ed. by C. Bambi and A. Santangelo. Singapore: Springer Nature Singapore, 2022, pp. 1–71. DOI: 10.1007/978-981-16-4544-0_43-1. URL: https://doi.org/10.1007/978-981-16-4544-0_43-1.

[48] G. Kanbach et al. "The project EGRET (energetic gamma-ray experiment telescope) on NASA's Gamma-Ray Observatory GRO". In: *Space Science Reviews* 49 (1989), pp. 69–84. DOI: 10.1007/BF00173744.

[49] W. B. Atwood et al. "The large area telescope on the Fermi gamma-ray space telescope mission". In: *The Astrophysical Journal* 697.2 (2009), p. 1071. DOI: 10.1088/0004-637X/697/2/1071.

[50] J. McEnery (PI). *AMEGO: All-sky Medium Energy Gamma-ray Observatory. A Multi-messenger Mission for the Extreme Universe*. 2020. DOI: 10.48550/arXiv.1907.07558.

[51] C. A. Kierans. "AMEGO: exploring the extreme multi-messenger universe". In: *Space Telescopes and Instrumentation 2020: Ultraviolet to Gamma Ray*. SPIE, Dec. 2020. DOI: 10.1117/12.2562352.

[52] e-ASTROGAM Collaboration. "The e-ASTROGAM mission: Exploring the extreme Universe with gamma rays in the MeV–GeV range". In: *Experimental Astronomy* 44 (2017), pp. 25–82. DOI: 10.1007/s10686-017-9533-6.

[53] J. E. Grove et al. *Glowbug, a Low-Cost, High-Sensitivity Gamma-Ray Burst Telescope*. 2020. DOI: 10.48550/arXiv.2009.11959.

[54] J. Racusin et al. "BurstCube: a CubeSat for gravitational wave counterparts". In: *arXiv* (2017). DOI: 10.48550/arXiv.1708.09292.

[55] M. S. Briggs. "The Moon Burst Energetics All-sky Monitor (MoonBEAM) CubeSat, a Gamma-ray Burst Detector for Cislunar Orbit". In: *AGU Fall Meeting Abstracts*. Vol. 2020. 2020, SH040–06.

[56] X. Barcons et al. "Athena: ESA's X-ray observatory for the late 2020s". In: *Astronomische Nachrichten* 338.2-3 (2017), pp. 153–158. DOI: 10.1002/asna.201713323.

[57] Lead Proposer K. Danzmann. *LISA Laser Interferometer Space Antenna*. 2017.

[58] M. A. J. Van Pamelen and C. Budtz-Jørgensen. "Novel electrode geometry to improve performance of CdZnTe detectors". In: *Nuclear Instruments and Methods in Physics Research Section A: Accelerators, Spectrometers, Detectors and Associated Equipment* 403.2-3 (1998), pp. 390–398. DOI: 10.1016/S0168-9002(97)01120-0.

[59] M. A. J. Van Pamelen and C. Budtz-Jørgensen. "CdZnTe drift detector with correction for hole trapping". In: *Nuclear Instruments and Methods in Physics Research Section A: Accelerators, Spectrometers, Detectors and Associated Equipment* 411.1 (1998), pp. 197–200. DOI: 10.1016/S0168-9002(98)00283-6.

[60] I. Kuvvetli. "Development of CdZnTe detector systems for space applications". PhD thesis. 2005.

[61] I. Kuvvetli et al. "A 3D CZT high resolution detector for x- and gamma-ray astronomy". In: High Energy, Optical, and Infrared Detectors for Astronomy VI ; Conference date: 22-06-2014 Through 25-06-2014. SPIE - International Society for Optical Engineering, 2014. DOI: 10.1117/12.2055119.

[62] I. Kuvvetli and C. Budtz-Jørgensen. *X-Ray and Gamma-Ray Radiation Detector*. Patent. Also registered as: WO2014EP75643, EP20130194445; WO2015078902; G01T1/24. June 2015.

[63] C. Budtz-Jørgensen and I. Kuvvetli. "New position algorithms for the 3-D CZT drift detector". In: *IEEE Transactions on Nuclear Science* 64.6 (2017), pp. 1611–1618. DOI: 10.1109/TNS.2017.2696574.

[64] I. Kuvvetli and C. Budtz-Jørgensen. *Semiconductor detector with segmented cathode*. Patent. WO2018065024; G01T 1/ 24 A I. Apr. 2018.

[65] S. H. Owe et al. "Evaluation of a Compton camera concept using the 3D CdZnTe drift strip detectors". In: vol. 14. 1. 20th International Workshop on Radiation Imaging Detectors ; Conference date: 24-06-2018 Through 28-06-2018. IOP Publishing, 2019. DOI: 10.1088/1748-0221/14/01/C01020.

[66] I. Kuvvetli and C. Budtz-Jørgensen. "Pixelated CdZnTe drift detectors". In: *IEEE Nuclear Science Symposium Conference Record* 7 (2004), pp. 4360–4364. DOI: 10.1109/NSSMIC.2004.1466852.

[67] *Project: CZT Drift Strip Detectors for 3D Molecular Breast Imaging.* 2018. URL: https://orbit.dtu.dk/en/projects/czt-strip-drift-detectors-for-3d-molecular-breast-imaging.

[68] *COMSOL Multiphysics ®, v. 5.5, COMSOL AB, Stockholm, Sweden.* URL: www.comsol.com.

[69] A. Cherlin et al. "A new concept for a low-dose stationary tomographic Molecular Breast Imaging camera using 3D position sensitive CZT detectors". IEEE NSS MIC (RTSD). 2021.

[70] A. Zoglauer, R. Andritschke, and F. Schopper. "MEGAlib–the medium energy gamma-ray astronomy library". In: *New Astronomy Reviews* 50.7-8 (2006), pp. 629–632. DOI: 10.1016/j.newar.2006.06.049.

[71] P. Sizun et al. "The INTEGRAL/SPI response and the Crab observations". In: *arXiv preprint astro-ph/0406058* (2004). DOI: 10.48550/arXiv.astro-ph/0406058.

[72] Y. Kaneko et al. "The Complete Spectral Catalog of Bright BATSE Gamma-Ray Bursts". In: *The Astrophysical Journal Supplement Series* 166.1 (Sept. 2006), p. 298. DOI: 10.1086/505911.

[73] A. Goldstein et al. "THE BATSE 5B GAMMA-RAY BURST SPECTRAL CATALOG". In: *The Astrophysical Journal Supplement Series* 208.2 (Sept. 2013), p. 21. DOI: 10.1088/0067-0049/208/2/21.